

# Intercalation Dynamics in Lithium-Ion Batteries

by

Damian Burch

B.S., California Institute of Technology, 2000

M.A., University of California, Los Angeles, 2002

Submitted to the Department of Mathematics  
in partial fulfillment of the requirements for the degree of

DOCTOR OF PHILOSOPHY

at the

MASSACHUSETTS INSTITUTE OF TECHNOLOGY

September 2009

©Damian Burch, 2009. All rights reserved.

The author hereby grants to MIT permission to reproduce and to distribute  
publicly paper and electronic copies of this thesis document in whole or in  
part in any medium now known or hereafter created.

Author .....  
Department of Mathematics  
August 7, 2009

Certified by .....  
Martin Z. Bazant  
Associate Professor of Chemical Engineering and Mathematics  
Thesis Supervisor

Accepted by .....  
Michel X. Goemans  
Chairman, Applied Mathematics Committee

Accepted by .....  
David Jerison  
Chairman, Department Committee on Graduate Students

<b>Report Documentation Page</b>		<i>Form Approved OMB No. 0704-0188</i>
Public reporting burden for the collection of information is estimated to average 1 hour per response, including the time for reviewing instructions, searching existing data sources, gathering and maintaining the data needed, and completing and reviewing the collection of information. Send comments regarding this burden estimate or any other aspect of this collection of information, including suggestions for reducing this burden, to Washington Headquarters Services, Directorate for Information Operations and Reports, 1215 Jefferson Davis Highway, Suite 1204, Arlington VA 22202-4302. Respondents should be aware that notwithstanding any other provision of law, no person shall be subject to a penalty for failing to comply with a collection of information if it does not display a currently valid OMB control number.		
1. REPORT DATE <b>SEP 2009</b>	2. REPORT TYPE	3. DATES COVERED <b>00-00-2009 to 00-00-2009</b>
4. TITLE AND SUBTITLE <b>Intercalation Dynamics in Lithium-Ion Batteries</b>		5a. CONTRACT NUMBER
		5b. GRANT NUMBER
		5c. PROGRAM ELEMENT NUMBER
6. AUTHOR(S)		5d. PROJECT NUMBER
		5e. TASK NUMBER
		5f. WORK UNIT NUMBER
7. PERFORMING ORGANIZATION NAME(S) AND ADDRESS(ES) <b>Massachusetts Institute of Technology, 77 Massachusetts Avenue, Cambridge, MA, 02139-4307</b>		8. PERFORMING ORGANIZATION REPORT NUMBER
9. SPONSORING/MONITORING AGENCY NAME(S) AND ADDRESS(ES)		10. SPONSOR/MONITOR'S ACRONYM(S)
		11. SPONSOR/MONITOR'S REPORT NUMBER(S)
12. DISTRIBUTION/AVAILABILITY STATEMENT <b>Approved for public release; distribution unlimited</b>		
13. SUPPLEMENTARY NOTES		
14. ABSTRACT <b>A new continuum model has been proposed by Singh, Ceder, and Bazant for the ion intercalation dynamics in a single crystal of rechargeable-battery electrode materials. It is based on the Cahn-Hilliard equation coupled to reaction rate laws as boundary conditions to handle the transfer of ions between the crystal and the electrolyte. In this thesis, I carefully derive a second set of boundary conditions?necessary to close the original PDE system?via a variational analysis of the free energy functional; I include a thermodynamically-consistent treatment of the reaction rates; I develop a semi-discrete finite volume method for numerical simulations; and I include a careful asymptotic treatment of the dynamical regimes found in different limits of the governing equations. Further, I will present several new findings relevant to batteries Defect Interactions: When applied to strongly phase-separating, highly anisotropic materials such as LiFePO<sub>4</sub>, this model predicts phase-transformation waves between the lithiated and unlithiated portions of a crystal. This work extends the analysis of the wave dynamics and describes a new mechanism for current capacity fade through the interactions of these waves with defects in the particle. Size-Dependent Spinodal and Miscibility Gaps: This work demonstrates that the model is powerful enough to predict that the spinodal and miscibility gaps shrink as the particle size decreases. It is also shown that boundary reactions are another general mechanism for the suppression of phase separation. Multi-Particle Interactions: This work presents the results of parallel simulations of several nearby crystals linked together via common parameters in the boundary conditions. The results demonstrate the so-called ?mosaic effect?: the particles tend to fill one at a time, so much so that the particle being filled actually draws lithium out of the other ones. Moreover, it is shown that the smaller particles tend to phase separate first, a phenomenon seen in experiments but difficult to explain with any other theoretical model.</b>		
15. SUBJECT TERMS		

16. SECURITY CLASSIFICATION OF:			17. LIMITATION OF ABSTRACT <b>Same as Report (SAR)</b>	18. NUMBER OF PAGES <b>160</b>	19a. NAME OF RESPONSIBLE PERSON
a. REPORT <b>unclassified</b>	b. ABSTRACT <b>unclassified</b>	c. THIS PAGE <b>unclassified</b>			

Standard Form 298 (Rev. 8-98)  
Prescribed by ANSI Std Z39-18



# Intercalation Dynamics in Lithium-Ion Batteries

by

Damian Burch

Submitted to the Department of Mathematics  
on August 7, 2009, in partial fulfillment of the  
requirements for the degree of  
DOCTOR OF PHILOSOPHY

## Abstract

A new continuum model has been proposed by Singh, Ceder, and Bazant for the ion intercalation dynamics in a single crystal of rechargeable-battery electrode materials. It is based on the Cahn-Hilliard equation coupled to reaction rate laws as boundary conditions to handle the transfer of ions between the crystal and the electrolyte. In this thesis, I carefully derive a second set of boundary conditions—necessary to close the original PDE system—via a variational analysis of the free energy functional; I include a thermodynamically-consistent treatment of the reaction rates; I develop a semi-discrete finite volume method for numerical simulations; and I include a careful asymptotic treatment of the dynamical regimes found in different limits of the governing equations. Further, I will present several new findings relevant to batteries:

*Defect Interactions:* When applied to strongly phase-separating, highly anisotropic materials such as LiFePO<sub>4</sub>, this model predicts phase-transformation waves between the lithiated and unlithiated portions of a crystal. This work extends the analysis of the wave dynamics, and describes a new mechanism for current capacity fade through the interactions of these waves with defects in the particle.

*Size-Dependent Spinodal and Miscibility Gaps:* This work demonstrates that the model is powerful enough to predict that the spinodal and miscibility gaps shrink as the particle size decreases. It is also shown that boundary reactions are another general mechanism for the suppression of phase separation.

*Multi-Particle Interactions:* This work presents the results of parallel simulations of several nearby crystals linked together via common parameters in the boundary conditions. The results demonstrate the so-called “mosaic effect”: the particles tend to fill one at a time, so much so that the particle being filled actually draws lithium out of the other ones. Moreover, it is shown that the smaller particles tend to phase separate first, a phenomenon seen in experiments but difficult to explain with any other theoretical model.

Thesis Supervisor: Martin Z. Bazant

Title: Associate Professor of Chemical Engineering and Mathematics



## Acknowledgments

I wish to thank several groups for their generous financial assistance. The Air Force Office of Scientific Research (AFOSR) and the American Society for Engineering Education (ASEE) fully funded me for three years through a National Defense Science and Engineering Graduate (NDSEG) fellowship. The Martin Family Society of Fellows for Sustainability (MFSFS) and the National Science Foundation (NSF) each provided an additional semester of support. Finally, the Society for Industrial and Applied Mathematics (SIAM), Mr. John Chisholm, and the NSF all provided travel grants which allowed me to attend several conferences.



# Contents

<b>Contents</b>	<b>7</b>
<b>1 Introduction</b>	<b>15</b>
1.1 Motivation . . . . .	15
1.2 Previous Work . . . . .	17
1.3 The Cahn-Hilliard with Reactions (CHR) Model . . . . .	18
1.4 Outline of the Thesis . . . . .	19
<b>I Theory</b>	<b>21</b>
<b>2 Variational Thermodynamics in Bounded, Open Systems</b>	<b>23</b>
2.1 Free Energy Functionals . . . . .	25
2.1.1 Bulk free energy . . . . .	25
2.1.2 Surface free energy . . . . .	27
2.2 Thermodynamic Potentials . . . . .	29
2.3 Steady States . . . . .	32
2.3.1 Energy extremizing states . . . . .	32
2.3.2 Constrained extremizing states . . . . .	33
2.3.3 Energy minimizing states . . . . .	38
2.4 Dynamic Approach to Equilibrium . . . . .	39
2.4.1 Kinetic equations . . . . .	40
2.4.2 Global time derivatives . . . . .	40
2.4.3 Boundary conditions . . . . .	43
2.5 Single-Species Diffusion in a Crystal . . . . .	43
2.5.1 Non-dimensionalized gradient penalty tensor . . . . .	45
2.5.2 Intercalant and substrate chemical potentials . . . . .	45
<b>3 Reaction Rates</b>	<b>47</b>
3.1 Thermodynamics . . . . .	48
3.2 Elementary Reactions . . . . .	49
3.3 Multi-Step Reactions . . . . .	52
3.4 Reverse Reactions . . . . .	54

3.5 Applications to Lithium Iron Phosphate . . . . .	57
<b>4 Finite Volume Methods Applied to the Cahn-Hilliard Equation</b>	<b>61</b>
4.1 The Finite Volume Method . . . . .	61
4.1.1 Accuracy . . . . .	62
4.1.2 Conservation during time-stepping . . . . .	63
4.2 One-Dimensional Geometries . . . . .	63
4.2.1 General formulas . . . . .	64
4.2.2 The Cahn-Hilliard equation . . . . .	65
4.3 Two-Dimensional Geometries . . . . .	68
4.3.1 General formulas . . . . .	70
4.3.2 The Cahn-Hilliard equation . . . . .	71
<b>5 Stochastic Phase-Field Models</b>	<b>73</b>
5.1 Stochastic Variables . . . . .	74
5.1.1 Multivariate Fokker-Planck Equation . . . . .	74
5.1.2 Multivariate Langevin Equation . . . . .	75
5.1.3 Discrete Approximation of the Variational Derivative . . . . .	77
5.2 Stochastic Fields . . . . .	78
5.2.1 Discrete Approximation . . . . .	78
5.2.2 Generalization . . . . .	79
5.2.3 Continuum Equations . . . . .	80
5.2.4 Example . . . . .	81
<b>6 Dynamical Regimes of the CHR System</b>	<b>85</b>
6.1 The One-Dimensional BTL Regime . . . . .	86
6.2 The One-Dimensional SRL Regime . . . . .	87
6.3 “The SRL Equation” . . . . .	89
6.3.1 Evolution equation . . . . .	90
6.3.2 Concentration field uniformity . . . . .	91
6.3.3 Boundary conditions . . . . .	93
6.3.4 Extension to systems with surface energies . . . . .	93
6.3.5 Relevance to LiFePO <sub>4</sub> . . . . .	93
6.3.6 Wave propagation . . . . .	95
<b>II Applications</b>	<b>99</b>
<b>7 Defects in LiFePO<sub>4</sub></b>	<b>101</b>
7.1 Maximum Charge Capacity . . . . .	101
7.1.1 One-sided capacity . . . . .	102
7.1.2 Two-sided capacity . . . . .	103
7.1.3 Defect formation energy . . . . .	105

7.2	Charge Capacity Fade . . . . .	105
7.3	Wave-Defect Interactions . . . . .	107
7.4	Conclusion . . . . .	109
<b>8</b>	<b>Size-Dependent Spinodal and Miscibility Gaps</b>	<b>111</b>
8.1	Model . . . . .	112
8.2	The CH Miscibility Gap . . . . .	114
8.3	The CHR Spinodal Gap . . . . .	115
8.4	Other Effects . . . . .	120
8.5	Conclusion . . . . .	120
<b>9</b>	<b>Inter-Particle Interactions</b>	<b>121</b>
9.1	Model . . . . .	123
9.2	Numerical Results . . . . .	124
9.3	Discussion . . . . .	126
<b>10</b>	<b>Conclusion</b>	<b>129</b>
<b>III</b>	<b>Appendix</b>	<b>131</b>
<b>A</b>	<b>Source Code</b>	<b>133</b>
A.1	<code>chr1d_params_init.m</code> . . . . .	133
A.2	<code>chr1d_solve.m</code> . . . . .	137
	<b>Bibliography</b>	<b>152</b>

THIS PAGE INTENTIONALLY LEFT BLANK

# List of Figures

1-1	Schematic representation of two models for lithium dynamics in phase-separating materials.	18
2-1	Simulation results demonstrating that an equilibrium concentration field can be non-uniform but still have a uniform, non-zero thermodynamic potential.	35
4-1	Schematic of the geometry for a one-dimensional finite volume method.	64
4-2	The $L^1$ -error of our spatial approximation scheme for the one-dimensional Cahn-Hilliard equation.	68
4-3	Schematic of the geometry for a two-dimensional finite volume method.	69
4-4	The stencil for our FVM scheme for the two-dimensional Cahn-Hilliard equation.	72
4-5	The $L^1$ -error of our spatial approximation scheme for the two-dimensional Cahn-Hilliard equation.	72
6-1	Normalized total concentration of an ion channel being filled via BTL dynamics.	87
6-2	Normalized total concentration of an ion channel being filled via SRL dynamics.	88
6-3	Homogeneous chemical potential as a function of concentration.	95
6-4	Wave response of depth-averaged system to small, sudden voltage drop.	97
6-5	Wave response of depth-averaged system to large, sudden voltage drop.	98
7-1	Bending of the phase boundary during defect interaction.	108
7-2	Instantaneous current during phase boundary-defect interaction.	109
8-1	Width of the miscibility gap as a function of crystal size.	116
8-2	Width of the spinodal gap as a function of crystal size and reaction rate.	118
9-1	Generic free energy plot demonstrating the thermodynamics of phase separation.	122
9-2	Schematic of the inter-particle mosaic instability.	123
9-3	Simulation results for the constant-C-rate lithiation of a set of three nearby particles	125

THIS PAGE INTENTIONALLY LEFT BLANK

# List of Tables

4.1	One-dimensional FVM approximations for point values and low-order derivatives at cell midpoints in the bulk. . . . .	64
4.2	One-dimensional FVM approximations for point values and low-order derivatives at cell endpoints in the bulk. . . . .	65
4.3	One-dimensional FVM approximations for point values and low-order derivatives near the left boundary of the system. . . . .	66
4.4	One-dimensional FVM approximations for point values and low-order derivatives near the right boundary of the system. . . . .	67
7.1	Estimated energy barriers for defect formation in LiFePO <sub>4</sub> . . . . .	106

THIS PAGE INTENTIONALLY LEFT BLANK

# Chapter 1

## Introduction

### 1.1 Motivation

An often-overlooked aspect of the energy problem facing modern society is the separation of production from storage and consumption: many production methods (e.g., solar and wind) are intermittent, and many consumption targets (e.g., cars and cell phones) cannot be tethered to the electrical grid. Thus even in an ideal world with renewable-energy power plants and ubiquitous solar cells, we would still need efficient electrical energy storage technologies. Such systems—primarily batteries, but also supercapacitors—already power all of our portable devices and improve the efficiency of hybrid vehicles. However, we eventually need them to do much more, including drastically reducing gasoline usage in large numbers of automobiles and helping with load-leveling of the output from power plants.

Unfortunately, rechargeable battery technology requires vast improvements in order to sustainably meet all of our demands [1]. For instance, they must be more efficient to avoid wasting energy during cycling<sup>1</sup>. They must be capable of surviving many more power cycles without suffering significant performance degradation in order to reduce the number of batteries which are thrown away<sup>2</sup>. They must be made from safer materials to avoid pollution<sup>3</sup>. They must also be made from more plentiful materials<sup>4</sup>. Finally, and most importantly, they must have dramatically improved effective energy densities<sup>5</sup>, power densities, and recharge times in order to make all-electric or even plugin-hybrid vehicles more feasible.

As technology has improved to address these issues, batteries have become much more complex systems. As an illustration, consider the “voltaic pile” invented by Alessandro Volta in 1800. This was simply a stack of alternating copper and zinc plates between which were

---

<sup>1</sup>For example, the nickel-metal hydride batteries currently found in electric and hybrid vehicles are only capable of delivering 66% of the electricity received during charging.

<sup>2</sup>According to the EPA, over 3 billion batteries are discarded in the U.S. each year.

<sup>3</sup>Many current batteries contain lead, mercury, cadmium, nickel, cobalt, and other potential toxins.

<sup>4</sup>For example, we may only have 90 years worth of nickel left on Earth (“Earth’s natural wealth: an audit”, New Scientist 2605: 34–41, 2007).

<sup>5</sup>The nickel-metal hydride cells in the Toyota Prius are only charged to 60% capacity and only discharged to 40% capacity

placed pieces of cloth soaked in brine. Each copper-cloth-zinc triple is a single electrochemical cell (the pile is a battery consisting of many of these cells in series). Zinc dissolves in the brine, losing two electrons in the process. These electrons travel through an external circuit to the copper plate, at which point they combine with hydrogen ions in the brine to generate hydrogen gas. Thus, complete knowledge of the cell’s static and dynamic properties only requires modeling two simple charge transfer reactions and ionic diffusion through the brine; these physical processes are very well understood. Moreover, many modern electrochemical systems (lead-acid and other wet-cell batteries) still employ similar designs [100, 28, 68].

The basic principle of lithium-ion batteries is similar to the above: there is an anode material which tends to give up electrons; a cathode material which tends to attract electrons; and an electrolyte in between which can transport ions between the anode and cathode without also transporting individual electrons, thus forcing the electrons through an external circuit. However, the active materials in the electrodes are not metals (though experimental studies often employ metallic lithium foil as the anode). Instead, they are each “intercalation” compounds with well-defined crystallography capable of accommodating lithium ions without significant changes to the host structure. In other words, no components of the system are damaged or used up by the electrochemical reactions which drive the cell. This allows the insertion/extraction processes to be reversed and the battery to be rechargeable [68].

Though the principle is the same as the voltaic pile, practical lithium-ion batteries are necessarily much more complicated. The electrode materials are present in the form of a fine powder, with individual particles of the active materials typically being smaller than a micron. The electrode then consists of many such individual particles embedded in the electrolyte. To allow for the flow of electrons through an external circuit, a paste of the electrode material must be applied to a metal current collector (say, copper or aluminum foil). Moreover, the cathode material is often electrically insulating, so it must be interspersed with conductive carbon powder capable of transporting the electrons to and from the current collector. A porous separator is positioned between the two electrodes to prevent them from interacting directly. Finally, safety equipment is also frequently required to prevent overheating and overcharging.

The typical voltage and charge capacity of lithium-ion cells can be computed using classical electrochemistry or measured with simple experiments. However, the desired improvements to power density and cycle life can only be made by understanding the dynamical processes of battery charge and discharge. This is complicated by the many different interacting subsystems which are present. During cell discharge, for example, lithium ions must diffuse through the anode material to get to the particle/electrolyte interface; a chemical reaction must occur to move the ion into the electrolyte and free an electron; lithium ions must diffuse through the porous electrolyte, across the separator, and then through the porous electrolyte again in the cathode; a different chemical reaction must occur at an individual cathode particle in which the lithium ion and an electron from the external circuit are inserted into the host crystal; finally, the ion must diffuse into the crystal to make room for further ion insertion reactions. Study of these processes is made more difficult by the large

range of length scales involved: the electrodes may be a millimeter apart, the individual particles of active material are typically less than a micron wide, and the ionic diffusion in the crystals occurs via individual hops between vacancies which are only a few angstroms apart.

Understanding such systems well enough to determine their faults and improve their performance therefore involves more than just a knowledge of the physical properties of the constituent materials. It requires thorough mathematical modeling of the components, their interactions, and the lithium dynamics during operation. Moreover, the resulting combination of highly interconnected, nonlinear, integral and partial differential equations is complex enough to demand study by applied mathematicians.

## 1.2 Previous Work

John Newman and his research group have pioneered the mathematical modeling of rechargeable batteries [76, 33, 77]. Their **porous electrode theory** consists of a very detailed set of equations for an electrochemical cell, including Butler-Volmer charge-transfer kinetics at the electrodes, concentrated-solution diffusion of lithium between the electrodes, and porous diffusion in the composite cathode. Several assumptions are made about the cathode in particular: each individual particle of the active material is spherical and isotropic; the lithium kinetics inside these particles obey linear Fickian diffusion; and all nearby particles have identical lithium concentration fields.

In 1996—by which time porous electrode theory was well-established—John Goodenough’s group patented the use of  $\text{LiFePO}_4$  as a new cathode material for lithium-ion batteries [83]. Their first paper presents an experimental voltage-vs.-lithium-capacity curve for a cell incorporating  $\text{LiFePO}_4$ , and notes that the voltage is constant until the cell is almost completely charged or discharged. Gibbs’ phase rule therefore suggests that there are two thermodynamic phases in the material—one lithium-rich and the other lithium-poor (this can be visualized by comparing a single crystal of  $\text{LiFePO}_4$  to a closed container of water: the  $\text{H}_2\text{O}$ -rich liquid phase remains separated from the  $\text{H}_2\text{O}$ -poor vapor phase even though individual  $\text{H}_2\text{O}$  molecules can move between the two). The ion kinetics therefore cannot be described by Fickian diffusion, but rather must be governed by the motion of the phase boundary between lithiated and unlithiated regions in each particle.

Such kinematics were incorporated into porous electrode theory by Newman and Srinivasan [92]. In this so-called “shrinking core” model, the concentrations of the lithium-rich and lithium-poor phases are fixed constants; lithium transport is still governed by isotropic, Fickian diffusion; and the sharp interface between the phases is solved for by mass conservation. See Fig. 1-1(a) for a schematic.

Several new findings have shown that this is not a very accurate model for the kinetics of  $\text{LiFePO}_4$ . First, this material forms a highly anisotropic crystal, so one should not expect spherically-symmetric diffusion. Indeed, Ceder’s group has used ab initio methods to predict that the diffusivity in one particular direction is at least 11 orders of magnitude faster than the diffusivity in either of the other two directions [74]. Lithium should therefore be

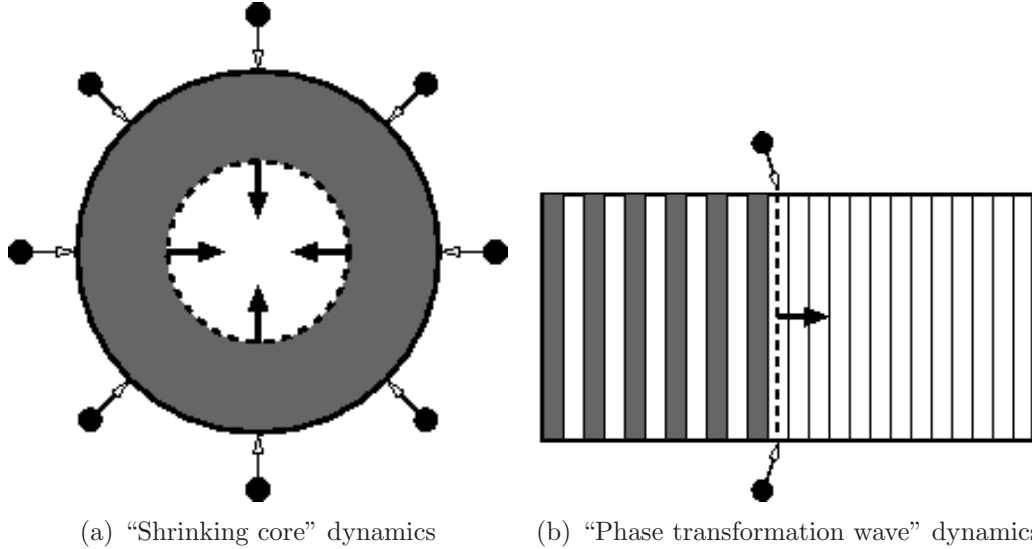


Figure 1-1: Schematic representation of two models for lithium dynamics in phase-separating materials. Dark regions are lithium-rich and light regions are lithium-poor; lithium insertion into the crystal from the surrounding electrolyte is represented by arrows. In the phase transformation wave model, lithium ions can only move up and down, whereas the phase boundary moves to the right during lithiation. Figures reproduced from [90].

essentially confined to one-dimensional channels; this unusual behavior has been verified experimentally [78]. Further, Richardson has published electron microscopy results showing that the phase boundary is planar, extending across the entire crystal, and therefore must move in a direction *perpendicular* to the lithium channels [21]. See Fig. 1-1(b) for a schematic.

It is possible that some modification of the shrinking core model could be devised to surmount these difficulties. However, a major theme of this thesis is that *any* such model will fail to capture important aspects of the charging dynamics in phase-separating materials. The reason is that the shrinking core model accounts for very little of the small-scale physics: the sharp interface is a purely mathematical construct whose energy is not accounted for in the reaction rates, diffusion laws, or cell voltage computation; it provides no physical justification for the phase separation; and it does not model the dynamics of the phase-separation process. As we will see, the simple fact that there is some positive energy associated with the interphase boundary can have important consequences.

### 1.3 The Cahn-Hilliard with Reactions (CHR) Model

In 2008, Singh, Ceder, and Bazant published a paper [90] which, though similar in some ways to an earlier study on graphite [48] and another on LiFePO<sub>4</sub> [47], developed a significantly different model for the intercalation dynamics in phase-separating electrodes. Their motivation was to use physically-motivated models to understand the dynamics rather than just to mimic the kinetics in such materials. Thus, they employed the Cahn-Hilliard equation

to model the diffusion in, and the phase-separation of, the electrode material. More significantly, they used thermodynamically-consistent reaction rate laws for the lithium insertion and extraction process between the electrolyte and the active crystals. This appears to be the first work which has coupled a bulk phase-field model to such boundary reactions, and this has many important consequences for the behavior of the system.

The resulting mathematical model is the first one capable of capturing and explaining the phase-transformation-wave dynamics seen in experiments on LiFePO<sub>4</sub>. At the same time, however, it is sufficiently powerful to describe shrinking-core-like dynamics in different parameter regimes. Further, Singh et al. made connections to standard experiments performed on batteries, and in particular made it clear that the Cottrell equation used to derive diffusivities from Potentiostatic Intermittent Titration Technique (PITT) experiments [104] is probably invalid for materials like LiFePO<sub>4</sub>.

## 1.4 Outline of the Thesis

Implicit in the paper by Singh et al. is that there is an energy cost to maintaining an interphase boundary, and that this cost impacts the bulk diffusion and the boundary reactions. The unifying theme of this thesis is that this energy—effectively a surface tension between the lithium-rich and lithium-poor phases—can have a dramatic impact on the behavior of a real battery. Moreover, the fact that the bulk phase-separating dynamics are coupled to reaction rates at the boundary, and inversely that the reaction rates depend on the interphase energy, makes the CHR equations an essentially new tool in materials science and chemical engineering, respectively.

The first part of this thesis is devoted to a very general, theoretical underpinning of the CHR model and its possible extensions. In Chapter 2, a careful study is made of bulk phase-field models, and great emphasis is placed on proper boundary conditions missing from [90]. In Chapter 3, we discuss simple, classical models for reaction rate laws. Though more sophisticated and realistic models exist, this Chapter will at least provide a derivation of an extension of the Butler-Volmer equation to our setting, and will correct a minor thermodynamic problem with the rate laws employed in [90]. In Chapter 4, we provide a general introduction to the semi-discrete Finite Volume Method employed by the numerical studies in later Chapters. In Chapter 5, we derive a stochastic version of the Cahn-Hilliard equation; though this is unused in later Chapters, such extensions to our theory would be necessary to capture some of the effects of thermal noise (nucleation, for example). In Chapter 6, we discuss various dynamical regimes of the CHR system, and in particular provide a derivation of an important equation from [90].

In the second part of this thesis, we focus on new applications of the CHR model to battery systems. In Chapter 7, we discuss the interaction of phase transformation waves with defects in the crystal, and show in particular that this will cause a power loss in the battery. In Chapter 8, we show that the CHR model predicts that the spinodal and miscibility gaps will shrink as the particle size decreases. We will also demonstrate that boundary reactions are a general mechanism for the suppression of phase separation in the

bulk. In Chapter 9, we discuss certain inter-particle, energetic interactions, and show that the CHR model very simply explains the so-called mosaic effect and its size dependence. Finally, Chapter 10 provides concluding remarks and possibilities for future research.

# Part I

## Theory

THIS PAGE INTENTIONALLY LEFT BLANK

## Chapter 2

# Variational Thermodynamics in Bounded, Open Systems

Most thermodynamics textbooks (e.g., [41, 67, 70]) only discuss systems in which the independent variables are spatially uniform. When multiphase systems are studied, the interphase boundary is assumed to be sharp, and many of the thermodynamic variables experience a discontinuous jump across it. This approach has several disadvantages. First, a theory for the energy and motion of the interphase boundary must be established separately from that of the pure phases. Second, it is computationally difficult to track a moving boundary (this is the so-called “free-boundary problem” in applied mathematics). Third, in real physical systems, such boundaries are usually diffuse: the transition between phases is gradual relative to the molecular length scale.

One method for simultaneously overcoming all of these difficulties is to use a **diffuse-interface** or **phase-field** model. In this approach, the changes in the thermodynamic variables are assumed to be sufficiently smooth to be described using derivatives rather than discontinuous jumps, but sufficiently severe to impact the local free energy densities. The diffuse interphase boundary has an energy which is explicitly modeled together with that of the pure phases. Moreover, a single equation governs the kinetics of the entire system, obviating the need for explicit tracking of the interface (this makes phase-field models similar to level set methods). The resulting equations are not exact (in the sense that Maxwell’s equations are exact for electromagnetic phenomena, for example), but their use has been extensively justified by comparison to experiments [18, 17, 49, 59].

Van der Waals [96] was the first to study thermodynamic systems in which the free energy is not a *function* of the independent variables, but rather is given by a *functional*—an integral whose integrand includes the independent variables and their low-order spatial derivatives. These are now frequently called “Ginzburg-Landau free energy functionals” due to important—but much later—work on superconductivity by Ginzburg and Landau [45]. Cahn and Hilliard [18] also independently proposed such functionals for a liquid-vapor system. This model was extended by Cahn [16] to handle the kinetics of conserved quantities (i.e. those whose total amounts can only change via fluxes at the boundary; for example, the number of molecules of a specific chemical species), and again by Allen and Cahn [3]

to describe the kinetics of non-conserved quantities (which are typically phenomenological variables used to differentiate phases; for example, degrees of crystallinity, superconductivity, or liquidity).

Only recently have these methods been applied to battery materials [47, 90, 94]. They are useful for LiFePO<sub>4</sub> in particular since it is known that this material is phase-separating [83], and that the interface between the lithium-rich and lithium-poor phases is diffuse with a width of around 10 nm [21]. Singh et al., in particular, have developed a phase-field model which compares well with experimentally-observed behavior [90]. Obviously, though, these papers were not meant to introduce the mathematical methods they employed, and future work may require even more sophisticated modeling. It is therefore the goal of this Chapter to derive very general phase-field models, and especially to carefully discuss appropriate boundary conditions.

Whereas traditional thermodynamic systems require only differential and integral calculus, the natural mathematical tool for systems with a free energy functional is the calculus of variations [38, 103, 44]. Unfortunately, there are not many references on general variational approaches to thermodynamics (though see [46]). In particular, most references make assumptions about their system which are violated by ours, including that it is at equilibrium [18], that it is infinite [18], or that it is bounded but is energetically isolated from its surroundings [42]. We will therefore give a careful and general treatment of variational, non-equilibrium thermodynamics applicable to bounded, open systems. For further reviews, see [35] for a general introduction, [17, 49] for the Cahn-Hilliard approach to spinodal decomposition, [59, 23] for phase-field modeling of microstructural evolution, and [12] for phase-ordering kinetics and scaling laws.

The only identities used herein are the multivariate multiplication rule

$$\nabla \cdot (s\mathbf{v}) = (\nabla s) \cdot \mathbf{v} + s\nabla \cdot \mathbf{v} \quad (2.1)$$

and the divergence theorem

$$\int_V \nabla \cdot \mathbf{v} dV = \oint_{\partial V} \hat{\mathbf{n}} \cdot \mathbf{v} dA \quad (2.2)$$

for any scalar field  $s(\mathbf{x})$  and vector field  $\mathbf{v}(\mathbf{x})$ , where  $\hat{\mathbf{n}}$  is an outward unit normal on the boundary of  $V$ ).

We can frequently avoid making any assumptions about the independent thermodynamic fields, and simply label them  $\{\phi_\alpha(\mathbf{x}, t)\}_{\alpha=1}^n$ . When it is necessary to make a notational distinction between conserved and non-conserved fields, we will write  $\{\phi_\alpha\}_{\alpha=1}^n = \{c_\alpha\}_{\alpha=1}^{n_c} \cup \{\eta_\alpha\}_{\alpha=1}^{n_n}$ , where  $n = n_c + n_n$ ; the  $c_\alpha$  are conserved and the  $\eta_\alpha$  are non-conserved.

We will need to deal with functions of the form  $f(\mathbf{x}, \phi, \nabla \phi)$  which themselves depend on a function  $\phi(\mathbf{x}, t)$  and its spatial derivatives. When considering  $f$  as a function from  $\mathbb{R}^d \times \mathbb{R} \times \mathbb{R}^d$  to  $\mathbb{R}$ , we will denote by  $\nabla_{\mathbf{x}}$  the gradient with respect to the first  $d$  arguments,  $\partial f / \partial \phi$  the partial derivative with respect to the  $(d+1)^{\text{st}}$  argument, and  $\nabla_{\mathbf{p}}$  the gradient with respect to the last  $d$  arguments. The notation  $\nabla$  will only be used for the spatial

gradient of  $f(\mathbf{x}, \phi(\mathbf{x}, t), \nabla\phi(\mathbf{x}, t))$ , a compound function from  $\mathbb{R}^d \times \mathbb{R}$  to  $\mathbb{R}$ . Similarly, we use the notation  $\partial/\partial t$  to mean the partial derivative with respect to time of the compound function. On the boundary  $\partial V$  of our volume  $V$ , we will split  $\nabla$  into components  $\nabla_{\parallel}$  and  $\nabla_{\perp} \equiv \partial/\partial n$  which are, respectively, tangent and normal to the boundary. We similarly split  $\nabla_{\mathbf{x}}$  and  $\nabla_{\mathbf{p}}$  into components  $\nabla_{\mathbf{x},\parallel}, \nabla_{\mathbf{x},\perp}$  and  $\nabla_{\mathbf{p},\parallel}, \nabla_{\mathbf{p},\perp}$ . Finally, when considering  $f$  as a function of several variables  $\{\phi_{\alpha}\}_{\alpha=1}^n$ , we will extend this notation in the obvious way, using  $\partial f/\partial\phi_{\beta}$ ,  $\nabla_{\mathbf{p},\beta}$ , etc. to single out derivatives with respect to a specific variable  $\phi_{\beta}$  or its gradients.

Finally, in rigorous treatments of the calculus of variations, it is necessary to be extremely careful about the regularity of putative solutions and the space of functions over which one is optimizing [44]. The purpose of this Chapter is to discuss the practical applications of this theory rather than its mathematical details. Consequently, we will assume all functions are “sufficiently differentiable,” look only for “weak” extrema, etc.

## 2.1 Free Energy Functionals

We first describe how free energy functionals can arise, and derive their most general, low-order form. Since we are dealing with a bounded system, we allow for the possibility that the bulk free energy  $G_{\text{bulk}}$  must be supplemented by a surface free energy  $G_{\text{surface}}$  to account for energetic interactions between the system and its environment. The total free energy is therefore the sum of two different functionals

$$G[\{\phi_{\alpha}\}] = G_{\text{bulk}}[\{\phi_{\alpha}\}] + G_{\text{surface}}[\{\phi_{\alpha}\}] . \quad (2.3)$$

### 2.1.1 Bulk free energy

We begin with the bulk free energy  $G_{\text{bulk}}$ , which is assumed to be the volume integral of a well-defined, local free energy density  $g$ :

$$G_{\text{bulk}}[\{\phi_{\alpha}\}] = \int_V g(\mathbf{x}, \{\phi_{\alpha}\}, \{\nabla\phi_{\alpha}\}, \dots) dV . \quad (2.4)$$

If all of the thermodynamic fields are spatially uniform, then we assume that  $g$  is given by some known homogeneous free energy density  $g_{\text{hom}}(\mathbf{x}, \phi_1, \dots, \phi_n)$ . Following Cahn and Hilliard [18], we then expand  $g$  in a Taylor series about  $g_{\text{hom}}$  in terms of the derivatives of

the  $\phi_\alpha$ , stopping at terms which are second-order:

$$\begin{aligned} g \approx g_{\text{hom}}(\mathbf{x}, \{\phi_\alpha\}) + \sum_{\sigma=1}^n \mathbf{P}^{(\sigma)}(\mathbf{x}, \{\phi_\alpha\}) \cdot \nabla \phi_\sigma \\ + \frac{1}{2} \sum_{\sigma, \tau=1}^n (\nabla \phi_\sigma)^T \cdot \mathbf{K}^{(\sigma\tau)}(\mathbf{x}, \{\phi_\alpha\}) \cdot (\nabla \phi_\tau) \\ + \sum_{\sigma=1}^n \left[ \sum_{i,j=1}^d H_{ij}^{(\sigma)}(\mathbf{x}, \{\phi_\alpha\}) \frac{\partial^2 \phi_\sigma}{\partial x_i \partial x_j} \right] . \end{aligned}$$

The vectors  $\mathbf{P}^{(\sigma)}$  and the second-rank tensors  $\mathbf{K}^{(\sigma\tau)}$  and  $\mathbf{H}^{(\sigma)}$  may depend on the thermodynamic variables, but not their derivatives. Further, to avoid using restricted sums, we take  $\mathbf{K}^{(\sigma\tau)} = (\mathbf{K}^{(\tau\sigma)})^T$  for all pairs of indices  $\sigma \neq \tau$ . This can also be extended to hold when  $\sigma = \tau$ : in this case,  $\mathbf{K}^{(\sigma\sigma)}$  acts as a binary quadratic form, so may be assumed to be symmetric since its antisymmetric part makes no contribution to the sum above.

By the chain rule,

$$\sum_{i,j=1}^d H_{ij}^{(\sigma)} \frac{\partial^2 \phi_\sigma}{\partial x_i \partial x_j} = \nabla \cdot (\mathbf{H}^{(\sigma)} \nabla \phi_\sigma) - (\nabla_{\mathbf{x}} \cdot \mathbf{H}^{(\sigma)}) \cdot \nabla \phi_\sigma - \sum_{\tau=1}^n (\nabla \phi_\tau)^T \cdot \frac{\partial \mathbf{H}^{(\sigma)}}{\partial \phi_\tau} \cdot (\nabla \phi_\sigma) .$$

The two rightmost terms of this equality may be absorbed into  $\mathbf{P}^{(\sigma)}$  and  $\mathbf{K}^{(\sigma\tau)}$ , respectively, leaving

$$\begin{aligned} g = g_{\text{hom}}(\mathbf{x}, \{\phi_\alpha\}) + \sum_{\sigma=1}^n \mathbf{P}^{(\sigma)}(\mathbf{x}, \{\phi_\alpha\}) \cdot \nabla \phi_\sigma \\ + \frac{1}{2} \sum_{\sigma, \tau=1}^n (\nabla \phi_\sigma)^T \cdot \mathbf{K}^{(\sigma\tau)}(\mathbf{x}, \{\phi_\alpha\}) \cdot (\nabla \phi_\tau) \\ + \sum_{\sigma=1}^n \nabla \cdot [\mathbf{H}^{(\sigma)}(\mathbf{x}, \{\phi_\alpha\}) \cdot \nabla \phi_\sigma] . \end{aligned}$$

Since  $G_{\text{bulk}} = \int_V g dV$ , the divergence theorem (2.2) proves that the second-derivative term only contributes to the free energy via the surface integral

$$\oint_{\partial V} \sum_{\sigma=1}^n \hat{\mathbf{n}} \cdot (\mathbf{H}^{(\sigma)} \cdot \nabla \phi_\sigma) dA .$$

We therefore consider this part of the surface contribution to the free energy, and remove it from our expression for  $g$ .

Finally, we make the standard reflection symmetry assumption [18] about the system that the free energy density is invariant under the transformation  $\nabla \phi_\beta \mapsto -\nabla \phi_\beta$  absent any

spatial gradients among the other  $\phi_\alpha$ . This implies that  $\mathbf{P}^{(\beta)} = \mathbf{0}$  for all  $\beta$ , leaving the final form of the bulk free energy density

$$g(\mathbf{x}, \{\phi_\alpha\}, \{\nabla \phi_\alpha\}) = g_{\text{hom}}(\mathbf{x}, \{\phi_\alpha\}) + \frac{1}{2} \sum_{\sigma, \tau=1}^n (\nabla \phi_\sigma)^T \cdot \mathbf{K}^{(\sigma\tau)}(\mathbf{x}, \{\phi_\alpha\}) \cdot (\nabla \phi_\tau) . \quad (2.5)$$

Since this was derived using a Taylor expansion, we are implicitly assuming that all derivatives are small and that higher-order terms are negligible. Of course we do not know a priori how big the higher-order terms are, so the truncated expansion may only be valid for nearly-homogeneous systems or for those near their critical temperature. Despite this problem, we will follow standard practice and assume that the system is always in local quasi-equilibrium, that there is consequently a well-defined free energy density, and that this density is always given exactly by (2.5).

The second-order tensors  $\mathbf{K}^{(\sigma\tau)}$  are usually called **gradient-penalty tensors** as they give the energy contributions of the interphase boundaries. The gradient terms in (2.5) may be written in block-matrix form:

$$\frac{1}{2} \begin{pmatrix} (\nabla \phi_1)^T & (\nabla \phi_2)^T & \cdots & (\nabla \phi_n)^T \end{pmatrix} \cdot \begin{pmatrix} \mathbf{K}^{(11)} & \mathbf{K}^{(12)} & \cdots & \mathbf{K}^{(1n)} \\ \mathbf{K}^{(21)} & \mathbf{K}^{(22)} & \cdots & \mathbf{K}^{(2n)} \\ \vdots & \vdots & \ddots & \vdots \\ \mathbf{K}^{(n1)} & \mathbf{K}^{(n2)} & \cdots & \mathbf{K}^{(nn)} \end{pmatrix} \cdot \begin{pmatrix} \nabla \phi_1 \\ \nabla \phi_2 \\ \vdots \\ \nabla \phi_n \end{pmatrix} .$$

To ensure that this is positive for any non-zero gradients, i.e. to guarantee that there is a positive free energy associated with any phase boundary, the above block matrix  $(\mathbf{K}^{(\sigma\tau)})$  must be positive definite. As a corollary,  $\mathbf{K}^{(\sigma\sigma)}$  must be positive definite for all  $\sigma$  [56]. This is further confirmed in § 2.3.3.

### 2.1.2 Surface free energy

As above, we assume that the surface free energy  $G_{\text{surface}}$  is the surface integral of a well-defined, local surface free energy density  $\gamma$ :

$$G_{\text{surface}}[\{\phi_\alpha\}] = \oint_{\partial V} \gamma(\mathbf{x}, \{\phi_\alpha\}, \{\nabla \phi_\alpha\}, \dots) dA . \quad (2.6)$$

Using the Taylor expansion and chain rule arguments above, we start with the approximation

$$\begin{aligned}\gamma \approx \gamma_{\text{hom}}(\mathbf{x}, \{\phi_\alpha\}) &+ \sum_{\sigma=1}^n \boldsymbol{\Pi}^{(\sigma)}(\mathbf{x}, \{\phi_\alpha\}) \cdot \nabla \phi_\sigma \\ &+ \frac{1}{2} \sum_{\sigma, \tau=1}^n (\nabla \phi_\sigma)^T \cdot \boldsymbol{\kappa}^{(\sigma\tau)}(\mathbf{x}, \{\phi_\alpha\}) \cdot (\nabla \phi_\tau) \\ &+ \sum_{\sigma=1}^n \nabla \cdot \left[ \boldsymbol{\Xi}^{(\sigma)}(\mathbf{x}, \{\phi_\alpha\}) \cdot \nabla \phi_\sigma \right] .\end{aligned}$$

By the divergence theorem (2.2), the integrals of the tangential component of the divergence terms above can be transformed into integrals over the boundary of the surface. However,  $\partial(\partial V) = \emptyset$ , so this integral must be 0. The only non-zero contributions from the divergence terms above are therefore

$$\begin{aligned}\frac{\partial}{\partial n} \left( \hat{\mathbf{n}}^T \cdot \boldsymbol{\Xi}^{(\sigma)} \cdot \nabla \phi_\sigma \right) &= \hat{\mathbf{n}}^T \cdot \left( \frac{\partial \boldsymbol{\Xi}^{(\sigma)}}{\partial n} \right) \cdot \nabla \phi_\sigma + \sum_{\tau=1}^n \frac{\partial \phi_\tau}{\partial n} \hat{\mathbf{n}}^T \cdot \left( \frac{\partial \boldsymbol{\Xi}^{(\sigma)}}{\partial \phi_\tau} \right) \cdot \nabla \phi_\sigma \\ &+ \hat{\mathbf{n}}^T \cdot \boldsymbol{\Xi}^{(\sigma)} \cdot \frac{\partial}{\partial n} \left( \nabla_{\parallel} \phi_\sigma + \frac{\partial \phi_\sigma}{\partial n} \hat{\mathbf{n}} \right)\end{aligned}$$

by the chain rule. The first term may be included in  $\boldsymbol{\Pi}^{(\sigma)}$ , and the summands in the second term may be included in  $\boldsymbol{\kappa}^{(\sigma\tau)}$ . The second-derivative term is therefore reduced to

$$\sum_{\sigma=1}^n \hat{\mathbf{n}}^T \cdot \boldsymbol{\Xi}^{(\sigma)}(\mathbf{x}, \{\phi_\alpha\}) \cdot \frac{\partial}{\partial n} \left( \nabla_{\parallel} \phi_\sigma + \frac{\partial \phi_\sigma}{\partial n} \hat{\mathbf{n}} \right) .$$

Again, we assume the system is symmetric with respect to changes in the sign of derivatives along the surface, so there can be no linear dependence upon tangential gradients. Further, it will be demonstrated below (2.10) that *any* dependence on normal derivatives cannot be allowed. We are therefore left with

$$\gamma(\mathbf{x}, \{\phi_\alpha\}, \{\nabla \phi_\alpha\}) = \gamma_{\text{hom}}(\mathbf{x}, \{\phi_\alpha\}) + \frac{1}{2} \sum_{\sigma, \tau=1}^n (\nabla_{\parallel} \phi_\sigma)^T \cdot \boldsymbol{\kappa}^{(\sigma\tau)}(\mathbf{x}, \{\phi_\alpha\}) \cdot (\nabla_{\parallel} \phi_\tau) . \quad (2.7)$$

As before, we take  $\boldsymbol{\kappa}^{(\sigma\tau)} = (\boldsymbol{\kappa}^{(\tau\sigma)})^T$  for all pairs of indices  $\sigma$  and  $\tau$ . We also take (2.7) to be accurate despite our lack of information about higher-order terms in the Taylor expansion.

In general, surface energies may be orientation dependent. This is allowed for in the above via the dependence of  $\gamma_{\text{hom}}$  and  $\boldsymbol{\kappa}^{(\sigma\tau)}$  on  $\mathbf{x}$ . In cases in which this effect is important, it might be more useful to allow these to be explicit functions of  $\hat{\mathbf{n}}$ , or to make  $\gamma$  a vector [15].

## 2.2 Thermodynamic Potentials

**Extensive** thermodynamic variables are those that depend (usually linearly) on the size of the system or the amount of material in it; examples include the volume of the system and the number of particles of a given species. **Intensive** variables, on the other hand, are scale invariant (pressure and chemical potential, for example). In standard approaches to thermodynamics, every extensive variable  $\phi_\beta$  is associated with a conjugate, intensive variable  $\mu_\beta \equiv \partial G / \partial \phi_\beta$  called a **thermodynamic potential**. This is clearly the change in free energy  $dG$  per unit change in  $\phi_\beta$  for some infinitesimal perturbation  $d\phi_\beta$ , assuming all other thermodynamic variables remain fixed. With free energy functionals, however, the thermodynamic variables are not individual scalars, but rather are fields which vary over space. The partial derivative above is therefore meaningless, and instead the **variational derivative**  $\delta G / \delta \phi_\beta$  must be used.

Suppose that one of the fields  $\phi_\beta(\mathbf{x}, t)$  experiences a small, localized perturbation  $\delta\phi_\beta(\mathbf{x}, t)$  while all other fields remain fixed. Then the resulting change in free energy may be approximated by Taylor expanding  $g$  and  $\gamma$ :

$$\begin{aligned}\delta G &\equiv G[\phi_\beta + \delta\phi_\beta] - G[\phi_\beta] \\ &= \int_V [g(\mathbf{x}, \phi_\beta + \delta\phi_\beta, \nabla\phi_\beta + \nabla\delta\phi_\beta) - g(\mathbf{x}, \phi_\beta, \nabla\phi_\beta)] dV \\ &\quad + \oint_{\partial V} [\gamma(\mathbf{x}, \phi_\beta + \delta\phi_\beta, \nabla\phi_\beta + \nabla\delta\phi_\beta) - \gamma(\mathbf{x}, \phi_\beta, \nabla\phi_\beta)] dA \\ &\approx \int_V \left[ \frac{\partial g}{\partial \phi_\beta} \delta\phi_\beta + (\nabla_p g) \cdot (\nabla \delta\phi_\beta) \right] dV + \oint_{\partial V} \left[ \frac{\partial \gamma}{\partial \phi_\beta} \delta\phi_\beta + (\nabla_p \gamma) \cdot (\nabla \delta\phi_\beta) \right] dA\end{aligned}$$

where, without loss of generality, we have suppressed the dependence on the fixed fields  $\phi_{\alpha \neq \beta}$  in order to minimize notational clutter. Using the multiplication rule (2.1), this can be rewritten

$$\begin{aligned}\delta G &= \int_V \left[ \frac{\partial g}{\partial \phi_\beta} \delta\phi_\beta - \nabla \cdot (\nabla_p g) \delta\phi_\beta + \nabla \cdot (\delta\phi_\beta \nabla_p g) \right] dV \\ &\quad + \oint_{\partial V} \left[ \frac{\partial \gamma}{\partial \phi_\beta} \delta\phi_\beta - \nabla \cdot (\nabla_p \gamma) \delta\phi_\beta + \nabla \cdot (\delta\phi_\beta \nabla_p \gamma) \right] dA.\end{aligned}$$

The divergence term in the volume integral may be rewritten as a surface integral using (2.2). Similarly, the surface integral of the tangential part of the second divergence term

above is 0 by (2.2) since  $\partial(\partial V) = \emptyset$ . Therefore

$$\begin{aligned}\delta G &= \int_V \left[ \frac{\partial g}{\partial \phi_\beta} - \nabla \cdot (\nabla_{\mathbf{p}} g) \right] \delta \phi_\beta dV + \oint_{\partial V} \hat{\mathbf{n}} \cdot (\delta \phi_\beta \nabla_{\mathbf{p}} g) dA \\ &\quad + \oint_{\partial V} \left[ \frac{\partial \gamma}{\partial \phi_\beta} - \nabla \cdot (\nabla_{\mathbf{p}} \gamma) \right] \delta \phi_\beta dA + \oint_{\partial V} \frac{\partial}{\partial n} (\delta \phi_\beta \nabla_{\mathbf{p},\perp} \gamma) dA.\end{aligned}$$

Using the chain rule, terms from the last two integrands may be combined

$$\begin{aligned}& \left[ -\nabla \cdot (\nabla_{\mathbf{p}} \gamma) \right] \delta \phi_\beta + \frac{\partial}{\partial n} \left( \delta \phi_\beta \nabla_{\mathbf{p},\perp} \gamma \right) \\ &= \left[ -\nabla_{\parallel} \cdot (\nabla_{\mathbf{p},\parallel} \gamma) - \frac{\partial}{\partial n} (\nabla_{\mathbf{p},\perp} \gamma) \right] \delta \phi_\beta + \left( \frac{\partial \delta \phi_\beta}{\partial n} \right) \nabla_{\mathbf{p},\perp} \gamma + \delta \phi_\beta \frac{\partial}{\partial n} \left( \nabla_{\mathbf{p},\perp} \gamma \right) \\ &= \left[ -\nabla_{\parallel} \cdot (\nabla_{\mathbf{p},\parallel} \gamma) \right] \delta \phi_\beta + \left( \frac{\partial \delta \phi_\beta}{\partial n} \right) \nabla_{\mathbf{p},\perp} \gamma.\end{aligned}$$

This leaves the final form for the free energy variation

$$\begin{aligned}\delta G &= \int_V \left[ \frac{\partial g}{\partial \phi_\beta} - \nabla \cdot (\nabla_{\mathbf{p},\beta} g) \right] \delta \phi_\beta dV \\ &\quad + \oint_{\partial V} \left[ \hat{\mathbf{n}} \cdot \nabla_{\mathbf{p},\beta} g + \frac{\partial \gamma}{\partial \phi_\beta} - \nabla_{\parallel} \cdot (\nabla_{\mathbf{p},\parallel,\beta} \gamma) \right] \delta \phi_\beta dA \\ &\quad + \oint_{\partial V} \left( \frac{\partial \delta \phi_\beta}{\partial n} \right) \nabla_{\mathbf{p},\perp,\beta} \gamma dA.\end{aligned}\tag{2.8}$$

Note that we have re-introduced the  $\beta$ -dependent notation.

In most introductory discussions of the calculus of variations, it is assumed that the perturbation is so small relative to the volume of the system that  $\delta \phi_\beta$  and its derivatives are all equal to 0 at the boundaries. In this case, both boundary integrals in (2.8) vanish. The bracketed term of the volume integral in (2.8) may be moved outside the integral if it is effectively constant over the support of  $\delta \phi_\beta$ , i.e. if the perturbation is very localized. Then the change in free energy per unit change  $\int_V \delta \phi_\beta dV$  is the *bulk* thermodynamic potential

$$\mu_\beta = \frac{\delta G}{\delta \phi_\beta} \equiv \frac{\partial g}{\partial \phi_\beta} - \nabla \cdot (\nabla_{\mathbf{p},\beta} g).\tag{2.9}$$

Notice that if  $g$  does not depend on the derivatives of  $\phi_\beta$ , then the usual potential  $\partial g / \partial \phi_\beta$  is recovered.

In a bounded, open system, one must also consider perturbations which occur near the boundaries, and therefore cannot always assume that  $\delta \phi_\beta$  and its derivatives vanish there. However, doing so introduces a discontinuity in the thermodynamic potential field at the

system boundary. As we will discuss in § 2.4.1, gradients in thermodynamic potentials drive fluxes of the conserved quantities, so a discontinuity in the potential field would be instantly ameliorated by an infinite flux. We therefore assume that the boundary integrals add to 0.

In the last term of (2.8),  $\delta\phi_\beta$  is being differentiated with respect to a direction which is normal to the surface over which it is being integrated. Consequently, this term cannot be simplified using integration by parts, so it must be handled separately from the other boundary integral. We must therefore assume that

$$\nabla_{\mathbf{p},\perp,\beta}\gamma = 0 , \quad (2.10)$$

i.e. that the surface free energy density does not depend on normal components of gradients. Higher-order normal derivatives would cause similar problems, which is why they too were excluded from (2.7)). Then we simply take

$$\hat{\mathbf{n}} \cdot (\nabla_{\mathbf{p},\beta}g) + \frac{\partial\gamma}{\partial\phi_\beta} - \nabla_{\parallel} \cdot (\nabla_{\mathbf{p},\parallel,\beta}\gamma) = 0 \quad (2.11)$$

as a boundary condition. With these two restrictions, (2.9) gives the thermodynamic potential in the bulk and near the boundaries.

For non-conserved quantities, one cannot make the physical argument that there should be no discontinuities in the potential field. Moreover, even for conserved quantities, one could choose a consistent set of perturbations such that the  $\delta G$  computed above does not suffer a discontinuity at the boundary. However, other arguments can be made for both of these conditions based on steady-state (§ 2.3) or global (§ 2.4.2) considerations. Therefore, for both conserved and non-conserved quantities, we will assume that  $\gamma$  satisfies (2.10) and that the field satisfies the boundary condition (2.11). Thus (2.9) will always be the thermodynamic potential at all points in the bulk and the boundary of the system.

The above formulas hold for any free energy density functions as long as they depend on at most first derivatives of the thermodynamic fields. In particular, for the free energy densities (2.5) and (2.7) derived earlier, the explicit thermodynamic potential is

$$\mu_\beta(\mathbf{x}, t) = \frac{\partial g_{\text{hom}}}{\partial\phi_\beta} + \frac{1}{2} \sum_{\sigma,\tau=1}^n (\nabla\phi_\sigma)^T \cdot \frac{\partial \mathbf{K}^{(\sigma\tau)}}{\partial\phi_\beta} \cdot (\nabla\phi_\tau) - \sum_{\sigma=1}^n \nabla \cdot (\mathbf{K}^{(\beta\sigma)} \nabla\phi_\sigma) \quad (2.9')$$

and the boundary condition is

$$\begin{aligned} & \sum_{\sigma=1}^n \hat{\mathbf{n}} \cdot (\mathbf{K}^{(\beta\sigma)} \nabla\phi_\sigma) + \frac{\partial\gamma_{\text{hom}}}{\partial\phi_\beta} \\ & + \frac{1}{2} \sum_{\sigma,\tau=1}^n (\nabla_{\parallel}\phi_\sigma)^T \cdot \frac{\partial \boldsymbol{\kappa}^{(\sigma\tau)}}{\partial\phi_\beta} \cdot (\nabla_{\parallel}\phi_\tau) - \sum_{\sigma=1}^n \nabla_{\parallel} \cdot (\boldsymbol{\kappa}^{(\beta\sigma)} \nabla_{\parallel}\phi_\sigma) = 0 . \end{aligned} \quad (2.11')$$

Something like this condition is almost universally employed in Cahn-Hilliard or Allen-

Cahn analyses of bounded systems. Some mathematicians just use the Neumann condition  $\hat{\mathbf{n}} \cdot \nabla \phi_\beta = 0$  to simplify their proofs. Others use the full condition (2.11) because it is “natural” for the variational problem; thus it is often called the **variational boundary condition**. Finally, some physically-oriented papers use it because it guarantees that the free energy of a closed system is monotonically decreasing (see § 2.4.2). The above justification is novel, but physically plausible, at least for conserved fields.

## 2.3 Steady States

Though we are primarily interested in time-dependent behavior, it is often useful to solve for steady states, as well. Several conditions for such states can be derived using only the variational methods discussed above.

### 2.3.1 Energy extremizing states

Consider the state of a system as a point in an infinite-dimensional landscape of free energy. If the system is at a local minimum (corresponding to a **metastable** or **equilibrium** state), then the change in free energy resulting from any sufficiently small perturbation of the thermodynamic fields must be positive. If we consider highly-localized, bulk perturbations to a single  $\phi_\beta$  as discussed above, then  $\delta G = \int_V \mu_\beta \delta \phi_\beta dV$  by (2.8) and (2.9). If  $\mu_\beta \neq 0$  at any point, then one can choose a  $\delta \phi_\beta$  which is localized around this point and has the opposite arithmetic sign as  $\mu_\beta$  there. But then  $\delta G < 0$ , contradicting the minimality of the system’s free energy. Therefore, the following must hold:

$$\mu_\beta(\mathbf{x}) = 0 \quad \forall \mathbf{x} \in V \quad \text{and} \quad \forall \beta . \quad (2.12)$$

Note that this argument (that  $\int_V \mu_\beta \delta \phi_\beta dV = 0 \forall \delta \phi_\beta$  implies that  $\mu_\beta$  must be zero) can be proven rigorously. It is sometimes called the “Fundamental Lemma of Variational Calculus” [44]. Also, by definition of  $\mu_\beta$  in Eq. 2.9, (2.12) is a second-order differential equation; it is known as the **Euler-Lagrange equation** from the calculus of variations, and could have been quoted directly as a condition for minimizing the free energy functional.

If the system is truly at a free energy minimum, then  $\delta G > 0$  must also hold for perturbations which do not necessarily vanish at the boundaries. Consider the class of perturbations which are highly localized near the boundaries, but for which  $\partial(\delta \phi_\beta)/\partial n = 0$  on  $\partial V$ . Then the third integral in (2.8) is 0, and the first integral is 0 by (2.12). The free energy variation may therefore be written  $\delta G = \oint_{\partial V} [\hat{\mathbf{n}} \cdot \nabla_{\mathbf{p},\beta} g + \partial \gamma / \partial \phi_\beta - \nabla_{\parallel,\beta} \cdot (\nabla_{\mathbf{p},\parallel,\beta} \gamma)] \delta \phi_\beta dA$ . As above, unless the term in brackets is identically 0 over the entire boundary, then one can generate a perturbation for which  $\delta G < 0$ . Therefore, any state which is at a free energy minimum must satisfy the variational boundary condition (2.11).

Finally, using (2.12) and (2.11) to simplify (2.8) yields  $\delta G = \oint_{\partial V} (\partial \delta \phi_\beta / \partial n) \nabla_{\mathbf{p},\perp,\beta} \gamma dA$ . Again, if  $\nabla_{\mathbf{p},\perp,\beta} \gamma$  is non-zero at any point on the boundary, then one can create a perturbation whose normal derivative is of the opposite sign around that point, yielding  $\delta G < 0$ .

Therefore, any minimum energy state must also satisfy (2.10).

Note that the arguments above can also be used to identify energy-maximizing states. More generally, (2.12), (2.10), and (2.11) are conditions for any **critical state**—minimum, maximum, or saddle—about which infinitesimal perturbations yield no first-order change in free energy. Moreover, these are only *necessary* conditions; see § 2.3.3 for *sufficient* conditions.

### 2.3.2 Constrained extremizing states

Of course, a real system cannot necessarily be perturbed arbitrarily. For example, if  $c_\beta$  is a conserved thermodynamic field, then the total quantity  $\int c_\beta dV$  cannot change spontaneously without fluxes into or out of the system via the external environment. We therefore define a **stable state** as one for which any sufficiently small, *allowable* perturbation results in a positive free energy change. Of course, such a state might still be an absolute minimizer of the free energy as considered above; however, it is only required that it be a minimizer with respect to the constrained set of allowable perturbations.

In general, there are no constraints on the infinitesimal perturbations of non-conserved quantities, so the conclusions from the previous section—and specifically Eq. 2.12—are still required. For a conserved quantity  $c_\beta$ , however, bulk perturbations (i.e. those which do not involve boundary fluxes) must satisfy  $\int_V \delta c_\beta dV = 0$ . We again apply (2.8) for perturbations which vanish on the boundary to get  $\delta G = \int_V \mu_\beta \delta c_\beta dV$ . If there exists a small, connected set in  $V$  over which  $\mu_\beta$  is non-constant, then one could construct a perturbation  $\delta c_\beta$  confined to this set for which  $\delta G < 0$ . This contradicts the above definition of a stable state, so  $\mu_\beta$  must be constant on every connected set in  $V$ . We only work with connected geometries; in this case, then,  $\mu_\beta$  must be constant over all of  $V$ . Note that this conclusion is essentially just another form of the Fundamental Lemma of Variational Calculus [44]. It also follows more abstractly by the method of Lagrange multipliers—specialized to the variational setting [103, 44]—in which one extremizes the free energy functional subject to the constraint that  $\int_V c_\beta dV$  is fixed.

As in the previous section, we also require  $\delta G \geq 0$  for perturbations at the boundaries. Thus, even before considering constitutive relations for our fluxes, we can conclude that (2.10) must hold in order for stable states to exist, and such states must satisfy the variational boundary condition (2.11).

We have so far only considered bulk fluctuations. If fluxes of the conserved quantity are allowed between the system and its external environment, then perturbations in the form of small fluxes must also be considered. However, this is a more classical problem, and it is well-known [41] that the system-universe interface will be stable to such variations as long as the thermodynamic potentials of  $c_\beta$  in the system and the external universe are the same. Thus,  $\mu_{\beta,\text{ext}} = \mu_{\beta,0}$  must hold for the thermodynamic potential of  $c_\beta$  near, but outside, the boundaries.

To summarize, a necessary condition on the conserved fields for a stable state is

$$\exists \mu_{\beta,0} \in \mathbb{R} \quad \text{such that} \quad \mu_{\beta}(\mathbf{x}) = \mu_{\beta,0} \quad \forall \mathbf{x} \in V , \quad (2.13a)$$

$$\mu_{\beta,\text{ext}} = \mu_{\beta,0} \quad \text{just outside of } V . \quad (2.13b)$$

As before, it takes the form of a second-order differential equation (though because of the possibly non-zero constant  $\mu_{\beta,0}$ , this is not the Euler-Lagrange equation). It is an important fact that, in general, there exist non-uniform solutions  $c_{\beta}(\mathbf{x})$  to the equation  $\mu_{\beta}(\mathbf{x}) = \mu_{\beta,0}$ , even for non-zero  $\mu_{\beta,0}$ . See Fig. 2-1 for an example.

## The Beltrami identity

By using the equality of mixed partials  $\partial^2 \phi_{\sigma} / \partial x_i \partial x_j = \partial^2 \phi_{\sigma} / \partial x_j \partial x_i$ , the gradient of  $g$  may be written

$$\nabla g = \nabla_{\mathbf{x}} g + \sum_{\sigma=1}^n \left\{ \frac{\partial g}{\partial \phi_{\sigma}} \nabla \phi_{\sigma} + [(\nabla_{\mathbf{p},\sigma} g) \cdot \nabla] \nabla \phi_{\sigma} \right\} .$$

Using (2.9), the necessary condition for an extremal state may be written

$$\frac{\partial g}{\partial \phi_{\sigma}} = \mu_{\sigma,0} + \nabla \cdot (\nabla_{\mathbf{p},\sigma} g)$$

(we must take  $\mu_{\sigma,0}$  to be 0 for non-conserved quantities). Substituting this into the gradient above yields

$$\nabla \left[ g - \sum_{\sigma=1}^n \mu_{\sigma,0} \phi_{\sigma} \right] = \nabla_{\mathbf{x}} g + \sum_{\sigma=1}^n \left\{ [\nabla \cdot (\nabla_{\mathbf{p},\sigma} g)] \nabla \phi_{\sigma} + [(\nabla_{\mathbf{p},\sigma} g) \cdot \nabla] \nabla \phi_{\sigma} \right\}$$

(using the fact that each  $\mu_{\sigma,0}$  is a constant). Finally, using the identities

$$\begin{aligned} \nabla \cdot (\mathbf{A} \otimes \mathbf{B}) &= (\nabla \cdot \mathbf{A}) \mathbf{B} + (\mathbf{A} \cdot \nabla) \mathbf{B} \\ \nabla s &= \nabla \cdot (s \mathbf{I}) \end{aligned}$$

for any vector fields  $\mathbf{A}$  and  $\mathbf{B}$  and scalar field  $s$  ( $\otimes$  denotes the tensor, or outer, product of two vectors, and  $\mathbf{I} = \delta_{ij}$  is the Kronecker delta tensor) allows us to write

$$\nabla \cdot \left[ \left( g - \sum_{\sigma=1}^n \mu_{\sigma,0} \phi_{\sigma} \right) \mathbf{I} - \sum_{\sigma=1}^n (\nabla_{\mathbf{p},\sigma} g) \otimes (\nabla \phi_{\sigma}) \right] = \nabla_{\mathbf{x}} g . \quad (2.14)$$

This is a generalization of **Noether's equation** from the calculus of variations [44].

In the typical case in which  $g$  does not depend explicitly on  $\mathbf{x}$  (i.e.  $\nabla_{\mathbf{x}} g = \mathbf{0}$ ), the tensor in brackets in (2.14) is divergence-free. In the 1-dimensional case ( $d = 1$ ), then, Noether's

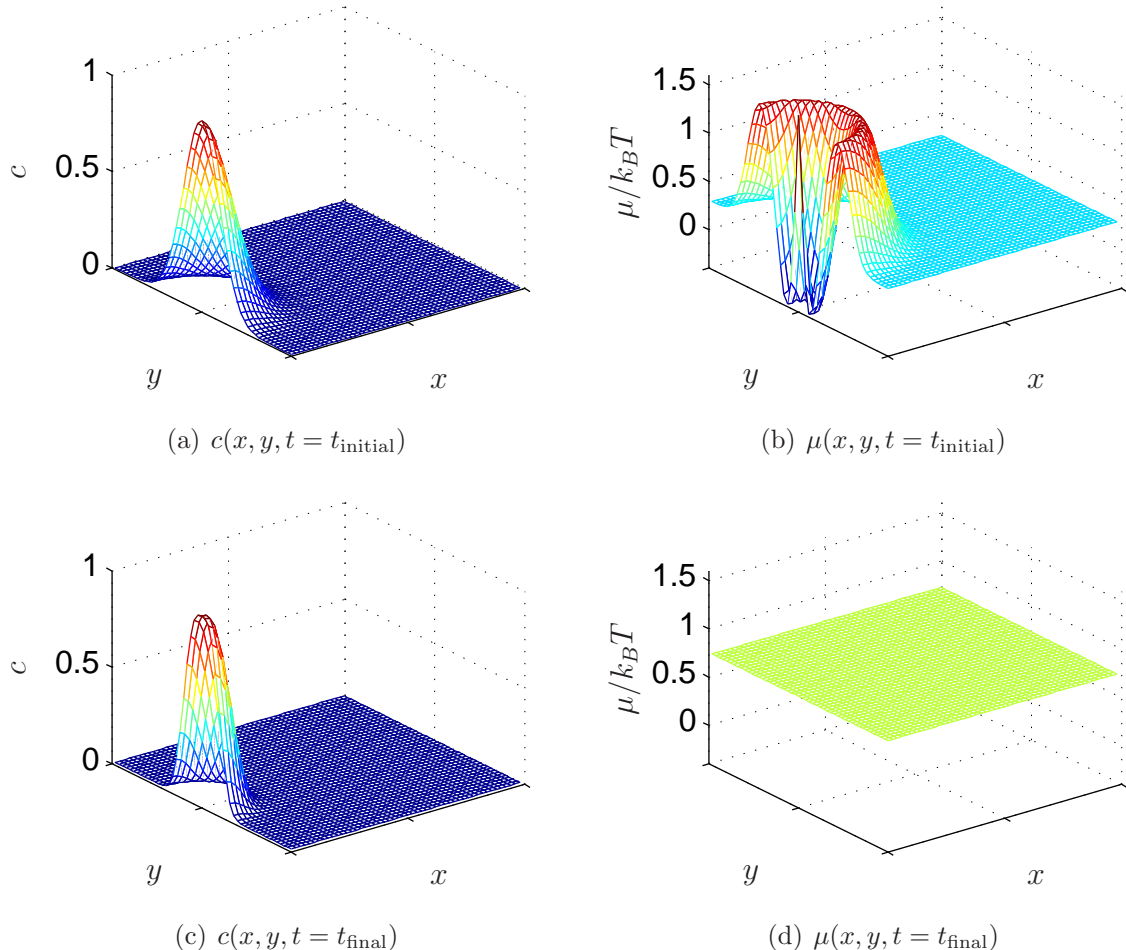


Figure 2-1: Simulation results demonstrating that an equilibrium concentration field can be non-uniform but still have a uniform, non-zero thermodynamic potential. The free energy density was assumed to satisfy (2.5) with non-dimensional homogeneous free energy density  $g_{\text{hom}}(c) = 5c(1 - c) + c \log(c) + (1 - c) \log(1 - c)$  and non-dimensional gradient-penalty tensor equal to the identity. Top row: initial condition. Bottom row: final state after a long relaxation period.

equation may be integrated to get

$$g - \sum_{\sigma=1}^n \frac{\partial g}{\partial(\partial\phi_\sigma/\partial x)} \frac{\partial\phi_\sigma}{\partial x} - \sum_{\sigma=1}^n \mu_{\sigma,0}\phi_\sigma = C \quad (2.15)$$

for some constant  $C$ . This is a generalization of the **Beltrami identity** from the calculus of variations. Note in particular that if we have only a single thermodynamic field (so  $n = 1$ ), then our necessary condition for a steady state has been simplified from a second-order to a first-order ODE.

The Beltrami identity is extremely specialized: one cannot usually find a first integral of the necessary condition in higher dimensions even when strong symmetry conditions apply. For example, even if we assume that  $\nabla_{\mathbf{x}}g = \mathbf{0}$ , that every  $\phi_\sigma$  is a function only of the radius  $r$  in polar ( $d = 2$ ) or spherical ( $d = 3$ ) coordinates, and that  $\nabla_{\mathbf{p},\sigma}g = (\partial\phi_\sigma/\partial r)\hat{\mathbf{r}}$  for each  $\sigma$ , then (2.14) is simply

$$\frac{\partial}{\partial r} \left[ g - \sum_{\sigma=1}^n \mu_{\sigma,0}\phi_\sigma \right] = \frac{1}{r^{d-1}} \frac{\partial}{\partial r} \left[ r^{d-1} \sum_{\sigma=1}^n \left( \frac{\partial\phi_\sigma}{\partial r} \right)^2 \right]$$

which cannot necessarily be written in closed form as a derivative with respect to  $r$ . Note that (2.14) is integrable if all variables are functions only of the angle in polar coordinates or the longitude in spherical coordinates; however, these are atypical symmetries in diffusion problems.

### Infinite 1-dimensional geometries

We now specialize to free energy densities of the form (2.5) in  $d = 1$  spatial dimension and with  $n = 1$  thermodynamic field (so we can drop the superscripts and subscripts identifying the field). The necessary condition for a steady state is then

$$g_{\text{hom}}(\phi(x)) - \frac{1}{2}K(\phi(x)) \left( \frac{\partial\phi}{\partial x} \right)^2 - \mu_0\phi(x) = C \quad (2.15')$$

subject to the Neumann conditions  $\partial\phi/\partial x = 0$  at the boundaries. This is equivalent to the derivation in mechanics that the Hamiltonian is conserved if the Lagrangian is not explicitly a function of time.

We first consider an infinite geometry, and assume that the limits

$$\begin{aligned} \phi_{\text{lower}} &\equiv \lim_{x \rightarrow -\infty} \phi(x) \\ \phi_{\text{upper}} &\equiv \lim_{x \rightarrow +\infty} \phi(x) \end{aligned}$$

both exist. In a two-phase system, we may assume without loss of generality that  $\phi_{\text{lower}} < \phi_{\text{upper}}$ . Far away from the interphase boundary,  $\phi'(x)$  and  $\phi''(x)$  should both tend to 0. Then by (2.9) the potential must be  $\mu_0 = g'_{\text{hom}}(\phi_{\text{lower}}) = g'_{\text{hom}}(\phi_{\text{upper}})$  (this is just the

classical **common tangent construction**), and by (2.15') the integration constant must be  $C = g_{\text{hom}}(\phi_{\text{lower}}) - \mu_0 \phi_{\text{lower}} = g_{\text{hom}}(\phi_{\text{upper}}) - \mu_0 \phi_{\text{upper}}$ . If we then seek some asymptotic approximation  $\phi(x) \sim \phi_{\text{lower}} + \varepsilon(x)$  as  $x \rightarrow -\infty$ , we can expand (2.15') to get the ODE

$$\frac{1}{2}g''_{\text{hom}}(\phi_{\text{lower}})\varepsilon(x)^2 - \frac{1}{2}K(\phi_{\text{lower}})\varepsilon'(x)^2 = 0 .$$

The non-constant solutions of this equation which decay as  $x \rightarrow -\infty$  are given by

$$\varepsilon(x) = \exp\left(\sqrt{\frac{g''_{\text{hom}}(\phi_{\text{lower}})}{K(\phi_{\text{lower}})}}(x - x_0)\right)$$

for any constant  $x_0$ . Thus, the decay away from the interphase boundary towards  $x = -\infty$  is exponential with an associated length scale of  $\sqrt{K(\phi_{\text{lower}})/g''_{\text{hom}}(\phi_{\text{lower}})}$ . Similarly, the approach towards  $\phi_{\text{upper}}$  as  $x \rightarrow +\infty$  is exponential with length scale  $\sqrt{K(\phi_{\text{upper}})/g''_{\text{hom}}(\phi_{\text{lower}})}$ . The interphase boundary—defined as the region in which  $\phi$  changes rapidly—is therefore exponentially sharp, and so effectively finite in extent. Beyond this region, the system is considered to be in one of the “pure phases”  $\phi \approx \phi_{\text{lower}}$  or  $\phi \approx \phi_{\text{upper}}$ .

In the interphase region, there must be some inflection point  $x_{\text{inf}}$  at which  $\phi''(x_{\text{inf}}) = 0$ . At this point, the slope of the curve  $\phi(x)$  is at a maximum. Define  $\phi_{\text{inf}} \equiv \phi(x_{\text{inf}})$ ; as long as  $K$  and  $g_{\text{hom}}$  are known functions of  $\phi$ ,  $\phi_{\text{inf}}$  can be computed in terms of  $\phi_{\text{lower}}$  or  $\phi_{\text{upper}}$ . From (2.15') and using the fact that  $C = g_{\text{hom}}(\phi_{\text{lower}}) - \mu_0 \phi_{\text{lower}}$ , the maximum slope of the curve is evidently

$$\phi'(x_{\text{inf}}) = \sqrt{\frac{2[g_{\text{hom}}(\phi_{\text{inf}}) - g_{\text{hom}}(\phi_{\text{lower}}) - \mu_0(\phi_{\text{inf}} - \phi_{\text{lower}})]}{K(\phi_{\text{inf}})}} .$$

Taking this slope to equal  $(\phi_{\text{upper}} - \phi_{\text{lower}})/w$  where  $w$  is a characteristic width of the interphase region, we see that

$$w = (\phi_{\text{upper}} - \phi_{\text{lower}}) \sqrt{\frac{K(\phi_{\text{inf}})}{2[g_{\text{hom}}(\phi_{\text{inf}}) - g_{\text{hom}}(\phi_{\text{lower}}) - \mu_0(\phi_{\text{inf}} - \phi_{\text{lower}})]}} .$$

This is the source of the general rule for phase-field models like ours that the gradient penalty tensor divided by some typical energy scale gives the square of the typical lengths for the interphase width (though this could also be argued for on purely dimensional grounds, as well). This rule is extended to higher dimensions by considering the eigenvalues of the gradient penalty tensor.

There is a special case for which the Beltrami identity can be solved exactly. Suppose that  $K$  is constant and  $g_{\text{hom}}$  is given by the Landau free energy  $g_{\text{hom}}(\phi) = \frac{1}{2}E(1 - \phi^2)^2$  for some positive constant  $E$  (this is the simplest double-welled free energy function). Then the common tangent construction requires  $\phi_{\text{lower}} = -1$ ,  $\phi_{\text{upper}} = +1$ , and  $\mu_0 = 0$ . The Beltrami

identity then becomes  $\frac{1}{2}E(1 - \phi^2)^2 - \frac{1}{2}K(\phi')^2 = 0$ , which has solutions of the form

$$\phi(x) = \tanh\left(\sqrt{\frac{E}{K}}(x - x_0)\right)$$

for any constant  $x_0$ . Notice that the phase boundary is centered at  $x_0$ , and is exponentially sharp with characteristic width  $\sqrt{K/E}$ .

### Finite 1-dimensional geometries

In a bounded system (say  $V = [x_{\text{lower}}, x_{\text{upper}}]$ ), we may define the quantities  $\phi_{\text{lower}} \equiv \phi(x_{\text{lower}})$  and  $\phi_{\text{upper}} \equiv \phi(x_{\text{upper}})$  directly rather than via limits. If we ignore surface energies, then the variational boundary condition (2.11) is simply  $\phi'(x_{\text{lower}}) = \phi'(x_{\text{upper}}) = 0$ . However, the system might not have sufficient room for the second derivatives to also reach 0 at the boundaries. Therefore the common tangent construction is not exactly applicable, and no simple statements like those above can be made.

#### 2.3.3 Energy minimizing states

None of the conditions derived above are sufficient to guarantee that a given state is a local minimum. As with ordinary differential calculus in which the second derivative must be employed to classify critical points, one must examine higher-order changes in  $G$  in order to classify the critical states.

In deriving the thermodynamic potential, we started by expanding  $g$  and  $\gamma$  in a Taylor series and keeping only the first-order terms. If instead we keep terms up to second-order, we get

$$G[\phi_\beta + \delta\phi_\beta] - G[\phi_\beta] \approx \delta G + \delta^2 G ,$$

where  $\delta G$ , given by (2.8), is 0 for critical states, and

$$\begin{aligned} \delta^2 G &\equiv \int_V \left\{ \left( \frac{\partial^2 g}{\partial \phi_\beta^2} \right) (\delta\phi_\beta)^2 + \left( \frac{\partial}{\partial \phi_\beta} \nabla_{\mathbf{p},\beta} g \right) \cdot (\delta\phi_\beta \nabla \delta\phi_\beta) \right. \\ &\quad \left. + (\nabla \delta\phi_\beta)^T \cdot (\nabla_{\mathbf{p},\beta} \nabla_{\mathbf{p},\beta} g) \cdot (\nabla \delta\phi_\beta) \right\} dV \\ &+ \oint_{\partial V} \left\{ \left( \frac{\partial^2 \gamma}{\partial \phi_\beta^2} \right) (\delta\phi_\beta)^2 + \left( \frac{\partial}{\partial \phi_\beta} \nabla_{\mathbf{p},\beta} \gamma \right) \cdot (\delta\phi_\beta \nabla \delta\phi_\beta) \right. \\ &\quad \left. + (\nabla \delta\phi_\beta)^T \cdot (\nabla_{\mathbf{p},\beta} \nabla_{\mathbf{p},\beta} \gamma) \cdot (\nabla \delta\phi_\beta) \right\} dA \end{aligned} \tag{2.16}$$

is the **second variation** of  $G$ . Then if  $\delta^2 G > 0$  for all allowable perturbations  $\delta\phi_\beta$ , the critical state is a true local minimum (though this problem requires more care about the

space of allowable perturbations [44]).

In general, this is an integro-differential inequality that must hold for all allowable perturbations. Unlike in previous sections in which “allowable” simply meant  $\int_V \delta c_\beta dV = 0$  for perturbations to conserved fields, we must now also restrict ourselves to perturbations which maintain the boundary conditions (2.11). Proving this inequality is therefore almost impossibly difficult for general critical states.

We first note that it is proven in [36] that if  $\delta^2 G > 0$ , then  $\nabla_{\mathbf{p},\beta} \nabla_{\mathbf{p},\beta} g$  must be positive definite at every point in  $V$ . If we use the free energy density derived earlier (2.5), then  $\nabla_{\mathbf{p},\beta} \nabla_{\mathbf{p},\beta} g = \mathbf{K}^{(\beta\beta)}$ . This is the rigorous, mathematical proof that  $\mathbf{K}^{(\beta\beta)}$  must be positive definite: it is required in order for a minimum-energy state to exist.

We can only make further progress at the expense of being overly strict. In general, the integrands in (2.16) may be negative at some points in  $V$  and still satisfy  $\delta^2 G > 0$ . However,  $\delta^2 G$  is obviously positive if the integrands happen to be pointwise positive. Consider the integrand of the volume integral in (2.16). It may be written as a binary quadratic form:

$$(\delta\phi_\beta \quad (\nabla\phi_\beta)^T) \cdot \begin{pmatrix} \partial^2 g / \partial\phi_\beta^2 & \frac{1}{2} \left( \frac{\partial}{\partial\phi_\beta} \nabla_{\mathbf{p},\beta} g \right)^T \\ \frac{1}{2} \frac{\partial}{\partial\phi_\beta} \nabla_{\mathbf{p},\beta} g & \nabla_{\mathbf{p},\beta} \nabla_{\mathbf{p},\beta} g \end{pmatrix} \cdot \begin{pmatrix} \delta\phi_\beta \\ (\nabla\phi_\beta)^T \end{pmatrix} .$$

If we take  $g$  to be given by (2.5) and assume only that  $\partial\mathbf{K}^{(\beta\sigma)} / \partial\phi_\beta = \mathbf{0}$  for all  $\sigma$ , then this may be written

$$(\delta\phi_\beta \quad (\nabla\phi_\beta)^T) \cdot \begin{pmatrix} \partial^2 g_{\text{hom}} / \partial\phi_\beta^2 & \mathbf{0}^T \\ \mathbf{0} & \mathbf{K}^{(\beta\beta)} \end{pmatrix} \cdot \begin{pmatrix} \delta\phi_\beta \\ (\nabla\phi_\beta)^T \end{pmatrix} .$$

We already know that  $\mathbf{K}^{(\beta\beta)}$  must be positive definite. Therefore, the above form is positive definite if and only if  $\partial^2 g_{\text{hom}} / \partial\phi_\beta^2 > 0$  [56]. The same computation can be done for the surface integral in (2.16). Therefore,

$$\forall \beta, \quad \frac{\partial^2 g_{\text{hom}}}{\partial\phi_\beta^2} > 0 \quad \forall \mathbf{x} \in V \quad \text{and} \quad \frac{\partial^2 \gamma_{\text{hom}}}{\partial\phi_\beta^2} \geq 0 \quad \forall \mathbf{x} \in \partial V \quad (2.17)$$

is a sufficient condition for a critical state to be a stable energy minimizer. We will see in Chapter 8 that this is, indeed, overly strict.

## 2.4 Dynamic Approach to Equilibrium

Though we have found several simple relations that must hold at equilibrium, we have said nothing about the out-of-equilibrium dynamics. To do so, we must postulate certain phenomenological relations for the kinetics. We will present the standard assumptions in general form, and demonstrate several nice properties thereof.

### 2.4.1 Kinetic equations

Every conserved field must satisfy the local conservation law

$$\frac{\partial c_\beta}{\partial t} = -\nabla \cdot \mathbf{J}_\beta , \quad (2.18)$$

where  $\mathbf{J}_\beta(\mathbf{x}, t)$  is a field of flux vectors for quantities of type  $\beta$ . In general, this vector cannot be computed from first principles, but rather must be assumed to satisfy some phenomenological equation. We will make the standard assumption of non-equilibrium thermodynamics [81, 26] that each flux depends at most linearly on the gradients of the thermodynamic potentials of all of the conserved quantities. Thus, we write

$$\mathbf{J}_\beta(\mathbf{x}, t) = \sum_{\sigma=1}^{n_c} \mathbf{L}^{(\beta\sigma)}(\mathbf{x}, \{\phi_\alpha\}) \cdot \nabla \mu_\sigma , \quad (2.19)$$

where the sum is taken over all conserved fields. The second-rank tensors  $\mathbf{L}^{(\beta\sigma)}$  are called **Onsager coefficients**. When  $c_\beta$  is the concentration field for a chemical species, one usually writes  $\mathbf{L}^{(\beta\beta)} = c_\beta \mathbf{B}_\beta$  where  $\mathbf{B}_\beta$  is the **mobility tensor** for species  $\beta$ ; thus, the above is essentially a generalization of Fick's first law and the Nernst-Planck equation.

For non-conserved quantities, the form of the kinetic equations are non-obvious given that the fields themselves are usually phenomenological order parameters. However, we follow a common generalization of the original Allen-Cahn equation [3] in assuming that

$$\frac{\partial \eta_\beta}{\partial t} = - \sum_{\sigma=1}^{n_n} \Lambda^{(\beta\sigma)}(\mathbf{x}, \{\phi_\alpha\}) \mu_\sigma , \quad (2.20)$$

where the sum is taken over all non-conserved fields. The scalars  $\Lambda^{(\beta\sigma)}$  are called **generalized Onsager coefficients**. This is not physically-motivated, but is rather assumed as the simplest kinetic equation which is consistent with the Second Law of Thermodynamics (see § 2.4.2).

### 2.4.2 Global time derivatives

For any conserved field  $c_\beta$ , define the total content of type  $\beta$  by

$$Q_\beta(t) \equiv \int_V c_\beta(\mathbf{x}, t) dV . \quad (2.21)$$

Then clearly

$$\frac{dQ_\beta}{dt} = - \oint_{\partial V} \hat{\mathbf{n}} \cdot \mathbf{J}_\beta dA \quad (2.22)$$

using only the divergence theorem (2.2) and the local conservation law (2.18). This is intuitively obvious: the only way the total content of the system can change is via a flux

through the boundary. Note that the integral conservation law (2.22) is more fundamental than, and is typically used to derive, the local conservation law (2.18), not vice versa.

Computing the time derivative of the total free energy of the system requires a bit more care. By the chain rule,

$$\begin{aligned}\frac{dG}{dt} &= \int_V \frac{\partial g}{\partial t} dV + \oint_{\partial V} \frac{\partial \gamma}{\partial t} dA \\ &= \int_V \sum_{\sigma=1}^n \left[ \frac{\partial g}{\partial \phi_\sigma} \frac{\partial \phi_\sigma}{\partial t} + (\nabla_{\mathbf{p},\sigma} g) \cdot \nabla \left( \frac{\partial \phi_\sigma}{\partial t} \right) \right] dV \\ &\quad + \oint_{\partial V} \sum_{\sigma=1}^n \left[ \frac{\partial \gamma}{\partial \phi_\sigma} \frac{\partial \phi_\sigma}{\partial t} + (\nabla_{\mathbf{p},\sigma} \gamma) \cdot \nabla \left( \frac{\partial \phi_\sigma}{\partial t} \right) \right] dA.\end{aligned}$$

Then following the same sequence of steps used to derive (2.8), we see that

$$\begin{aligned}\frac{dG}{dt} &= \int_V \sum_{\sigma=1}^n \left[ \frac{\partial g}{\partial \phi_\sigma} - \nabla \cdot (\nabla_{\mathbf{p},\sigma} g) \right] \frac{\partial \phi_\sigma}{\partial t} dV \\ &\quad + \oint_{\partial V} \sum_{\sigma=1}^n \left[ \hat{\mathbf{n}} \cdot \nabla_{\mathbf{p},\sigma} g + \frac{\partial \gamma}{\partial \phi_\sigma} - \nabla_{\parallel} \cdot (\nabla_{\mathbf{p},\parallel,\sigma} \gamma) \right] \frac{\partial \phi_\sigma}{\partial t} dA \\ &\quad + \oint_{\partial V} \sum_{\sigma=1}^n \left( \frac{\partial(\partial \phi_\sigma / \partial t)}{\partial n} \right) \nabla_{\mathbf{p},\perp,\sigma} \gamma dA.\end{aligned}$$

The surface integrals are identically 0 by (2.11) and (2.10). Then using the definition of the thermodynamic potential (2.9), we get the simplified expression

$$\frac{dG}{dt} = \int_V \sum_{\sigma=1}^n \mu_\sigma \frac{\partial \phi_\sigma}{\partial t} dV. \quad (2.23)$$

Given that we defined the thermodynamic potentials to be the change in free energy per unit change in the independent field, this equation makes intuitive sense. However, with a bit more work, a more useful relation can be derived. First, we split the above sum into its non-conserved and conserved components, and we replace the time derivatives using the kinetic equations (2.20) and (2.18):

$$\frac{dG}{dt} = - \int_V \sum_{\sigma,\tau=1}^{n_n} \mu_\sigma \Lambda^{(\sigma\tau)} \mu_\tau dV - \int_V \sum_{\sigma=1}^{n_c} \mu_\sigma \nabla \cdot \mathbf{J}_\sigma dV.$$

The second integral may be rewritten using the multiplication rule (2.1):

$$\frac{dG}{dt} = - \int_V \sum_{\sigma,\tau=1}^{n_n} \mu_\sigma \Lambda^{(\sigma\tau)} \mu_\tau dV + \int_V \sum_{\sigma=1}^{n_c} (\nabla \mu_\sigma) \cdot \mathbf{J}_\sigma dV - \int_V \sum_{\sigma=1}^{n_c} \nabla \cdot (\mu_\sigma \mathbf{J}_\sigma) dV.$$

By the divergence theorem (2.2), the last integral is really a surface integral:

$$\frac{dG}{dt} = - \int_V \sum_{\sigma, \tau=1}^{n_n} \mu_\sigma \Lambda^{(\sigma\tau)} \mu_\tau dV + \int_V \sum_{\sigma=1}^{n_c} (\nabla \mu_\sigma) \cdot \mathbf{J}_\sigma dV - \oint_{\partial V} \sum_{\sigma=1}^{n_c} \mu_\sigma \hat{\mathbf{n}} \cdot \mathbf{J}_\sigma dA .$$

Finally, using the flux equation (2.19) yields

$$\begin{aligned} \frac{dG}{dt} &= - \int_V \sum_{\sigma, \tau=1}^{n_n} \mu_\sigma \Lambda^{(\sigma\tau)} \mu_\tau dV - \int_V \sum_{\sigma, \tau=1}^{n_c} (\nabla \mu_\sigma)^T \cdot \mathbf{L}^{(\sigma\tau)} \cdot (\nabla \mu_\tau) dV \\ &\quad - \oint_{\partial V} \sum_{\sigma=1}^{n_c} \mu_\sigma \hat{\mathbf{n}} \cdot \mathbf{J}_\sigma dA . \end{aligned} \tag{2.24}$$

The first two integrals in this expression quantify the free energy dissipation due to relaxation in the bulk. The third integral is the free energy loss due to the outflow of conserved quantities.

Now suppose that there are no fluxes across the boundary. Then the system is closed, and by the Second Law of Thermodynamics,  $G$  must be non-increasing for any set of initial conditions. Notice that the two volume integrands from (2.24) may be rewritten in block-matrix form:

$$- (\mu_1 \ \mu_2 \ \dots \ \mu_{n_n}) \cdot \begin{pmatrix} \Lambda^{(11)} & \Lambda^{(12)} & \dots & \Lambda^{(1n_n)} \\ \Lambda^{(21)} & \Lambda^{(22)} & \dots & \Lambda^{(2n_n)} \\ \vdots & \vdots & \ddots & \vdots \\ \Lambda^{(n_n 1)} & \Lambda^{(n_n 2)} & \dots & \Lambda^{(n_n n_n)} \end{pmatrix} \cdot \begin{pmatrix} \mu_1 \\ \mu_2 \\ \vdots \\ \mu_{n_n} \end{pmatrix}$$

and

$$- ((\nabla \mu_1)^T \ (\nabla \mu_2)^T \ \dots \ (\nabla \mu_{n_c})^T) \cdot \begin{pmatrix} \mathbf{L}^{(11)} & \mathbf{L}^{(12)} & \dots & \mathbf{L}^{(1n_c)} \\ \mathbf{L}^{(21)} & \mathbf{L}^{(22)} & \dots & \mathbf{L}^{(2n_c)} \\ \vdots & \vdots & \ddots & \vdots \\ \mathbf{L}^{(n_c 1)} & \mathbf{L}^{(n_c 2)} & \dots & \mathbf{L}^{(n_c n_c)} \end{pmatrix} \cdot \begin{pmatrix} \nabla \mu_1 \\ \nabla \mu_2 \\ \vdots \\ \nabla \mu_{n_c} \end{pmatrix} .$$

To ensure that this is non-positive for any set of potentials and their gradients, the above matrix  $(\Lambda^{(\sigma\tau)})$  and block matrix  $(\mathbf{L}^{(\sigma\tau)})$  must both be positive semi-definite. In the typical case in which cross terms  $\Lambda^{(\sigma\tau)}$  and  $\mathbf{L}^{(\sigma\tau)}$  for  $\sigma \neq \tau$  are assumed to be 0, this is equivalent to requiring that  $\Lambda^{(\sigma\sigma)}$  and  $\mathbf{L}^{(\sigma\sigma)}$  be positive semi-definite for all  $\sigma$  [56].

In many treatments of phase-field models, the variational boundary condition (2.11) is only justified as a method to ensure that  $G$  is non-increasing in the absence of boundary fluxes (see, for example, [42]). Many mathematical studies also rely heavily on the condition that  $dG/dt \leq 0$ , i.e. that  $G$  is a **Lyapunov function**. Note, however, that in the general case in which boundary fluxes are allowed, this property does not necessarily hold: even

if the above matrices are positive semi-definite, the boundary integral in (2.24) may force  $dG/dt$  to be positive. While the total free energy of the *universe* is decreasing, the free energy of our particular system may be increasing due to interactions with its surroundings. We always make the positive semi-definiteness assumption above, so there will always be bulk relaxation. However, we can only get a genuine Lyapunov function in the general case by including the free energy of the exterior system (assuming only that the boundary fluxes occur in the direction of decreasing thermodynamic potentials).

### 2.4.3 Boundary conditions

When solving problems in a bounded geometry, the kinetic equations above must be closed by an appropriate number of boundary conditions. By (2.9), the thermodynamic potentials are all functions involving second-order derivatives of the corresponding independent fields. Then the kinetic equation for non-conserved fields (2.20) is also second-order in space, while the equation for conserved fields (2.18) is fourth-order. One therefore needs one condition for non-conserved fields and two for conserved quantities at every point on  $\partial V$  (thus totaling 2 and 4 boundary conditions, respectively).

When standard thermodynamic transport equations are employed, only a single set of boundary conditions is required, and they are usually physically obvious. For example, when using Fourier's law for heat transfer, one might hold the boundaries at a fixed temperature (Dirichlet boundary conditions); or when using Fick's law for diffusion, one might have a condition on the fluxes at the boundaries (Neumann boundary conditions). This is more difficult in the phase-field setting. Non-conserved fields are typically phenomenological order parameters; as such, they have no fluxes, and the physical significance of any particular boundary condition is unclear. One can certainly develop laws for the fluxes of conserved quantities, but as mentioned above, these still must be supplemented by an additional set of boundary conditions.

It is for this reason that we have emphasized the variational boundary condition (2.11) throughout this Chapter. It provides the only boundary condition necessary for non-conserved fields, and it supplements any flux laws for conserved quantities we might have. When trying to generate solutions to any of these partial differential equations in a bounded system, (2.11) is absolutely necessary. This is a non-trivial point: according to Giaquinta and Hildebrandt [44], even Euler and Lagrange were unable to derive these conditions in more than one dimension.

## 2.5 Single-Species Diffusion in a Crystal

Most of this thesis is focused on the case of a single species diffusing through a crystal without significantly affecting the host structure. In this case, the only thermodynamic field is the concentration of the single species. We will specialize to a free energy functional of the form (2.5), so must first discuss its homogeneous component.

Define  $\rho$  to be the site density (in molecules per unit volume) in the crystal, i.e. the density of the diffusing species plus the density of vacancies. We will assume that  $\rho$  is a constant independent of the local concentration (the small dependence present in real systems is usually only important when elastic effects are considered). The scalar field of interest is  $c(\mathbf{x}, t)$ , the local concentration of the diffusing species. Let  $c$  be normalized by  $\rho$ , so it is non-dimensional and only takes values between 0 and 1.

With these definitions, a common assumption for the homogeneous free energy is that it obeys the **regular solution model** [84]:

$$g_{\text{hom}}(c) = g_L \rho c + g_F \rho (1 - c) + a \rho c (1 - c) + \rho k_B T [c \log c + (1 - c) \log(1 - c)] . \quad (2.25)$$

Here  $g_L$  is the chemical potential of a crystal completely filled with the diffusing species (e.g., pure LiFePO<sub>4</sub>);  $g_F$  is the chemical potential of a crystal completely devoid of the diffusing species (e.g., pure FePO<sub>4</sub>);  $a$  is the excess energy of the species-vacancy nearest-neighbor interactions over species-species and vacancy-vacancy interactions;  $k_B$  is Boltzmann's constant; and  $T$  is the temperature. The  $a$  term gives the enthalpy density of mixing and the logarithmic term gives the entropy density of mixing.

We will not consider surface energies and will assume that the gradient penalty tensor is a constant. Then (2.5), (2.9'), (2.19), (2.18), and (2.11') may be written

$$G = \int_V \rho \left\{ g_L c + g_F (1 - c) + a c (1 - c) + k_B T [c \log c + (1 - c) \log(1 - c)] + \frac{1}{2} (\nabla c)^T \mathbf{K} (\nabla c) \right\} dV \quad (2.26a)$$

$$\mu = g_L - g_F + a(1 - 2c) + k_B T \log \left( \frac{c}{1 - c} \right) - \nabla \cdot (\mathbf{K} \nabla c) \quad (2.26b)$$

$$\mathbf{J} = -\rho c \mathbf{B} \nabla \mu = -\rho c \mathbf{B} \left\{ \left[ -2a + \frac{k_B T}{c(1 - c)} \right] \nabla c - \nabla [\nabla \cdot (\mathbf{K} \nabla c)] \right\} \quad (2.26c)$$

$$\frac{\partial c}{\partial t} = -\frac{1}{\rho} \nabla \cdot \mathbf{J} = \nabla \cdot (c \mathbf{B} \nabla \mu) \quad (2.26d)$$

with boundary conditions

$$\hat{\mathbf{n}} \cdot (\mathbf{K} \nabla c) = 0 \quad (2.26e)$$

$$\hat{\mathbf{n}} \cdot \mathbf{J} = -\rho_s R(\mathbf{x}, c, \mu) . \quad (2.26f)$$

In the boundary condition on the flux,  $\rho_s$  is the surface site density and  $R$  is the net influx of the diffusional species from the external universe. This influx is usually considered the result of some reaction, so the rate will typically depend on the local concentration and chemical potential.

### 2.5.1 Non-dimensionalized gradient penalty tensor

In order to reduce the complexity of the above equations, it is frequently useful to non-dimensionalize the parameters. This can be done in many different ways, and the “best” time- and length-scales will depend on the exact problem being studied. However, there is a very simple coordinate system which is natural for this set of equations.

In § 2.1.1, we showed that  $\mathbf{K}$  is symmetric. By standard results from linear algebra,  $\mathbf{K}$  therefore has a complete set of orthogonal eigenvectors. In other words, applying a rotation to the physical space  $\mathbb{R}^d$  will transform  $\mathbf{K}$  into a diagonal matrix.

In § 2.1.1 and § 2.3.3, we showed that  $\mathbf{K}$  must also be positive definite. Therefore all of its diagonal elements are positive [56]. Since  $\mathbf{K}$  evidently has units of energy-times-length-squared, we may write

$$\mathbf{K} = k_B T \begin{pmatrix} \lambda_1^2 & & \\ & \ddots & \\ & & \lambda_d^2 \end{pmatrix}$$

for some positive lengths  $\lambda_1, \dots, \lambda_d$  in the rotated coordinate system discussed above.

Finally, it was shown in § 2.3.2 that in one dimension,  $K$  divided by a typical energy gives the square of the characteristic width of interphase boundaries. If we assume that  $k_B T$  is a typical energy scale in our problem, then in fact  $\lambda_i$  must be a characteristic interphase width in the  $i$ -direction. It is therefore natural to scale lengths in the  $i$ -direction by  $\lambda_i$ .

After rotating the axes, rescaling the lengths by  $\lambda_i$ , and rescaling energies by  $k_B T$ , we are left with a non-dimensional gradient penalty tensor which is just equal to the identity matrix. In particular, the diffusional chemical potential is simply

$$\tilde{\mu} = \tilde{g}_L - \tilde{g}_F + \tilde{a}(1 - 2c) + \log\left(\frac{c}{1 - c}\right) - \tilde{\nabla}^2 c$$

where tildes denote non-dimensionalized quantities.

### 2.5.2 Intercalant and substrate chemical potentials

As in our LiFePO<sub>4</sub>/FePO<sub>4</sub> example above, it is frequently the case that vacancies and occupied sites are distinct, well-defined chemical species. It is then reasonable to split  $G$  into two partial Gibbs free energies, one for each individual species. These would then be the chemical potentials needed, for example, to model reaction rates.

Let  $n_L$  be the concentration (in molecules per unit volume) of the diffusing species, and similarly define the concentration  $n_F$  of the vacancies. Then in terms of the variables we have been using,

$$\rho = n_L + n_F \quad \text{and} \quad c = \frac{n_L}{n_L + n_F} .$$

The free energy is then

$$G = \int_V \left\{ g_{\text{hom}}(n_L, n_F) + \frac{1}{2}(n_L + n_F) \left[ \boldsymbol{\nabla} \left( \frac{n_L}{n_L + n_F} \right) \right]^T \cdot \mathbf{K} \cdot \left[ \boldsymbol{\nabla} \left( \frac{n_L}{n_L + n_F} \right) \right] \right\} dV$$

and the chemical potentials of  $L$  and  $F$ — $\mu_L$  and  $\mu_F$ —are given by the variational derivatives of  $G$  with respect to  $n_L$  and  $n_F$ .

The calculations above are straightforward but tedious—especially if the results are to be translated back to the original variables  $c$  and  $\rho$ . Identities such as the following are helpful:

$$\begin{aligned} \frac{\partial}{\partial n_L} f(c, \rho) &= \left( \frac{1-c}{\rho} \right) \frac{\partial f}{\partial c} + \frac{\partial f}{\partial \rho} \quad \text{for any function } f, \\ \frac{\partial}{\partial n_F} f(c, \rho) &= \left( -\frac{c}{\rho} \right) \frac{\partial f}{\partial c} + \frac{\partial f}{\partial \rho} \quad \text{for any function } f, \\ \boldsymbol{\nabla} c &= \frac{1-c}{\rho} \boldsymbol{\nabla} n_L - \frac{c}{\rho} \boldsymbol{\nabla} n_F, \\ \frac{\partial}{\partial n_L} (\boldsymbol{\nabla} c) &= -\frac{1}{\rho} \boldsymbol{\nabla} c - \frac{1-c}{\rho^2} \boldsymbol{\nabla} \rho, \\ \frac{\partial}{\partial n_F} (\boldsymbol{\nabla} c) &= -\frac{1}{\rho} \boldsymbol{\nabla} c + \frac{c}{\rho^2} \boldsymbol{\nabla} \rho. \end{aligned}$$

The results are

$$\mu_L = g_L + a(1-c)^2 + k_B T \log(c) + \frac{1}{2} (\boldsymbol{\nabla} c)^T \mathbf{K} (\boldsymbol{\nabla} c) - (1-c) \boldsymbol{\nabla} \cdot (\mathbf{K} \boldsymbol{\nabla} c) \quad (2.27)$$

$$\mu_F = g_F + ac^2 + k_B T \log(1-c) + \frac{1}{2} (\boldsymbol{\nabla} c)^T \mathbf{K} (\boldsymbol{\nabla} c) + c \boldsymbol{\nabla} \cdot (\mathbf{K} \boldsymbol{\nabla} c) \quad (2.28)$$

There are two thermodynamic identities that are satisfied by these quantities. First, note that  $\mu_L - \mu_F = \mu$ ; this is as expected since the diffusional chemical potential is the energy required to replace one vacancy with a single diffusing molecule. Second,  $n_L \mu_L + n_F \mu_F = g$ , which in classical thermodynamics follows from extensivity assumptions and allows one to prove the Gibbs-Duhem relation [41].

# Chapter 3

## Reaction Rates

The thermodynamics of chemical reactions are reasonably simple, and the underlying principles date back to Gibbs. The *kinetics* of chemical reactions, on the other hand, can be extremely complicated, and even detailed, quantum-mechanical simulations frequently make predictions which do not match experiments. To make matters worse, many introductory textbooks state simplified rate laws without providing an underlying model.

The earliest theoretical work on reaction kinetics which is still generally accepted today was done by van't Hoff in 1884 [98] (who rediscovered ideas proposed earlier by Guldberg and Waage) and Arrhenius in 1889 [7]. In the latter, rates laws for reactions in aqueous solutions are written as products of the concentrations of the reactants, and it is argued that the constant must be of the form  $Ae^{-q/k_B T}$  for some “activation” heat  $q$ . Though no indication was given as to how  $q$  or  $A$  could be predicted, experiments have consistently validated that the temperature dependence of most chemical reactions is of this **Arrhenius form**.

These problems were first solved by **transition-state theory** in nearly-simultaneous papers by Eyring [39] and Evans and Polanyi [37] in 1935. This theory is based on modeling the reaction pathway as a curve through an energy landscape. The activation energy above is then explicitly quantified as the difference between the energy minimum occupied by the reactants and the energy of the saddle point over which the reaction pathway must traverse on its way to the products. In addition, the prefactor  $A$  is computed in terms of quantum statistical mechanics.

In this Chapter, we provide a brief, elementary account of transition state theory. This should be sufficient at least to motivate the rate laws employed throughout this thesis, and to make it clear why a generalized Butler-Volmer equation is appropriate for electrode kinetics in a phase-separating battery system.

In the spirit of Chapter 5, a better approach for us might be to use the theory of reaction rates developed by Kramers in 1940 [62] based on Brownian motion over an energy barrier. In addition to providing corrections to the predicted pre-exponential factor from transition-state theory, Kramers’ theory would allow us to explicitly model the stochastic effects of thermal noise on the reaction rates. For the sake of time and simplicity, however, we have omitted such a treatment.

## 3.1 Thermodynamics

For any chemical species  $S$ , we denote the concentration of  $S$  (in molecules of  $S$  per unit volume) by  $[S]$ . We may then define a **standard state**  $\Theta_S$  for  $S$  at some fixed temperature and pressure, with uniform concentrations of all species, and in particular with some fixed concentration  $[S]^\Theta$  of  $S$ . Note that different species may have different standard states.

In its standard state,  $S$  will have some well-defined chemical potential  $\mu_S^\Theta$ . In general, the instantaneous chemical potential of  $S$  will differ from its standard value, and we define the **activity**  $a_S$  of  $S$  by

$$\mu_S - \mu_S^\Theta = k_B T \log a_S , \quad (3.1)$$

where  $k_B$  is Boltzmann's constant and  $T$  is the temperature.

Now consider the reversible reaction



The Gibbs free energy change resulting from a single, net forward reaction at constant temperature and pressure is [41]

$$\Delta G = \sum_{j=1}^n d_j \mu_{P_j} - \sum_{i=1}^m c_i \mu_{R_i} .$$

Using (3.1), we may rewrite this expression as

$$\Delta G = \Delta G^\Theta + k_B T \frac{\prod_{j=1}^n a_{P_j}^{d_j}}{\prod_{i=1}^m a_{R_i}^{c_i}} ,$$

where we have defined the **standard Gibbs free energy change**

$$\Delta G^\Theta \equiv \sum_{j=1}^n d_j \mu_{P_j}^\Theta - \sum_{i=1}^m c_i \mu_{R_i}^\Theta .$$

If the system in which our reaction is taking place is at equilibrium, then we must have  $\Delta G = 0$  (since the system must be at a local free energy minimum). If we define the constant  $K_{\text{eq}}$  by

$$K_{\text{eq}} \equiv e^{-\Delta G^\Theta / k_B T} , \quad (3.3)$$

then the equilibrium condition  $\Delta G = 0$  is equivalent to

$$K_{\text{eq}} = \frac{\prod_{j=1}^n a_{P_j}^{d_j}}{\prod_{i=1}^m a_{R_i}^{c_i}} , \quad (3.4)$$

where it must be emphasized that these are all *equilibrium* activities. Equation 3.4 is a statement of the **equilibrium Law of Mass Action**, i.e. that the quotient of the equilibrium

activities is a function only of temperature. We therefore call  $K_{\text{eq}}$  the **equilibrium constant** for the reaction (3.2), though it must be kept in mind that it depends on our arbitrary definitions of the standard states.

If any of our species are electrically charged, then each  $\mu_S$  must be reinterpreted as an *electrochemical* potential, necessitating a bit more bookkeeping. We will define all of our standard states to be at 0 electrical potential, and we leave all activities unchanged. Thus, if  $S$  has charge  $z_S e$  (where  $e \approx 1.602 \times 10^{-19}$  C is the charge on a proton) and it feels the (mean-field) electrical potential  $\phi_S$ , then (3.1) becomes

$$\mu_S = \mu_S^\Theta + z_S e \phi_S + k_B T \log a_S . \quad (3.1')$$

It is frequently the case that the reaction occurs across a phase boundary around which there is a very sharp change in electrical potential. We designate one phase  $\pi_1$  and the other  $\pi_2$ ; assume the phases are at uniform electrical potentials  $\phi_1$  and  $\phi_2$ , respectively; and assume that every reactant and product feels one of these two (mean-field) electrical potentials. Denote by  $q$  the *net* charge transfer from  $\pi_1$  to  $\pi_2$  during one occurrence of the *forward* reaction from (3.2), and define  $\Delta\phi \equiv \phi_2 - \phi_1$ . Then the equilibrium Law of Mass Action becomes

$$\frac{\prod_{j=1}^n a_{P_j}^{d_j}}{\prod_{i=1}^m a_{R_i}^{c_i}} = e^{-\Delta G^\Theta / k_B T} e^{-q\Delta\phi / k_B T} . \quad (3.4')$$

As a “theorem”, the equilibrium Law of Mass Action is almost content free, depending as it does on so many undefined concepts. It is only useful in conjunction with a model for the free energy of the system which allows us to compute the activities. For instance, an **ideal solution** is one in which the activity of species  $S$  equals its mole fraction  $x_S$  in its particular phase [84] (this only strictly holds for uniform systems of non-interacting particles). In this case, the equilibrium constant may be written

$$K_{\text{eq}} = C \frac{[R_1]^{c_1} \dots [R_m]^{c_m}}{[P_1]^{d_1} \dots [P_n]^{d_n}} ,$$

where the constant  $C$  is just a product of numbers of molecules in different phases and volumes of different phases. This is often how the equilibrium Law of Mass Action is written, though this expression is only valid for ideal solutions in equilibrium.

## 3.2 Elementary Reactions

Define the (for now assumed to be unidirectional) reaction



to be **elementary** if the reactants combine together in a single, discrete chemical event. It is obviously unlikely that more than two reactants can participate in a single elementary reaction, and it can be argued [71] that an elementary reaction with only one reactant is

impossible, but we will retain the form above for generality. Note that most reactions are not, as written, elementary; however, if such a reaction occurs, it must be through some sequence of elementary steps.

Define the **extent** of the reaction  $\xi(t)$  to be the net number of times the reaction has proceeded in the forward direction by time  $t$ , and define the instantaneous **reaction rate**  $r \equiv d\xi/dt$ . If the species  $R_i$  is not one of the products of the above reaction, it is not involved in any other reactions, the volume  $V$  of the phase containing  $R_i$  remains constant, and the number  $N$  of molecules in the phase containing  $R_i$  remains constant, then

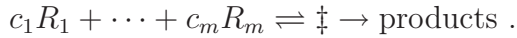
$$\frac{d[R_i]}{dt} = -\frac{c_i}{V}r \quad \text{and} \quad \frac{dx_{R_i}}{dt} = -\frac{c_i}{N}r .$$

We now wish to find a model for the reaction which will yield a **rate law**, i.e. an expression for  $r$ . For now, we ignore the possibility of a reverse reaction, so in this section  $r$  will refer only to the forward rate.

Transition state theory [71, 5] hypothesizes that:

- the reactants that go on to form the products do so only after passing through a well-defined, short-lived **activated complex**, denoted  $\ddagger$ ; and
- the reactants are in quasi-equilibrium with  $\ddagger$ .

We are therefore really studying the two-step process



The rate of the reaction (3.5) is then

$$r = \nu_{\ddagger} N_{\ddagger}$$

where  $N_{\ddagger}$  is the number of activated complexes in the system and  $\nu_{\ddagger}$  is the inverse of the average time required for an activated complex to decay into the products. We can obviously rewrite this as

$$r = \nu_{\ddagger} N x_{\ddagger}$$

where  $x_{\ddagger}$  is the mole fraction of the activated complex in its phase and  $N$  is the total number of molecules in this phase.

The frequency factor  $\nu_{\ddagger}$  can be estimated using statistical mechanics. In the simplest model in which decay involves only translation of the activated complex across a potential energy peak, the result is  $\nu_{\ddagger} = k_B T/h$ , where  $h$  is Planck's constant. This is the most typical value used. However, it is sometimes multiplied by a **transmission coefficient**  $\kappa$  to account for complexes which decay back into reactants, as well as for quantum tunneling of reactants without enough energy to overcome the classical energy barrier. Finally, there are ab initio methods for accurately estimating this term, but they are too system-specific to be of general use.

We can easily compute  $x_{\ddagger}$  from the assumptions above. Since the activated complex decays very quickly, we assume that it is extremely diluted, and thus that it behaves ideally (in the sense of §3.1):  $a_{\ddagger} = x_{\ddagger}$ . Because  $\ddagger$  is at equilibrium with the reactants, we may use the equilibrium Law of Mass Action (3.4) to get another expression for the activity:

$$a_{\ddagger} = K_{\text{eq}}^{\ddagger} \prod_{i=1}^m a_{R_i}^{c_i}$$

where  $K_{\text{eq}}^{\ddagger}$  is the equilibrium constant for the reaction between the reactants and the activated complex. Finally, we may use (3.3) to write

$$K_{\text{eq}}^{\ddagger} = e^{-\Delta^{\ddagger}G^{\Theta}/k_B T},$$

where  $\Delta^{\ddagger}G^{\Theta}$  is the standard free energy change of activation. Putting all of this together yields

$$\begin{aligned} r &= k \prod_{i=1}^m a_{R_i}^{c_i} \quad \text{where} \\ k &= A e^{-\Delta^{\ddagger}G^{\Theta}/k_B T} \quad \text{and frequently} \\ A &= \frac{k_B T}{h} N. \end{aligned} \tag{3.6}$$

The factor  $k$  is called the **rate constant**, and we have shown that in this model it is only a function of the standard states of the reactants and the activated complex. For obvious reasons,  $A$  is called the **pre-exponential factor**; it is usually taken to be a constant which is almost entirely independent of the system. Equation 3.6 is known as the **Eyring-Polanyi equation**.

In terms of chemical potentials, the reaction rate may be written

$$r = A \exp \left( \sum_{i=1}^m c_i \mu_{R_i} - \mu_{\ddagger}^{\Theta} \right).$$

Note that it only depends on the *standard* chemical potential of the activated complex, and is completely independent of the energies of the products.

To include charge transfer effects, we need only add the potential difference term from (3.4') to the  $K_{\text{eq}}^{\ddagger}$  used above. However, in this case we generally assume that, while the reactants and products are in one of the bulk phases  $\pi_1$  or  $\pi_2$ , the activated complex is very close to the interface between the two phases. Thus it feels an intermediate (mean-field)

electric field which we denote by  $\phi_1 + \beta\Delta\phi$  for some  $\beta \in [0, 1]$ . Then (3.6) becomes

$$\begin{aligned} r &= k \prod_{i=1}^m a_{R_i}^{c_i} \quad \text{where} \\ k &= Ae^{-\Delta^\ddagger G^\Theta/k_B T} e^{-q\beta\Delta\phi/k_B T} \quad \text{and frequently} \\ A &= \frac{k_B T}{h} N, \end{aligned} \tag{3.6'}$$

where, again, we have used  $q$  to denote the net charge transfer from  $\pi_1$  to  $\pi_2$  during one occurrence of reaction (3.5).

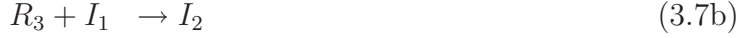
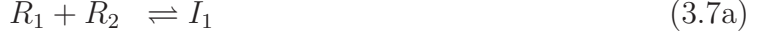
This description of the charge transfer effect differs from standard treatments [77, 11, 9], but is a bit more rigorous and easy to understand. The fraction  $\beta$  is characteristic of the reaction, and is called the **symmetry factor**. It has been found experimentally to be close to 1/2 for many different reactions, and is often taken to equal 1/2 for analytical work. Finally, note that an elementary reaction can probably involve at most one charge transfer, and in typical applications that charge is an electron.

### 3.3 Multi-Step Reactions

As mentioned above, most reactions are not elementary, but rather occur through several elementary steps which may be taking place in serial or in parallel. In principle, each step can be described by a rate law as in §3.2, and the resulting coupled ODEs may be solved to find the individual rates of creation or depletion. This program has several shortcomings, though. First, there are frequently intermediate species created during early steps and consumed during later steps, and we would require an activity model for each one. Second, the equations would be highly coupled and non-linear (especially when non-ideal solution models are needed), making them difficult to solve. Third, there are many parameters (in particular, the free energies of the intermediate activated complexes) which are difficult to estimate and almost impossible to measure in isolation in a real system.

For these and other reasons, we wish to formulate a simpler model for the rate of a multi-step reaction. One way to do this is by making the same quasi-equilibrium assumption as was employed in §3.2. In particular, we assume that all but one elementary step is so fast that its reactants and products are in equilibrium, and that the remaining step (the so-called **rate-determining step**, or rds) is sufficiently slow to control the overall rate of the reaction.

We illustrate the general procedure with the following three-step system:



where  $I_1$  and  $I_2$  are intermediates that do not interest us,  $\{R_1, R_2, R_3, R_4\}$  is the set of reactants, and  $P$  is the product. We will assume that (3.7b) is the rate-determining step,

and that (3.7a) and (3.7c) are fast enough to remain equilibrated. Then using the transition state model (Equation 3.6'), the overall rate of the reaction is

$$r = Ae^{-\Delta^{\ddagger}G_2^{\Theta}/k_B T} e^{-q_2\beta_2\Delta\phi/k_B T} a_{R_3} a_{I_1},$$

where  $\Delta^{\ddagger}G_2^{\Theta}$  is the standard Gibbs free energy of activation of the rds,  $q_2$  is the charge transferred across the interface during the rds, and  $\beta_2$  is the symmetry factor of the rds. We do not know the activity for the intermediate species  $I_1$ . However, since we are assuming that (3.7a) is at equilibrium, we may use the equilibrium Law of Mass Action (3.4') to write

$$a_{I_1} = e^{-\Delta G_1^{\Theta}/k_B T} e^{-q_1\Delta\phi/k_B T} a_{R_1} a_{R_2},$$

where  $\Delta G_1^{\Theta}$  is the standard Gibbs free energy change for (3.7a) and  $q_1$  is the charge transferred across the interface during (3.7a). We can combine these two expressions to get

$$r = Ae^{-(\Delta G_1^{\Theta} + \Delta^{\ddagger}G_2^{\Theta})/k_B T} e^{-(q_1 + q_2\beta_2)\Delta\phi/k_B T} a_{R_1} a_{R_2} a_{R_3}.$$

Note that nothing that happens after the rds enters into the rate expression, and in particular that the rate is independent of the activity of the reactant  $R_4$ . Also note that only the charge transferred during the rds is multiplied by a corresponding symmetry factor.

This result can easily be generalized. First, it appears that we have restricted the analysis to three elementary steps. However, all we have assumed about (3.7a) and (3.7c) is that they each instantly equilibrate in response to changes driven by the rds. They need not be elementary steps at all, nor will adding more of them (or removing either of them, obviously) change the fact that the overall rate is exactly the forward rate of the rds. Further, as long as all intermediates created before the rds are consumed by the rds, we can still cancel the intermediates' activities from the rate law by using the product of the equilibrium constants of the pre-rds reactions. Finally, we can even account for some of the product species being generated before the rds. However, our use of the pre-rds equilibrium constants means that the forward rate law for our overall reaction will include some of the products' activities.

If all of our assumptions are met, we get the following rate law:

$$r = Ae^{-\Delta^{\ddagger}G_{\text{cum}}^{\Theta}/k_B T} e^{-\alpha e\Delta\phi/k_B T} \prod_{i=1}^m a_{R_i}^{c'_i} / \prod_{j=1}^n a_{P_j}^{d'_j}. \quad (3.8)$$

The activity exponents are primed to indicate that they are not the same as the stoichiometric coefficients for the overall reaction. Instead,  $c'_i$  is the net number of molecules of  $R_i$  consumed up to and including the rds, and  $d'_j$  is the net number of molecules of  $P_j$  produced by this point. Any of these coefficients can be 0 if the corresponding species has no *net* involvement with the creation of the activated complex during the rds. We have defined

$$\Delta^{\ddagger}G_{\text{cum}}^{\Theta} \equiv \Delta G_1^{\Theta} + \Delta G_2^{\Theta} + \cdots + \Delta G_{\text{rds}-1}^{\Theta} + \Delta^{\ddagger}G_{\text{rds}}^{\Theta}$$

to be the sum of the standard Gibbs free energy differences for the pre-rds reactions, plus the

standard Gibbs free energy of activation for the rds. Since there are no *net* intermediates, this is equivalent to

$$\Delta^\ddagger G_{\text{cum}}^\Theta = \mu_{\ddagger}^\Theta + \sum_{j=1}^n d'_j \mu_{P_j}^\Theta - \sum_{i=1}^m c'_i \mu_{R_i}^\Theta ,$$

where again we must use the primed coefficients. Finally, we have defined the **transfer coefficient**

$$\alpha \equiv \frac{1}{e} (q_1 + q_2 + \cdots + q_{\text{rds}-1} + \beta_{\text{rds}} q_{\text{rds}})$$

to be the net number of protons (electrons are counted as negative protons) transferred across the phase boundary before the rds, plus the usual symmetry factor for the rds.

The inclusion of product activities in a forward rate law may seem odd. In an elementary reaction, increasing the concentration of a product decreases the *overall* reaction rate only by increasing the *reverse* rate. In the general case, though, one of the product species might be generated in a pre-rds reaction along with an intermediate needed by the rds. Then increasing the concentration of the product will decrease the concentration of the intermediate, thus slowing the *forward* rate of the rds.

Note that the transfer coefficient for a multi-step reaction is very different from the symmetry factor for an elementary reaction. It is not constrained to the interval  $[0, 1]$ , and need not even be positive. However, it is the transfer coefficient rather than the symmetry factor which can be measured experimentally.

## 3.4 Reverse Reactions

We have so far only considered the forward rates of our reactions. Many texts use the transition state model to simultaneously predict the forward and reverse rates for an elementary reaction. This seems natural, especially since we would expect both directions to go through the same activated state. However, the derivation of the rate law assumes that the reactants are in equilibrium with the activated complex. If we apply this same model to the reverse reaction, then we must assume that the products are also in equilibrium with the activated complex. But then by the Zeroth Law of Thermodynamics [41], the reactants must be in equilibrium with the products. We would thus only be predicting the equilibrium rate laws, and we would have no way to extrapolate to any out-of-equilibrium setting. One fix is to posit the existence of two activated complexes—one in equilibrium with the reactants and the other in equilibrium with the products—but then we would need to know the energy difference between these two complexes.

Regardless of the mechanism, we will assume that a rate law of the form (3.6') exists—

even out of equilibrium—for the forward and backward directions:

$$r_f = k_f \prod_{i=1}^m a_{R_i}^{c_i} \quad \text{where}$$

$$k_f = A_f e^{-\Delta^\ddagger G_f^\Theta / k_B T} e^{-q_f \beta_f \Delta\phi / k_B T} \quad ; \text{ and}$$

$$r_b = k_b \prod_{i=1}^n a_{P_i}^{d_i} \quad \text{where}$$

$$k_b = A_b e^{-\Delta^\ddagger G_b^\Theta / k_B T} e^{-q_b \beta_b \Delta\phi / k_B T} .$$

We must now relate the parameters for the reverse reaction to those for the forward reaction.

At equilibrium, obviously  $r_f = r_b$ . Combining this with the equilibrium Law of Mass Action (3.4) yields

$$\frac{k_f}{k_b} = K_{\text{eq}} . \quad (3.9)$$

This is called the **kinetic Law of Mass Action**, and is sometimes described as being equivalent to the equilibrium Law of Mass Action as we have defined it. However, the kinetic law is *not* fundamental, but is rather a trivial consequence of the forms of the rate laws that we have *assumed* above. Expanding the kinetic law using (3.4'), we see that the following must hold:

$$\frac{A_f}{A_b} e^{-(\Delta^\ddagger G_f^\Theta - \Delta^\ddagger G_b^\Theta) / k_B T} e^{-(q_f \beta_f - q_b \beta_b) \Delta\phi / k_B T} = e^{-\Delta G^\Theta / k_B T} e^{-q \Delta\phi / k_B T} .$$

Note that the  $q$  used on the right side of the above equation was defined to be the same as  $q_f$ . By conservation of charge, we must have  $q_b = -q_f = -q$ . But then if the above is to hold for any value of  $\Delta\phi$ , we must have  $\beta_f + \beta_b = 1$  (assuming only that the pre-exponential factors are independent of  $\Delta\phi$ ). This can be understood in the transition state model as implying that the activated complexes in both directions share a common location along the potential drop. We follow common convention and let  $\beta = \beta_f$  be the symmetry factor for the reaction, and write the potential term in  $k_b$  as  $+q(1 - \beta)$ .

Factoring out the potential terms leaves us with

$$\frac{A_f}{A_b} e^{-(\Delta^\ddagger G_f^\Theta - \Delta^\ddagger G_b^\Theta) / k_B T} = e^{-\Delta G^\Theta / k_B T} .$$

To make more progress, we must make an additional assumption: either that  $A_f = A_b$ , which is supported by the simple transition models described in §3.2; or that the forward and backward reactions go through activated complexes with the same standard Gibbs free energy, which is reasonable since one would think that the two activated complexes must be identical. Either assumption in combination with the above equality implies the other, and that  $\Delta^\ddagger G_f^\Theta - \Delta^\ddagger G_b^\Theta = \Delta G^\Theta$ . Note that we could not have derived this just by making a mathematical argument about the temperature dependence of the various factors in

the equation above since there is an additional temperature dependence hidden in the free energies.

Putting all of these assumptions and conclusions together yields the final form for the rate laws of a bi-elementary, reversible reaction:

$$r_f = k_f \prod_{i=1}^m a_{R_i}^{c_i} \quad \text{where} \quad (3.10a)$$

$$k_f = A e^{-\Delta^\ddagger G_f^\Theta / k_B T} e^{-q\beta\Delta\phi / k_B T}; \quad (3.10b)$$

$$r_b = k_b \prod_{i=1}^n a_{P_i}^{d_i} \quad \text{where} \quad (3.10c)$$

$$k_b = A e^{-\Delta^\ddagger G_b^\Theta / k_B T} e^{+q(1-\beta)\Delta\phi / k_B T}; \quad (3.10d)$$

$$\Delta G^\Theta = \Delta^\ddagger G_f^\Theta - \Delta^\ddagger G_b^\Theta; \quad \text{and frequently} \quad (3.10e)$$

$$A = \frac{k_B T}{h} N. \quad (3.10f)$$

By expanding the activities using (3.1'), we see that the following holds, in or out of equilibrium:

$$\frac{r_f}{r_b} = \exp \left( \frac{1}{k_B T} \sum_{i=1}^m c_i \mu_{R_i} - \frac{1}{k_B T} \sum_{j=1}^n d_j \mu_{P_j} \right) = e^{-\Delta G / k_B T}, \quad (3.11)$$

where the  $\mu$ 's are electrochemical potentials, and  $\Delta G$  is the free energy difference between the products and the reactants (including mean-field electrical potential differences). Note that these are all energies of the system in its *current* state, not the standard state. This is known as **de Donder's equation**. Again, this is *not* a fundamental law (at least as we have derived it), but rather a consequence of the *assumptions* made in producing the rate laws above. Also, note that the net reaction rate depends exponentially on the driving force, so the standard linear approximations in non-equilibrium thermodynamics [26] are wildly inaccurate.

Finally, note that we may use the elementary reverse rate law to derive a reverse rate law for our multi-step reaction from §3.3. Since we require slight changes in the notation, we include the forward and reverse laws here:

$$r_f = A e^{-\Delta^\ddagger G_{\text{cum},f}^\Theta / k_B T} e^{-\alpha_f e\Delta\phi / k_B T} \prod_{i=1}^m a_{R_i}^{c'_i} / \prod_{j=1}^n a_{P_j}^{d'_j} \quad (3.12a)$$

$$r_b = A e^{-\Delta^\ddagger G_{\text{cum},b}^\Theta / k_B T} e^{+\alpha_b e\Delta\phi / k_B T} \prod_{j=1}^n a_{P_j}^{(d_j - d'_j)} / \prod_{i=1}^m a_{R_i}^{(c_i - c'_i)}. \quad (3.12b)$$

The forward rate law is the same as (3.8), though we must now differentiate the *forward* transfer coefficient  $\alpha_f$  from the *reverse* transfer coefficient  $\alpha_b$ . By convention, we count protons crossing the interface in the forward direction even for the reverse reaction rate.

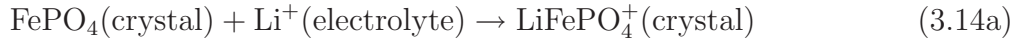
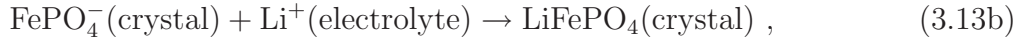
This explains the sign change in the electrical terms, and yields the relation

$$\alpha_f + \alpha_b = q/e , \quad (3.12c)$$

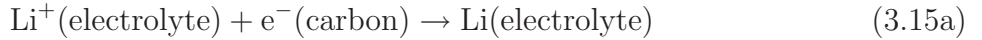
where  $q$  is the net charge transferred across the interface during a single, complete instance of the multi-step reaction in the forward direction. Finally, note that the multi-step rate laws also satisfy de Donder's equation.

### 3.5 Applications to Lithium Iron Phosphate

The intercalation reaction in  $\text{LiFePO}_4$  involves an electron transfer from carbon black and a lithium transfer from the electrolyte, so is almost certainly not elementary. The three obvious candidates for reaction pathways are



or



Pathway (3.13) seems the most plausible: the  $\text{Fe}^{3+}$  in  $\text{FePO}_4$  “wants” to get reduced, and once it does so, the lithium ion would get pulled across the boundary to reestablish charge neutrality. In contrast, it is harder to understand why the lithium would initiate the intercalation in the other two pathways. Moreover, in any pathway, the rate-determining step is almost certainly the lithium insertion since this probably must involve a significant deformation of the crystal lattice. For completion and comparison, though, we will write down the rate laws for all six possibilities.

First we must agree on conventions for the directions of the electrical potential differences. If the carbon-crystal and electrolyte-crystal potential differences were the same, then because an electron and a positively-charged lithium ion must both cross the crystal interface, we would require  $\alpha_f + \alpha_b = 0$ . The three interfaces probably have different potential drops, though, so we will approach the problem more generally. Denote the carbon phase by  $C$ , the electrolyte phase by  $E$ , and the crystal phase by  $F$  (which stands for Fe). We use the following notational pattern for the interphase data: the difference between the electrical potential in the crystal and that in the electrolyte is written  $\Delta_{E \rightarrow F}\phi \equiv \phi_F - \phi_E$ , and the symmetry factor for the lithium-ion insertion across this interface is written  $\beta_{E \rightarrow F}$ .

The reaction rates for any case can be read off from (3.12). For path (3.13) with rds (3.13a), we get

$$r_{f,(3.13),(3.13a)} = Ae^{-\Delta^\ddagger G_{\text{cum},f}^\Theta / k_B T} e^{+e\beta_{C \rightarrow F}\Delta_{C \rightarrow F}\phi / k_B T} a_{\text{FePO}_4} a_{\text{e}^-}$$

$$r_{b,(3.13),(3.13a)} = Ae^{-\Delta^\ddagger G_{\text{cum},b}^\Theta / k_B T} e^{-e(1-\beta_{C \rightarrow F})\Delta_{C \rightarrow F}\phi / k_B T} e^{+e\Delta_{E \rightarrow F}\phi / k_B T} a_{\text{LiFePO}_4} / a_{\text{Li}^+} .$$

For path (3.13) with rds (3.13b), we get

$$r_{f,(3.13),(3.13b)} = Ae^{-\Delta^\ddagger G_{\text{cum},f}^\Theta / k_B T} e^{-e\beta_{E \rightarrow F}\Delta_{E \rightarrow F}\phi / k_B T} e^{+e\Delta_{C \rightarrow F}\phi / k_B T} a_{\text{FePO}_4} a_{\text{Li}^+} a_{\text{e}^-}$$

$$r_{b,(3.13),(3.13b)} = Ae^{-\Delta^\ddagger G_{\text{cum},b}^\Theta / k_B T} e^{+e(1-\beta_{E \rightarrow F})\Delta_{E \rightarrow F}\phi / k_B T} a_{\text{LiFePO}_4} .$$

For path (3.14) with rds (3.14a), we get

$$r_{f,(3.14),(3.14a)} = Ae^{-\Delta^\ddagger G_{\text{cum},f}^\Theta / k_B T} e^{-e\beta_{E \rightarrow F}\Delta_{E \rightarrow F}\phi / k_B T} a_{\text{FePO}_4} a_{\text{Li}^+}$$

$$r_{b,(3.14),(3.14a)} = Ae^{-\Delta^\ddagger G_{\text{cum},b}^\Theta / k_B T} e^{+e(1-\beta_{E \rightarrow F})\Delta_{E \rightarrow F}\phi / k_B T} e^{-e\Delta_{C \rightarrow F}\phi / k_B T} a_{\text{LiFePO}_4} / a_{\text{e}^-} .$$

For path (3.14) with rds (3.14b), we get

$$r_{f,(3.14),(3.14b)} = Ae^{-\Delta^\ddagger G_{\text{cum},f}^\Theta / k_B T} e^{+e\beta_{C \rightarrow F}\Delta_{C \rightarrow F}\phi / k_B T} e^{-e\Delta_{E \rightarrow F}\phi / k_B T} a_{\text{FePO}_4} a_{\text{Li}^+} a_{\text{e}^-}$$

$$r_{b,(3.14),(3.14b)} = Ae^{-\Delta^\ddagger G_{\text{cum},b}^\Theta / k_B T} e^{-e(1-\beta_{C \rightarrow F})\Delta_{C \rightarrow F}\phi / k_B T} a_{\text{LiFePO}_4} .$$

For path (3.15) with rds (3.15a), we get

$$r_{f,(3.15),(3.15a)} = Ae^{-\Delta^\ddagger G_{\text{cum},f}^\Theta / k_B T} e^{+e\beta_{C \rightarrow E}\Delta_{C \rightarrow E}\phi / k_B T} a_{\text{Li}^+} a_{\text{e}^-}$$

$$r_{b,(3.15),(3.15a)} = Ae^{-\Delta^\ddagger G_{\text{cum},b}^\Theta / k_B T} e^{-e(1-\beta_{C \rightarrow E})\Delta_{C \rightarrow E}\phi / k_B T} a_{\text{LiFePO}_4} / a_{\text{FePO}_4} .$$

For path (3.15) with rds (3.15b), we get

$$r_{f,(3.15),(3.15b)} = Ae^{-\Delta^\ddagger G_{\text{cum},f}^\Theta / k_B T} e^{+e\Delta_{C \rightarrow E}\phi / k_B T} a_{\text{FePO}_4} a_{\text{Li}^+} a_{\text{e}^-}$$

$$r_{b,(3.15),(3.15b)} = Ae^{-\Delta^\ddagger G_{\text{cum},b}^\Theta / k_B T} a_{\text{LiFePO}_4} .$$

The  $\Delta^\ddagger G^\Theta$  term must be interpreted differently in each case. Notice that only when the last step is the rate-determining one do we get a forward rate proportional to the product of the reactant activities and a reverse rate proportional only to the product activity. Also, note that the rate laws for path (3.15) with rds (3.15a) only contain the LiFePO<sub>4</sub> and FePO<sub>4</sub> activities as ratios of one another. As will become clear later, this is highly desirable since it would mean that we would only need the difference between the LiFePO<sub>4</sub> and FePO<sub>4</sub> chemical potentials rather than needing them both individually. Unfortunately, this is probably the least likely of the six mechanisms.

We now focus on pathway (3.13) with a fast electron transfer and slow lithium transfer.

We can expand the activities using (3.1') to get the following rate laws:

$$r_f = Ae^{(\mu_{\text{FePO}_4} + \mu_{\text{Li}^+} + \mu_{\text{e}^-} - \mu_{\ddagger}^{\Theta})/k_B T} e^{(1 - \beta_{E \rightarrow F}) \Delta_{E \rightarrow F} \phi / k_B T},$$

$$r_b = Ae^{(\mu_{\text{LiFePO}_4} - \mu_{\ddagger}^{\Theta})/k_B T} e^{(1 - \beta_{E \rightarrow F}) \Delta_{E \rightarrow F} \phi / k_B T}.$$

The fact that the electrical potential factors are identical may appear odd, but this is the result of more electrical terms being hidden in the electrochemical potentials  $\mu_{\text{Li}^+}$  and  $\mu_{\text{e}^-}$ .

Now we must find the chemical potentials. The lithium chemical potential requires an energy model for the electrolyte and a solution to the transport equations between the anode and the cathode. However, we might be able to consider it a constant during the intercalation of a single crystal. Similarly, the electrochemical potential of the electrons requires knowledge of the material properties of carbon black, but might also be considered a constant for our purposes.

The only remaining question, then, is how to compute  $\mu_{\text{FePO}_4}$  and  $\mu_{\text{LiFePO}_4}$ . In the variational setting, we may use the expressions (2.27) and (2.28). We non-dimensionalize electrical potentials by  $k_B T/e$ , energies by  $k_B T$ , and time by

$$\tau \equiv \frac{\exp(\mu_{\ddagger}^{\Theta})}{A}.$$

Note that  $\mu_{\ddagger}^{\Theta}$  is a *standard* chemical potential, so is a constant. It certainly belongs in the time unit since it has the same, exponential effect on both the forward and reverse reactions. Finally, if we non-dimensionalize lengths using the gradient penalty tensor (as in § 2.5.1), our rate laws may be written

$$\begin{aligned} \tilde{r}_f &= \exp \left[ (1 - \beta_{E \rightarrow F}) \Delta_{E \rightarrow F} \tilde{\phi} \right] \\ &\quad \cdot \exp \left[ \tilde{\mu}_{\text{Li}^+} + \tilde{\mu}_{\text{e}^-} + \tilde{g}_F + \tilde{a}c^2 + \log(1 - c) + \frac{1}{2} \|\tilde{\nabla} c\|^2 + c \nabla^2 c \right] \end{aligned} \tag{3.16}$$

$$\begin{aligned} \tilde{r}_b &= \exp \left[ (1 - \beta_{E \rightarrow F}) \Delta_{E \rightarrow F} \tilde{\phi} \right] \\ &\quad \cdot \exp \left[ \tilde{g}_L + \tilde{a}(1 - c)^2 + \log c + \frac{1}{2} \|\tilde{\nabla} c\|^2 - (1 - c) \nabla^2 c \right] \end{aligned} \tag{3.17}$$

where tildes denote non-dimensionalized quantities.

This is a very unusual reaction rate law. If we only had the constant and logarithmic terms in the second exponentials, this would be of the **Butler-Volmer** form, and the rate would mostly be driven by the interfacial potential differences. The quadratic terms (with coefficient  $\tilde{a}$ ) in the exponentials are just the result of using concentrated solution theory rather than dilute solution theory, but are still rarely included in reaction rates in textbooks. Finally, the Laplacian terms in the exponential come from explicit modeling of the phase separation in the bulk; their presence in the exponents of reaction rate laws appears to have been unprecedented until recent work on LiFePO<sub>4</sub> [90].

THIS PAGE INTENTIONALLY LEFT BLANK

# Chapter 4

## Finite Volume Methods Applied to the Cahn-Hilliard Equation

There are many standard numerical techniques for solving partial differential equations. However, they are not all suitable for every problem. For example, the Finite Difference Method (FDM) is the simplest general scheme: function values are stored on a grid, and all derivatives are approximated by local linear functions of these values. However, these are typically low-order approximations, and when applied to conservation equations (like the Cahn-Hilliard equation), global conservation is not guaranteed.

In contrast to finite difference methods, spectral methods have extremely high orders of accuracy. In a finite domain with non-trivial boundary conditions (such as a flux condition involving reaction rates), we cannot assume periodicity, and so cannot use Fourier series. Chebyshev polynomials may be used instead, which might allow for enough accuracy to overcome the lack of any conservation guarantees. However, in phase-separating systems, there is a sharp interphase boundary near which any spectral method will still be susceptible to the Gibbs phenomenon [95]. Overcoming this difficulty requires using more basis elements, which quickly becomes computationally expensive.

For these reasons, we have chosen to use the Finite Volume Method (FVM), which we now describe.

### 4.1 The Finite Volume Method

Suppose we have some scalar field  $c(\mathbf{x}, t)$  which is locally conserved. If we can define flux vectors  $\mathbf{J}(\mathbf{x}, t)$  for  $c$ , then we can usually derive a PDE for local conservation:

$$\frac{\partial c}{\partial t} + \nabla \cdot \mathbf{J} = 0 . \quad (4.1)$$

This is done by integrating  $c$  over a control volume  $CV$ , and asserting that the only way this total amount of  $c$  can change is by fluxes across the boundary of  $CV$ . We thus arrive at the

integral equation

$$\frac{d}{dt} \int_{CV} c(\mathbf{x}, t) dV + \int_{\partial(CV)} \hat{\mathbf{n}} \cdot \mathbf{J}(\mathbf{x}, t) dA = 0 . \quad (4.2)$$

The PDE is then derived by applying Stokes' theorem to the surface integral and taking the limit as  $CV$  shrinks to 0.

The cell-centered finite volume method (FVM) is a general numerical scheme for solving conservative PDEs of the form (4.1) by taking (4.2) as the fundamental equation [66]. The geometry of the problem is split into many small control volumes. For each cell  $C_i$ , the average value of  $c$ ,

$$\bar{c}_i(t) \equiv \frac{1}{\text{Vol}(C_i)} \int_{C_i} c(\mathbf{x}, t) dV , \quad (4.3)$$

is stored (as opposed to a point value of  $c$  as in the finite difference method). Then (4.2) can be written exactly as

$$\frac{d\bar{c}_i}{dt} = -\frac{1}{\text{Vol}(C_i)} \sum_{E_{i,j} \in \partial C_i} J_{i,j} \quad (4.4)$$

where  $J_{i,j}(t)$  is the total normal flux across one edge  $E_{i,j}$  of the boundary of  $C_i$ . In the *semi-discrete* finite volume method, each  $J_{i,j}(t)$  is approximated in terms of the  $\bar{c}_i(t)$ , and then (4.4) is solved using the method of lines, i.e. by integrating this set of ODEs in time.

The finite volume method has several advantages over other numerical methods. First, it is very easy and natural to incorporate boundary conditions for the flux, even for higher-order problems. Second, the global conservation of  $c$  is numerically guaranteed. Indeed, since for each edge only a single normal flux is computed, the flux from one cell into one of its neighbors is exactly the negative of the flux into the neighbor from the first cell. Thus, the only way that  $\sum_i \bar{c}_i \text{Vol}(C_i)$  can change is by fluxes from the system boundaries or numerical errors in the time-stepping.

A disadvantage of the finite volume method is that finding approximation formulas for functions and their derivatives is more difficult than for finite difference methods [54]. The reason is that the stored values  $\bar{c}_i$  are cell averages and the fluxes  $J_{i,j}$  are boundary totals; neither is a simple point value. Since the cell average is a second-order-accurate approximation for the value of  $c$  at the center of the cell (regardless of its shape or size), standard second-order finite difference formulas can often be used. However, care must still be exercised near boundaries or for higher-order methods.

#### 4.1.1 Accuracy

Suppose we wish to compute  $d\bar{c}_i/dt$  with a certain level of spatial accuracy. It might appear from (4.4) that we would need to compute the  $J_{i,j}$  with *more* accuracy since we must divide by  $\text{Vol}(C_i)$ . For example, in one dimension the formula becomes  $d\bar{c}_i/dt = (J_{i,2} - J_{i,1})/\Delta x$ , so if the  $J_{i,j}$  are  $O((\Delta x)^n)$  accurate, the division by  $\Delta x$  appears to leave  $d\bar{c}_i/dt$  with only  $O((\Delta x)^{n-1})$  accuracy.

For any particular FVM problem, this obviously must be checked. However,  $d\bar{c}_i/dt$  will

tend to have the same accuracy as the fluxes despite the division by  $\text{Vol}(C_i)$ . To see this, we again specialize to one dimension. If the  $J_{i,j}$  have order  $n$  accuracy, their error will be of the form  $e_j(\Delta x)^n$ , where  $e_j$  is some combination of values of  $c$  and its derivatives at the  $j^{\text{th}}$  boundary point. Thus the computed  $d\bar{c}_i/dt$  will have an error of the form  $(e_2 - e_1)(\Delta x)^{n-1}$ . However,  $e_1$  and  $e_2$  will usually be of the same functional form, just evaluated at points that are  $\Delta x$  apart. Therefore  $e_2 - e_1$  will tend to be an  $O(\Delta x)$  quantity, and the computed derivative will indeed have  $O((\Delta x)^n)$  accuracy.

This property will tend to fail near the boundaries as the forms for the  $e_j$  will need to change to take boundary conditions into account. Thus, even when the boundary fluxes are all  $n^{\text{th}}$ -order accurate, the fact that the error terms are of a different form will reduce the accuracy of the time derivatives. This problem cannot be eliminated by using more accurate flux computations near the boundaries. For example, if we employ no-flux boundary conditions, then the  $J$ 's at the boundaries are *exact*. Despite this, though, it is obvious from (4.4) that the order- $n$  accuracy of the other flux components will amount to an order- $(n-1)$  accuracy for the time derivatives. In general, the order of accuracy must drop near the boundaries in finite volume methods.

#### 4.1.2 Conservation during time-stepping

In diffusion problems, it is often advantageous to employ an implicit scheme for the time integration. With such methods, the  $\bar{c}_i$  for the next time step satisfy some set of implicit equations in terms of the  $\bar{c}_i$  from the current time step. These equations are generally not solvable in closed form, especially when  $\mathbf{J}$  is a non-linear function of the  $\bar{c}_i$ ; we therefore cannot expect for them to be solved exactly in numerical code. These errors are a potential threat to the FVM guarantee that  $\sum_i \bar{c}_i \text{Vol}(C_i)$  remains constant.

Conservation can still be maintained without having to solve the implicit equations exactly. For example, constrained optimization tools may be used at every time step. However, it is frequently the case that no extra work is needed. If we analytically compute the gradients of our numerical equations as the difference of the gradients of the fluxes, and if a Newton-Raphson method is employed to solve the time-stepping equations using these gradients, then it can be shown that a sufficiently small time step will guarantee conservation by the solver.

## 4.2 One-Dimensional Geometries

In one-dimensional geometries, the control volumes are line segments. Denote the coordinates of their endpoints by  $x_0, x_1, \dots, x_N$  (so the total system length is  $L \equiv x_N - x_0$ ), the coordinates of their midpoints by  $x_{i-1/2} \equiv \frac{1}{2}(x_{i-1} + x_i)$ , and their widths by  $\Delta x_i \equiv x_i - x_{i-1}$ . The average values used by the finite volume method are given by

$$\bar{c}_i \equiv \frac{1}{\Delta x_i} \int_{x_{i-1}}^{x_i} c(x) dx \quad (4.3,1D)$$

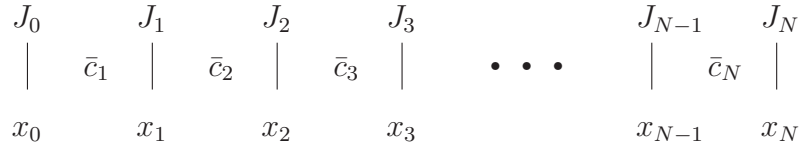


Figure 4-1: Schematic of the geometry for a one-dimensional finite volume method. The average value of  $c(x)$  between  $x_{i-1}$  and  $x_i$  is approximated by  $\bar{c}_i$ . The fluxes  $J_i$  are computed at the points  $x_i$ .

for  $i = 1, 2, \dots, N$  (see Fig. 4-1 for a schematic). An approximation  $J_i$  is computed for the flux at each point  $x_i$ , and the system of equations solved by the method of lines is then

$$\frac{d\bar{c}_i}{dt} = -\frac{1}{\Delta x_i} (J_i - J_{i-1}) . \quad (4.4,1D)$$

### 4.2.1 General formulas

To proceed, we must be able to approximate  $c(x)$  and its derivatives at various points in the system. Formulas can be derived by Taylor-expanding  $c(x)$  about the point of interest, computing  $\bar{c}_i$  for nearby  $i$  in terms of this expansion, and then taking linear combinations of these  $\bar{c}_i$  which yield the desired derivative of  $c(x)$  with some acceptable error. For reference, we include several second-order-accurate examples in the case where the control volume width is a constant denoted by  $h$  (see [54] for more general and higher-order examples).

Approximations at the midpoints of control volumes away from the system boundaries are listed in Table 4.1. Approximations at the endpoints of control volumes away from the system boundaries are listed in Table 4.2.

quantity of interest	coefficients					error
	$\bar{c}_{j-2}$	$\bar{c}_{j-1}$	$\bar{c}_j$	$\bar{c}_{j+1}$	$\bar{c}_{j+2}$	
$c(x_{j-1/2})$			1			$-\frac{1}{24}c^{(2)}(x_{j-1/2})h^2 + O(h^4)$
$c^{(1)}(x_{j-1/2})$		$-\frac{1}{2h}$		$\frac{1}{2h}$		$-\frac{5}{24}c^{(3)}(x_{j-1/2})h^2 + O(h^4)$
$c^{(2)}(x_{j-1/2})$		$\frac{1}{h^2}$	$-\frac{2}{h^2}$	$\frac{1}{h^2}$		$-\frac{1}{8}c^{(4)}(x_{j-1/2})h^2 + O(h^4)$
$c^{(3)}(x_{j-1/2})$	$-\frac{1}{2h^3}$	$\frac{2}{2h^3}$		$-\frac{2}{2h^3}$	$\frac{1}{2h^3}$	$-\frac{7}{24}c^{(5)}(x_{j-1/2})h^2 + O(h^4)$

Table 4.1: One-dimensional FVM approximations for point values and low-order derivatives at cell midpoints in the bulk. Each row gives the coefficients of the linear approximation for the quantity in the leftmost column.

quantity of interest	coefficients				error
	$\bar{c}_{j-1}$	$\bar{c}_j$	$\bar{c}_{j+1}$	$\bar{c}_{j+2}$	
$c(x_j)$		$\frac{1}{2}$	$\frac{1}{2}$		$-\frac{1}{6}c^{(2)}(x_j)h^2 + O(h^4)$
$c^{(1)}(x_j)$		$-\frac{1}{h}$	$\frac{1}{h}$		$-\frac{1}{12}c^{(3)}(x_j)h^2 + O(h^4)$
$c^{(2)}(x_j)$	$\frac{1}{2h^2}$	$-\frac{1}{2h^2}$	$-\frac{1}{2h^2}$	$\frac{1}{2h^2}$	$-\frac{1}{4}c^{(4)}(x_j)h^2 + O(h^4)$
$c^{(3)}(x_j)$	$-\frac{1}{h^3}$	$\frac{3}{h^3}$	$-\frac{3}{h^3}$	$\frac{1}{h^3}$	$-\frac{1}{6}c^{(5)}(x_j)h^2 + O(h^4)$

Table 4.2: One-dimensional FVM approximations for point values and low-order derivatives at cell endpoints in the bulk. Each row gives the coefficients of the linear approximation for the quantity in the leftmost column.

Near the system boundaries, many of these formulas cannot be applied because they involve nonexistent average values ( $\bar{c}_0$  or  $\bar{c}_{N+1}$ , for example). Less symmetric formulas are therefore required. Moreover, we frequently need to incorporate boundary conditions into our formulas, so the general equations given in [54] are not necessarily useful. Tables 4.3 and 4.4 list equations that are valid near the boundaries and which incorporate the conditions  $c'(x_0) = c'(x_N) = 0$ ; this is the one-dimensional variational boundary condition (2.11) absent any concentration-dependence in the surface energy  $\gamma$ .

### 4.2.2 The Cahn-Hilliard equation

In one dimension, we may non-dimensionalize the Cahn-Hilliard equation by using the length scale  $\lambda$  and the time scale  $\lambda^2/D$ . Then the non-dimensional equation is given by

$$\frac{\partial c}{\partial t} = -\frac{\partial J}{\partial x}$$

where the non-dimensional flux  $J$  is defined by

$$J = 2acc^{(1)} - \frac{c^{(1)}}{1-c} + cc^{(3)}$$

(see Eqs. 2.26). This is computed by using the formulas in Table 4.2 to approximate  $c$ ,  $c^{(1)}$ , and  $c^{(3)}$  (though formulas from Tables 4.3 and 4.4 are needed near the boundaries). The result is a second-order-accurate approximation for  $J$  and a symmetric, five-point stencil for the  $d\bar{c}_i/dt$ . Further, numerical tests confirm that the corresponding approximation for the time derivatives is also  $O(h^2)$  (c.f. Fig. 4-2).

quantity of interest	coefficients				error
	$\bar{c}_1$	$\bar{c}_2$	$\bar{c}_3$	$\bar{c}_4$	
$c(x_0)$	1				$-\frac{1}{6}c^{(2)}(x_0)h^2 + O(h^3)$
$c^{(1)}(x_0)$					0
$c^{(2)}(x_0)$	$\frac{-25}{11h^2}$	$\frac{32}{11h^2}$	$\frac{-7}{11h^2}$		$\frac{17}{44}c^{(4)}(x_0)h^2 + O(h^3)$
$c^{(3)}(x_0)$	$\frac{30}{5h^3}$	$\frac{-54}{5h^3}$	$\frac{30}{5h^3}$	$\frac{-6}{5h^3}$	$\frac{151}{150}c^{(5)}(x_0)h^2 + O(h^3)$
$c^{(1)}(x_{1/2})$	$\frac{-1}{2h}$	$\frac{1}{2h}$			$-\frac{1}{6}c^{(3)}(x_{1/2})h^2 + O(h^3)$
$c^{(2)}(x_{1/2})$	$\frac{-13}{11h^2}$	$\frac{14}{11h^2}$	$\frac{-1}{11h^2}$		$-\frac{3}{88}c^{(4)}(x_{1/2})h^2 + O(h^3)$
$c^{(3)}(x_{1/2})$	$\frac{85}{20h^3}$	$\frac{-147}{20h^3}$	$\frac{75}{20h^3}$	$\frac{-13}{20h^3}$	$\frac{203}{600}c^{(5)}(x_{1/2})h^2 + O(h^3)$
$c^{(2)}(x_1)$	$\frac{-1}{11h^2}$	$\frac{-4}{11h^2}$	$\frac{5}{11h^2}$		$-\frac{9}{44}c^{(4)}(x_1)h^2 + O(h^3)$
$c^{(3)}(x_1)$	$\frac{25}{10h^3}$	$\frac{-39}{10h^3}$	$\frac{15}{10h^3}$	$\frac{-1}{10h^3}$	$-\frac{2}{25}c^{(5)}(x_1)h^2 + O(h^3)$
$c^{(3)}(x_{3/2})$	$\frac{15}{20h^3}$	$\frac{-9}{20h^3}$	$\frac{-15}{20h^3}$	$\frac{9}{20h^3}$	$-\frac{149}{600}c^{(5)}(x_{3/2})h^2 + O(h^3)$

Table 4.3: One-dimensional FVM approximations for point values and low-order derivatives near the left boundary of the system. Any quantity not listed in this table may be estimated using the bulk formulas from Tables 4.1 and 4.2.

quantity of interest	coefficients				error
	$\bar{c}_{N-3}$	$\bar{c}_{N-2}$	$\bar{c}_{N-1}$	$\bar{c}_N$	
$c(x_N)$				1	$-\frac{1}{6}c^{(2)}(x_N)h^2 + O(h^3)$
$c^{(1)}(x_N)$					0
$c^{(2)}(x_N)$		$\frac{-7}{11h^2}$	$\frac{32}{11h^2}$	$\frac{-25}{11h^2}$	$\frac{17}{44}c^{(4)}(x_N)h^2 + O(h^3)$
$c^{(3)}(x_N)$	$\frac{6}{5h^3}$	$\frac{-30}{5h^3}$	$\frac{54}{5h^3}$	$\frac{-30}{5h^3}$	$\frac{151}{150}c^{(5)}(x_N)h^2 + O(h^3)$
$c^{(1)}(x_{N-1/2})$			$\frac{-1}{2h}$	$\frac{1}{2h}$	$-\frac{1}{6}c^{(3)}(x_{N-1/2})h^2 + O(h^3)$
$c^{(2)}(x_{N-1/2})$		$\frac{-1}{11h^2}$	$\frac{14}{11h^2}$	$\frac{-13}{11h^2}$	$-\frac{3}{88}c^{(4)}(x_{N-1/2})h^2 + O(h^3)$
$c^{(3)}(x_{N-1/2})$	$\frac{13}{20h^3}$	$\frac{-75}{20h^3}$	$\frac{147}{20h^3}$	$\frac{-85}{20h^3}$	$\frac{203}{600}c^{(5)}(x_{N-1/2})h^2 + O(h^3)$
$c^{(2)}(x_{N-1})$		$\frac{5}{11h^2}$	$\frac{-4}{11h^2}$	$\frac{-1}{11h^2}$	$-\frac{9}{44}c^{(4)}(x_{N-1})h^2 + O(h^3)$
$c^{(3)}(x_{N-1})$	$\frac{1}{10h^3}$	$\frac{-15}{10h^3}$	$\frac{39}{10h^3}$	$\frac{-25}{10h^3}$	$-\frac{2}{25}c^{(5)}(x_{N-1})h^2 + O(h^3)$
$c^{(3)}(x_{N-3/2})$	$\frac{-9}{20h^3}$	$\frac{15}{20h^3}$	$\frac{9}{20h^3}$	$\frac{-15}{20h^3}$	$-\frac{149}{600}c^{(5)}(x_{N-3/2})h^2 + O(h^3)$

Table 4.4: One-dimensional FVM approximations for point values and low-order derivatives near the right boundary of the system. Any quantity not listed in this table may be estimated using the bulk formulas from Tables 4.1 and 4.2.

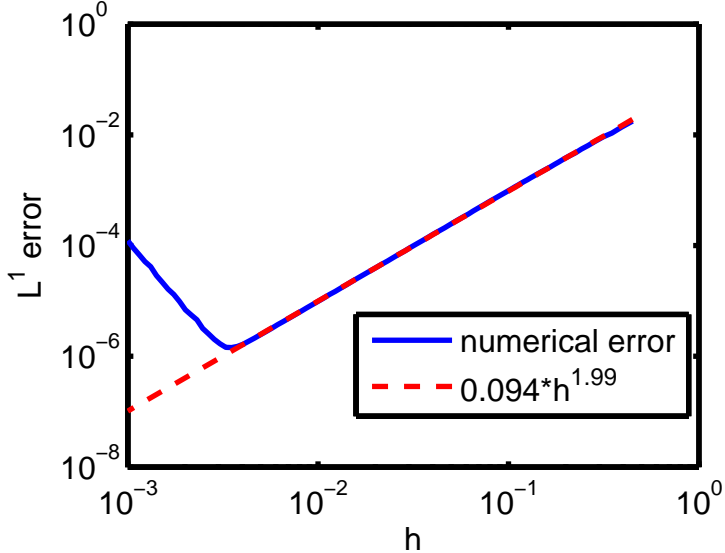


Figure 4-2: The  $L^1$ -error of our spatial approximation to  $\partial c / \partial t$  in one dimension as a function of  $h$ . Note that as  $h$  approaches and decreases past  $10^{-3}$ , we begin to lose accuracy due to rounding errors.

### 4.3 Two-Dimensional Geometries

In two-dimensional geometries, the control volumes are allowed to be polygons with arbitrary sizes and orientations. However, we will specialize to the case of rectilinear grids. As in the one-dimensional case, we will label the  $x$ -coordinates of the control volume boundaries  $x_0, x_1, \dots, x_N$  (so the total system width is  $L_x \equiv x_N - x_0$ ), the  $x$ -coordinates of the control volume midpoints by  $x_{i-1/2} \equiv \frac{1}{2}(x_{i-1} + x_i)$ , and the control volume widths by  $\Delta x_i \equiv x_i - x_{i-1}$ . Similarly, we label the  $y$ -coordinates of the control volume boundaries  $y_0, y_1, \dots, y_M$  (so the total system height is  $L_y \equiv y_M - y_0$ ), the  $y$ -coordinates of the control volume midpoints by  $y_{i-1/2} \equiv \frac{1}{2}(y_{i-1} + y_i)$ , and the control volume heights by  $\Delta y_i \equiv y_i - y_{i-1}$ . The average values used by the finite volume method are given by

$$\bar{c}_{i,j} \equiv \frac{1}{\Delta x_j \Delta y_i} \int_{y_{i-1}}^{y_i} \int_{x_{j-1}}^{x_j} c(x, y) dx dy \quad (4.3,2D)$$

for  $i = 1, 2, \dots, M$  and  $j = 1, 2, \dots, N$ . Further,  $J_{x,i,j}$  is the total flux in the  $x$ -direction across the line segment  $x_j \times [y_{i-1}, y_i]$ , and  $J_{y,i,j}$  is the total flux in the  $y$ -direction across the line segment  $[x_{j-1}, x_j] \times y_i$  (see Fig. 4-3 for a schematic). The system of equations solved by the method of lines is then

$$\frac{d\bar{c}_{i,j}}{dt} = -\frac{1}{\Delta x_j \Delta y_i} (J_{x,i,j} - J_{x,i,j-1} + J_{y,i,j} - J_{y,i-1,j}) . \quad (4.4,2D)$$

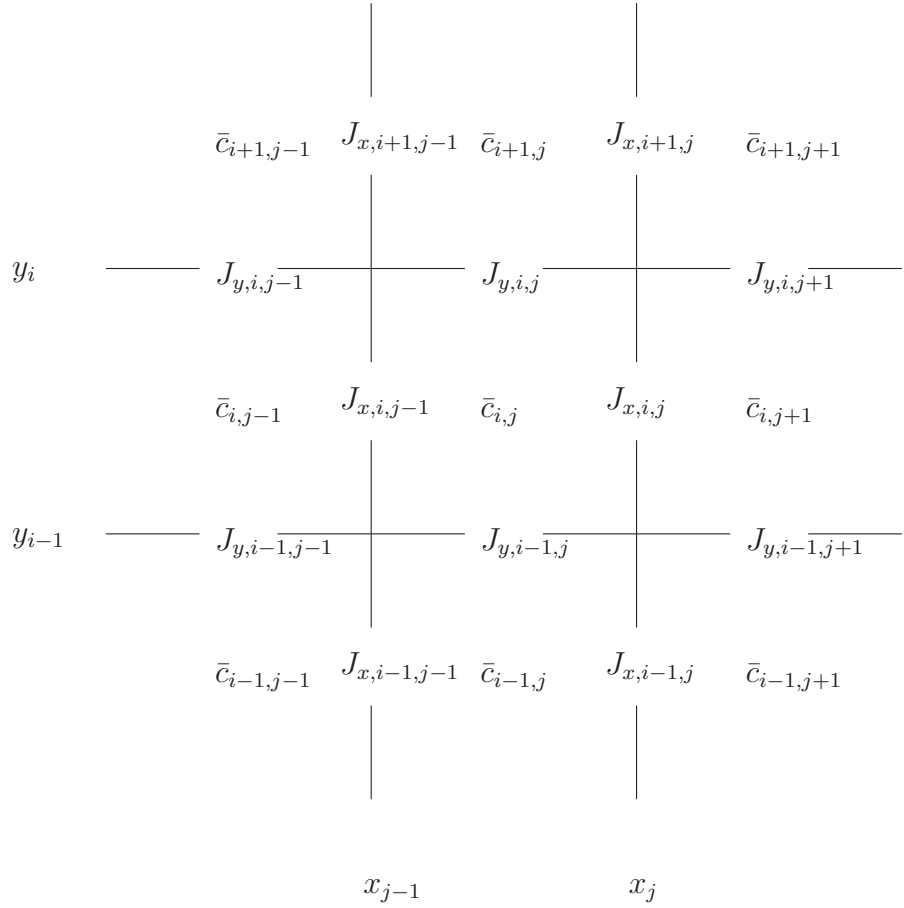


Figure 4-3: Schematic of the geometry for a two-dimensional finite volume method. The average value of  $c(x, y)$  in the rectangular region  $[x_{j-1}, x_j] \times [y_{i-1}, y_i]$  is approximated by  $\bar{c}_{i,j}$ . The  $x$ -components of the fluxes  $J_{x,i,j}$  are computed along the vertical edges  $x_j \times (y_{i-1}, y_i)$ , and the  $y$ -components of the fluxes  $J_{y,i,j}$  are computed along the horizontal edges  $(x_{j-1}, x_j) \times y_i$ .

### 4.3.1 General formulas

In more than one dimension, computing accurate total fluxes across a face of a control volume given only cell averages is very difficult (at least when the flux is a non-linear function). If only second-order accuracy is required, however, then each face's flux total may be replaced by the face's area (in 2-D, this is just the edge length) times the point value of the flux at the face's center. This is because the point value at the facial center is a second-order-accurate approximation for the facial average. We will therefore still focus on computing point values of  $c(x, y)$  and its derivatives.

If we specialize to a grid with uniform  $x$ -spacing  $h$  and uniform  $y$ -spacing  $k$ , then all of the formulas given in § 4.2.1 are valid with errors that are  $O(h^2 + k^2)$ . Mixed derivatives can also be derived from the 1-D equations. For example, away from the system boundaries we have:

$$\begin{aligned} \frac{1}{hk^2} [(\bar{c}_{i+1,j+1} - 2\bar{c}_{i,j+1} + \bar{c}_{i-1,j+1}) - (\bar{c}_{i+1,j} - 2\bar{c}_{i,j} + \bar{c}_{i-1,j})] \\ = \frac{\partial^3 u}{\partial x \partial y^2}(x_j, y_{i-1/2}) + O(h^2 + k^2) \end{aligned} \quad (4.5a)$$

$$\begin{aligned} \frac{1}{h^2 k} [(\bar{c}_{i+1,j+1} - 2\bar{c}_{i+1,j} + \bar{c}_{i+1,j-1}) - (\bar{c}_{i,j+1} - 2\bar{c}_{i,j} + \bar{c}_{i,j-1})] \\ = \frac{\partial^3 u}{\partial x^2 \partial y}(x_{j-1/2}, y_i) + O(h^2 + k^2) \end{aligned} \quad (4.5b)$$

Boundary conditions must be incorporated near the system edges. If we assume a Neumann condition  $\hat{\mathbf{n}} \cdot \nabla c = 0$  must hold (which is equivalent to the variational boundary condition (2.11) if  $\mathbf{K}$  is diagonal and  $\gamma$  is concentration-independent), then the resulting

approximations are:

$$\begin{aligned} \frac{1}{11hk^2} [(-13\bar{c}_{1,j+1} + 14\bar{c}_{2,j+1} - \bar{c}_{3,j+1}) - (-13\bar{c}_{1,j} + 14\bar{c}_{2,j} - \bar{c}_{3,j})] \\ = \frac{\partial^3 u}{\partial x \partial y^2}(x_j, y_{1/2}) + O(h^2 + k^2) \end{aligned} \quad (4.5c)$$

$$\begin{aligned} \frac{1}{11hk^2} [(-13\bar{c}_{M,j+1} + 14\bar{c}_{M-1,j+1} - \bar{c}_{M-2,j+1}) - (-13\bar{c}_{M,j} + 14\bar{c}_{M-1,j} - \bar{c}_{M-2,j})] \\ = \frac{\partial^3 u}{\partial x \partial y^2}(x_j, y_{M-1/2}) + O(h^2 + k^2) \end{aligned} \quad (4.5d)$$

$$\begin{aligned} \frac{1}{11h^2k} [(-13\bar{c}_{i+1,1} + 14\bar{c}_{i+1,2} - \bar{c}_{i+1,3}) - (-13\bar{c}_{i,1} + 14\bar{c}_{i,2} - \bar{c}_{i,3})] \\ = \frac{\partial^3 u}{\partial x^2 \partial y}(x_{1/2}, y_i) + O(h^2 + k^2) \end{aligned} \quad (4.5e)$$

$$\begin{aligned} \frac{1}{11h^2k} [(-13\bar{c}_{i+1,N} + 14\bar{c}_{i+1,N-1} - \bar{c}_{i+1,N-2}) - (-13\bar{c}_{i,N} + 14\bar{c}_{i,N-1} - \bar{c}_{i,N-2})] \\ = \frac{\partial^3 u}{\partial x^2 \partial y}(x_{N-1/2}, y_i) + O(h^2 + k^2) \end{aligned} \quad (4.5f)$$

### 4.3.2 The Cahn-Hilliard equation

In two dimensions, there is no longer a single natural time or length scale, so we must keep many of the constants in the problem. We will assume that the non-dimensionalized diffusivity and gradient penalty tensors are constants of the form

$$\mathbf{D} = \begin{pmatrix} D_x & 0 \\ 0 & D_y \end{pmatrix} \quad \mathbf{K} = \begin{pmatrix} \lambda_x^2 & 0 \\ 0 & \lambda_y^2 \end{pmatrix}.$$

Then the non-dimensional conservation equation is given by

$$\frac{\partial c}{\partial t} = -\frac{\partial J_x}{\partial x} - \frac{\partial J_y}{\partial y}$$

where the non-dimensional flux  $\mathbf{J} = (J_x, J_y)$  is defined by

$$\begin{aligned} J_x &= D_x \left[ 2ac \frac{\partial c}{\partial x} - \frac{1}{1-c} \frac{\partial c}{\partial x} + \lambda_x^2 c \frac{\partial^3 c}{\partial x^3} + \lambda_y^2 c \frac{\partial^3 c}{\partial x \partial y^2} \right] \\ J_y &= D_y \left[ 2ac \frac{\partial c}{\partial y} - \frac{1}{1-c} \frac{\partial c}{\partial y} + \lambda_x^2 c \frac{\partial^3 c}{\partial x^2 \partial y} + \lambda_y^2 c \frac{\partial^3 c}{\partial y^3} \right] \end{aligned}$$

(see Eqs. 2.26).

This is computed by using the equations from § 4.2.1 to compute the non-mixed derivatives and those from § 4.3.1 to compute the mixed ones. The result is a second-order-accurate approximation for  $\mathbf{J}$  and a 13-point stencil for the  $d\bar{c}_{i,j}/dt$  (c.f. Fig. 4-4). Further, numerical

tests confirm that the corresponding approximation for the time derivatives is also  $O(h^2+k^2)$  (c.f. Fig. 4-5).

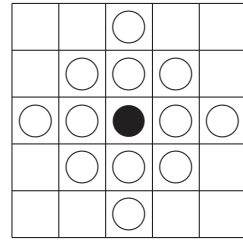


Figure 4-4: The 13-point stencil for our second-order-accurate, two-dimensional FVM scheme for the Cahn-Hilliard equation. In computing an approximation for  $d\bar{c}_{i,j}/dt$  in the cell with the black circle, only the  $\bar{c}$  values in the 13 cells with circles are used.

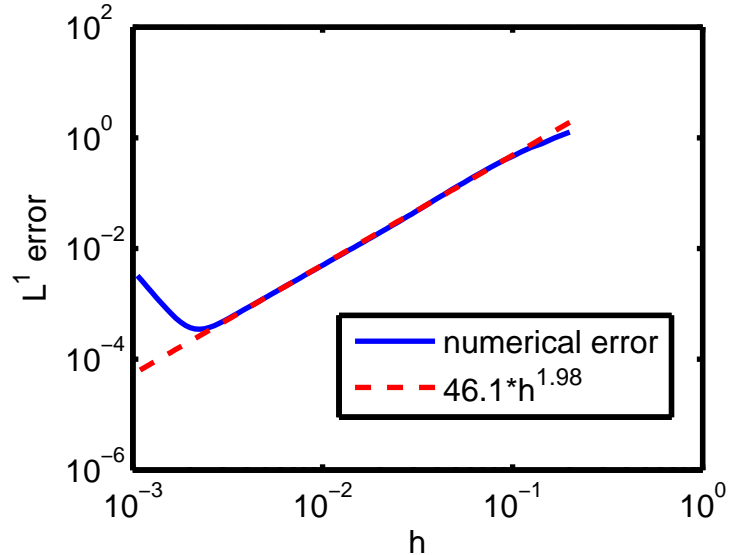


Figure 4-5: The  $L^1$ -error of our spatial approximation to  $\partial c/\partial t$  in two dimensions as a function of  $h(=k)$ . Note that as  $h$  approaches and decreases past  $10^{-3}$ , we begin to lose accuracy due to rounding errors.

# Chapter 5

## Stochastic Phase-Field Models

In many physical systems, there are *metastable* states occupying *local* free energy minima but separated from the *global* free energy minimum via a free energy barrier. The transition between these states is frequently driven by random thermal motions which are not adequately described by macroscopic evolution equations. Even in cases in which thermal motion is accounted for at some level by the evolution equations (for instance, a derivation of the diffusion equation via Brownian motions), the macroscopic equations can typically be proven to strictly reduce the free energy as a function of time. In all of these cases, having a stochastic version of the deterministic equations can help us to understand the transitions to equilibrium.

There are also other reasons to consider stochastic models. For instance, in large systems, deterministic equations can safely ignore thermal noise effects. However, in small systems, typical energy scales might now be on the order of the thermal energy  $k_B T$ . In these cases, the macroscopic, mean-field forces considered in the large systems are no longer the only dominant forces. Just from a scaling perspective, we must now account for thermal noise; since doing this exactly might still be prohibitive (our system is probably still large enough to contain many, many atoms), a stochastic approach is useful.

There seem to be two general techniques for understanding physical systems with (Gaussian white) noise: the stochastic-differential-equation approach based on the Langevin equation and the probability-density-function approach based on the Fokker-Planck equation. While some authors have argued that only the former [24] or the latter [87] is necessary, both are very useful.

Stochastic models are most frequently used for Brownian motion, so the equations describe the dynamics of systems with a small number of degrees of freedom. We wish to extend the analysis to systems in which a *field*—rather than just a particle—evolves stochastically. At least in the Cahn-Hilliard setting, this was first done using a Langevin approach by Cook [25] and using a Fokker-Planck approach by Langer [64].

The so-called Cahn-Hilliard-Cook equation is almost universally written as

$$\frac{\partial c}{\partial t} = M \nabla^2 \frac{\delta F}{\delta c} + \eta$$

where  $F$  is a free energy functional. The stochastic noise  $\eta$  is Gaussian with 0 mean and variance

$$\langle \eta(\mathbf{x}, t) \eta(\mathbf{x}', t') \rangle = 2k_B T M \nabla^2 \delta(\mathbf{x} - \mathbf{x}') \delta(t - t')$$

(N.B.  $c$ -independent mobility is assumed here). It is usually pointed out that this is equivalent to Langer's Fokker-Planck equation

$$\frac{\partial \rho}{\partial t} = - \int_V \frac{\delta J}{\delta c} dV ,$$

where the probability flux is given by

$$J = M \nabla^2 \left[ \frac{\delta F}{\delta c} \rho + k_B T \frac{\delta \rho}{\delta c} \right] .$$

These equations can be very difficult to understand and use. First, what does it mean for a random variable to have variance equal to the second derivative of the delta function, and how can this be simulated numerically? Second, how do you solve the Fokker-Planck equation with a continuum of variables? Third, how do you derive these, prove their equivalence, or extend the equations to different settings ( $c$ -dependent mobilities, for example)?

There are very few good reference for this material. The Cahn-Hilliard-Cook equation is frequently used, but only in the form above, and derivations are never included. Moreover, most authors only work with the Fourier transform of the equation (by converting  $\nabla^2 \delta$  to  $-k^2$ ). Many works cite the famous review article by Hohenberg and Halperin [50], but this paper focuses on applications to critical phenomena, and does not give derivations. Indeed, there are many papers which refer readers interested in derivations to other works which themselves include no derivations.

In this Chapter, we will explain the Langevin and Fokker-Planck approaches to stochastic fields in a way that is easily generalized and implemented numerically. The only prerequisite is an understanding of their finite-dimensional versions.

## 5.1 Stochastic Variables

We will always use Greek letters for stochastic variables and functions, and English letters for deterministic ones. Excellent general references for this material include [20] and [97].

### 5.1.1 Multivariate Fokker-Planck Equation

The Fokker-Planck equation is an exact PDE for the probability density function of a Markov process with Gaussian,  $\delta$ -correlated noise [87]. We denote by the vector  $\mathbf{x}$  a single point in phase space, and by  $\rho(\mathbf{x}, t)$  the probability density function of our system. Its evolution is

governed by the conservation equation

$$\frac{\partial \rho}{\partial t} = - \sum_i \frac{\partial J_i}{\partial x_i} \quad (5.1a)$$

where the “probability flux”  $\mathbf{J}$  is a vector whose  $i^{\text{th}}$  component is

$$J_i(\mathbf{x}, t) = D_i^{(1)}(\mathbf{x}, t)\rho(\mathbf{x}, t) - \sum_j \frac{\partial}{\partial x_j} \left[ D_{ij}^{(2)}(\mathbf{x}, t)\rho(\mathbf{x}, t) \right]. \quad (5.1b)$$

The  $D_i^{(1)}$  are called the drift coefficients, and the  $D_{ij}^{(2)}$  are called the diffusion coefficients. They are defined by

$$D_i^{(1)}(\mathbf{x}, t) = \lim_{\tau \rightarrow 0} \frac{\langle \Delta x_i \rangle}{\tau} = \lim_{\tau \rightarrow 0} \frac{1}{\tau} \int (x'_i - x_i) P(\mathbf{x}', t + \tau | \mathbf{x}, t) d\mathbf{x}' \quad (5.1c)$$

$$D_{ij}^{(2)}(\mathbf{x}, t) = \lim_{\tau \rightarrow 0} \frac{\langle (\Delta x_i)(\Delta x_j) \rangle}{2\tau} = \lim_{\tau \rightarrow 0} \frac{1}{2\tau} \int (x'_i - x_i)(x'_j - x_j) P(\mathbf{x}', t + \tau | \mathbf{x}, t) d\mathbf{x}' \quad (5.1d)$$

where  $P$  is the transition probability function.

### 5.1.2 Multivariate Langevin Equation

The Langevin equation is a stochastic ODE for the time evolution of a set of random variable through phase space [24]. For any vector  $\boldsymbol{\xi} = \boldsymbol{\xi}(t)$  of stochastic variables, the Langevin equation is given by

$$\dot{\xi}_i = h_i(\boldsymbol{\xi}, t) + \eta_i(\boldsymbol{\xi}, t) \quad (5.2a)$$

where the  $h_i$  are deterministic functions and the  $\eta_i$  are the stochastic noise terms. The most commonly-assumed form for the noise is

$$\eta_i(\boldsymbol{\xi}, t) = \sum_j g_{ij}(\boldsymbol{\xi}, t) \Gamma_j(t) \quad (5.2b)$$

where the  $g_{ij}$  are deterministic functions and each  $\Gamma_j$  is a Gaussian white noise satisfying

$$\langle \Gamma_j(t) \rangle = 0 \quad (5.2c)$$

$$\langle \Gamma_j(t) \Gamma_k(t') \rangle = 2b_{jk}\delta(t - t') \quad (5.2d)$$

(this is a slight generalization of the equations discussed in [24]). The  $b_{jk}$  are real numbers giving the correlations between the different  $\Gamma_i$ 's, and are typically equal to the Kronecker delta function. The factor of 2 is a convenience which obviates extra factors later.

The Gaussian white noises used above are the “derivatives” of Wiener processes. To see

this, note that

$$W_i(t) \equiv \int_0^t \Gamma_i(t') dt'$$

is Gaussian with 0-mean and variance equal to  $2b_{ii}t$ . Note, however, that the Wiener process is differentiable with probability 0 [58], which explains the presence of the delta function in (5.2d). We therefore must interpret (5.2a) as an integral equation

$$\xi_i(t) - \xi_i(0) = \int_0^t h_i(\boldsymbol{\xi}(t'), t') dt' + \sum_j \int_0^t g_{ij}(\boldsymbol{\xi}(t'), t') dW_i(t') .$$

For *multiplicative noise*—systems in which the  $g_{ij}$  are  $\boldsymbol{\xi}$ -dependent—this integral is not uniquely defined. The most common definitions are those of Itô and Stratonovich, but for physical systems in which the white noise is taken as the limit of continuous noises with finite correlation times that approach 0, we must use the Stratonovich integral [87].

The above equation is equivalent to a Fokker-Planck equation with parameters

$$D_i^{(1)}(\boldsymbol{\xi}, t) = h_i(\boldsymbol{\xi}, t) \quad [\text{Itô}] \text{ or} \quad (5.3a)$$

$$D_i^{(1)}(\boldsymbol{\xi}, t) = h_i(\boldsymbol{\xi}, t) + \sum_{j,k,l} b_{jl} g_{kl}(\boldsymbol{\xi}, t) \frac{\partial}{\partial \xi_k} g_{ij}(\boldsymbol{\xi}, t) \quad [\text{Stratonovich}], \text{ and} \quad (5.3b)$$

$$D_{ij}^{(2)}(\boldsymbol{\xi}, t) = \sum_{k,l} b_{kl} g_{ik}(\boldsymbol{\xi}, t) g_{jl}(\boldsymbol{\xi}, t) . \quad (5.3c)$$

If we employ matrix notation (so  $\mathbf{g} = (g_{ij})$ ,  $\mathbf{b} = (b_{ij})$ , etc.), then we get the following modified Fokker-Planck probability flux for the Stratonovich interpretation of the Langevin equation:

$$\mathbf{J} = [\mathbf{h} - \mathbf{g}\mathbf{b}(\nabla \cdot \mathbf{g})^T] \rho - \mathbf{g}\mathbf{b}\mathbf{g}^T \nabla \rho \quad (5.3d)$$

where  $\nabla \cdot \mathbf{g}$  is the row vector whose  $i^{\text{th}}$  element is  $\sum_k \frac{\partial}{\partial \xi_k} g_{ki}$ .

The extra term in (5.3b) is usually called the Stratonovich drift or the spurious drift. In either case, though, the expected value evolves according to

$$\dot{\langle \xi_i \rangle} = D_i(\boldsymbol{\xi}, t) . \quad (5.4)$$

Thus, when using the Stratonovich integral, one cannot just set  $\mathbf{h}$  equal to the time derivative of the deterministic system.

Finally, we include for future reference the exact form of the covariance matrix of the noise terms,  $\boldsymbol{\Sigma}(\boldsymbol{\xi}, t, \boldsymbol{\xi}', t') = (\Sigma_{ij}) = (\langle \eta_i(\boldsymbol{\xi}, t)\eta_j(\boldsymbol{\xi}', t') \rangle)$ . Regardless of the integral interpretation, it is given by

$$\boldsymbol{\Sigma}(\boldsymbol{\xi}, t, \boldsymbol{\xi}', t') = 2\mathbf{g}(\boldsymbol{\xi}, t)\mathbf{b}\mathbf{g}(\boldsymbol{\xi}', t')^T \delta(t - t') . \quad (5.5)$$

### 5.1.3 Discrete Approximation of the Variational Derivative

Our goal in this Chapter is to add stochastic noise to the variational thermodynamic equations of Chapter 2 in a way that is easily discretized. We must therefore briefly discuss discretizing the operations employed from the calculus of variations. In particular, given a functional

$$F[c(\mathbf{x}, t), t] = \int_V f(c(\mathbf{x}, t), \nabla c(\mathbf{x}, t), \mathbf{x}, t) dV ,$$

we would like to compute a discrete approximation of the variational derivative

$$\frac{\delta F}{\delta c} \equiv \frac{\partial f}{\partial c} - \nabla \cdot \frac{\partial f}{\partial \nabla c} .$$

For simplicity, we will only work out the 1-dimensional case.

We choose evenly-spaced points  $x_1, \dots, x_n$  in the region of interest, and we employ the notation  $c_i \equiv c(x_i, t)$ . Any linear approximation scheme for derivatives is given by a matrix  $\mathbf{D} = (D_{ij})$  such that

$$\frac{\partial c}{\partial x}(x_i, t) \approx \sum_{j=1}^n D_{ij} c_j .$$

Then the Riemann approximation for our integral gives us

$$F(\mathbf{c}, t) \approx \sum_{i=1}^n f \left( c_i, \sum_{j=1}^n D_{ij} c_j, x_i, t \right) \Delta x ,$$

where we have defined  $\Delta x \equiv x_i - x_{i-1}$ . Given this approximation, we may compute

$$\frac{1}{\Delta x} \frac{\partial F}{\partial c_k}(\mathbf{c}, t) = \frac{\partial f}{\partial c} \left( c_k, \sum_{j=1}^n D_{kj} c_j, x_k, t \right) + \sum_{i=1}^n D_{ik} \frac{\partial f}{\partial c'} \left( c_i, \sum_{j=1}^n D_{ij} c_j, x_i, t \right)$$

where  $\frac{\partial f}{\partial c'}$  is the derivative of  $f$  with respect to  $\frac{\partial c}{\partial x}$ . If we assume that  $\mathbf{D}^T = -\mathbf{D}$  (which holds, for instance, in any centered-difference scheme, though care must be exercised near the boundaries), then

$$\begin{aligned} \frac{1}{\Delta x} \frac{\partial F}{\partial c_k}(\mathbf{c}, t) &= \frac{\partial f}{\partial c} \left( c_k, \sum_{j=1}^n D_{kj} c_j, x_k, t \right) - \sum_{i=1}^n D_{ki} \frac{\partial f}{\partial c'} \left( c_i, \sum_{j=1}^n D_{ij} c_j, x_i, t \right) \\ &\approx \frac{\partial f}{\partial c} \Big|_{x_k, t} - \frac{d}{dx} \frac{\partial f}{\partial c'} \Big|_{x_k, t} \\ &= \frac{\delta F}{\delta c}(x_k, t) . \end{aligned}$$

Generalizing to full dimensionality, we get

$$\frac{\delta F}{\delta c}(x_k, t) \approx \frac{1}{\Delta V} \frac{\partial F}{\partial c_k}(\mathbf{c}, t) \quad (5.6)$$

where now  $\Delta V$  is the volume of each element in our discretized space.

## 5.2 Stochastic Fields

We now begin with the continuum case. Suppose  $c(\mathbf{x}, t)$  is a physical field whose deterministic evolution is modeled by the equation

$$\frac{\partial c}{\partial t} = \mathcal{L} \left[ \frac{\delta F}{\delta c} \right] \quad (5.7)$$

for some functional  $F$  (typically a free energy) and some linear differential operator  $\mathcal{L}$ . If we wish to include the random effects of thermal noise, it might seem reasonable to consider the Langevin-type equation

$$\frac{\partial c}{\partial t} = \mathcal{L} \left[ \frac{\delta F}{\delta c} \right] + \eta(c, \mathbf{x}, t)$$

for some stochastic term  $\eta$ . However, keeping in mind Eq. 5.4, it is not clear that the expected value of the stochastic field would evolve according to (5.7), nor is it obvious how to choose a noise term.

### 5.2.1 Discrete Approximation

We will overcome these difficulties by first discretizing our mean-field equation and then adding noise. We begin by choosing a discrete set of points  $\{x_1, \dots, x_n\}$  in space; each “point” may be a vector, depending on the dimensionality of the underlying space. We then store an approximation  $c_i(t) \approx c(x_i, t)$  for the field only at these points, and denote by  $\mathbf{c}$  the vector  $(c_1, \dots, c_n)$ . We then assume our discrete, deterministic field evolves according to

$$\frac{\partial c_i}{\partial t} = \sum_j L_{ij}(\mathbf{c}, t) \cdot \frac{1}{\Delta V} \frac{\partial F(\mathbf{c}, t)}{\partial c_j} \quad (5.8)$$

(note the use of Eq. 5.6). Our differential operator  $\mathcal{L}$  is now approximated by the matrix  $\mathbf{L} = (L_{ij})$ ; it may depend explicitly on the field  $c$ , time  $t$ , and space (via  $i$  and  $j$ ).

Now, to extend our deterministic equation to a stochastic one, we assume that our discrete, noisy field will evolve according to the Langevin equation (5.2). In order to recover the deterministic behavior (5.8) as the expected value of the stochastic behavior under the

Stratonovich interpretation, we must choose the Langevin parameters according to (5.4)

$$\mathbf{h} - \mathbf{g}\mathbf{b}(\nabla \cdot \mathbf{g})^T + [\nabla \cdot (\mathbf{g}\mathbf{b}^T\mathbf{g}^T)]^T = \frac{1}{\Delta V} \mathbf{L} \nabla F \quad (5.9)$$

(note that we have rewritten the derivative term in Eq. 5.3b).

We now have a Langevin equation from which we can recover our mean-field behavior in the average sense. We have not, however, fully determined the noise covariances. To do this, we make the additional assumption that

$$\rho(\mathbf{c}, t) = A e^{-F(\mathbf{c}, t)/k_B T}$$

is a stationary distribution for our system, i.e. that the Fokker-Planck probability flux is identically  $\mathbf{0}$  for this  $\rho$ . Here  $k_B$  is Boltzmann's constant,  $T$  is the temperature, and  $A$  is just a normalization constant. This can be understood from a canonical-ensemble point of view if we take  $F$  to be a coarse-grained free energy (c.f. [64] and [50]).

Substituting this into (5.3d) and using (5.9), we get the new requirement

$$\left\{ \mathbf{L} + \frac{\Delta V}{k_B T} \mathbf{g}\mathbf{b}\mathbf{g}^T \right\} \nabla F = [\nabla \cdot (\mathbf{g}\mathbf{b}^T\mathbf{g}^T)]^T \Delta V \quad (5.10)$$

This is called the *fluctuation-dissipation theorem* for our system; it specifies a constraint on the noise  $\mathbf{g}$  as a function of the generalized Onsager coefficients  $\mathbf{L}$ .

Since our space is discretized into  $n$  discrete points, there are  $2n^2 + n$  unknown functions between the vector  $\mathbf{h}$  and the matrices  $\mathbf{g}$  and  $\mathbf{b}$ . Our requirements (5.9) and (5.10) only give  $2n$  constraints. If  $c$  is a conserved quantity, we might also require

$$\sum_{i,j} g_{ij} = 0 \quad (5.11)$$

in which case the stochastic noise will be strictly conservative. This provides only one additional constraint, though, and there are no others that we could generally impose here (though see the next section). We must therefore accept that the stochastic equations as derived here are not uniquely defined.

### 5.2.2 Generalization

We have said nothing about the identity of our  $c$  field. We could, for instance, be interested in adding stochastic noise to deterministic equations for the evolution of concentration fields [16], elastic strain [65], or crystallinity [94]. More generally, it could be a combination of several different fields. In this case, our free energy depends on the fields  $\psi_1, \psi_2, \dots, \psi_m$ , and our equations of motion are of the form

$$\frac{\partial \psi_i}{\partial t} = \sum_j \mathcal{L}_{ij} \left[ \frac{\delta F}{\delta \psi_j} \right] .$$

Now we have a matrix of linear differential operators  $\mathcal{L}_{ij}$  (hopefully making it more clear why we have been calling our  $\mathcal{L}$  a generalized Onsager coefficient). Even in this general situation, we can still apply the above recipe exactly to get a discrete Langevin equation for a noisy version of our system.

### 5.2.3 Continuum Equations

As mentioned in the introduction, the continuum versions of the evolution equations are difficult to use and interpret. For completeness, however, we will demonstrate their derivation as the continuum limits of the discrete systems discussed in § 5.2.1.

We begin by making additional assumptions about the noise terms:

$$\mathbf{g}\mathbf{b}(\nabla \cdot \mathbf{g})^T = \mathbf{0} \quad (5.12)$$

$$\nabla \cdot (\mathbf{g}\mathbf{b}^T\mathbf{g}^T) = \mathbf{0} \quad (5.13)$$

$$\mathbf{g}\mathbf{b}\mathbf{g}^T = -\left(\frac{k_B T}{\Delta V}\right) \mathbf{L} \quad (5.14)$$

(note that (5.14) is not quite a consequence of (5.13) and (5.10)). If  $\mathcal{L}$  were  $c$ -independent, it would be reasonable to assume that  $\mathbf{g}$  and  $\mathbf{b}$  would be constant, in which case (5.12) and (5.13) would be trivial. In the general setting, though, these cannot be rigorously justified without a more detailed model of the noise. In particular, note that (5.13) and (5.14) together impose an additional requirement on  $\mathbf{L}$  (namely that  $\nabla \cdot \mathbf{L}^T = \mathbf{0}$ ); this matrix is given to us via the mean-field, deterministic dynamics, so we are not at liberty to change it. With these assumptions, however, (5.10) is satisfied identically, and (5.9) holds simply by letting  $\mathbf{h}$  equal the right side of the deterministic equation.

The resulting Langevin equation in vector form is given by

$$\dot{\mathbf{c}}(t) = \mathbf{L}(\mathbf{c}, t) \cdot \frac{1}{\Delta V} \nabla F(\mathbf{c}, t) + \boldsymbol{\eta}(\mathbf{c}, t)$$

and the covariance of the noise vector (c.f. Eq. 5.5) is given by

$$\langle \eta_i(\mathbf{c}, t) \eta_j(\mathbf{c}, t') \rangle = -2k_B T \delta(t - t') \cdot L_{ij}(\mathbf{c}, t) \frac{1}{\Delta V} .$$

In the continuum limit, we then get

$$\frac{\partial c(\mathbf{x}, t)}{\partial t} = \mathcal{L}(c, \mathbf{x}, t) \left[ \frac{\delta F}{\delta c}(\mathbf{x}, t) \right] + \eta(c, \mathbf{x}, t) \quad (5.15a)$$

$$\langle \eta(c, \mathbf{x}, t) \eta(c, \mathbf{x}', t') \rangle = -2k_B T \delta(t - t') \mathcal{L}(c, \mathbf{x}, t) [\delta(\mathbf{x} - \mathbf{x}')] . \quad (5.15b)$$

When  $\mathcal{L} = \nabla^2$ , this is the Cahn-Hilliard-Cook equation (though it was not written quite like this in Cook's original paper [25]). This is also how Model B dynamics are described by Hohenberg and Halperin [50]; their Model A dynamics are also a special case of the above

with  $\mathcal{L}$  equal to a constant.

The resulting modified Fokker-Planck probability flux in vector form is given by

$$\mathbf{J}(\mathbf{c}, t) = \mathbf{L}(\mathbf{c}, t) \left[ \rho(\mathbf{c}, t) \frac{1}{\Delta V} \nabla F(\mathbf{c}, t) + k_B T \frac{1}{\Delta V} \nabla \rho(\mathbf{c}, t) \right] .$$

Using the Riemann-sum approximation for integrals along with (5.6), we get the following in the continuum limit:

$$\frac{\partial \rho(c, t)}{\partial t} = - \int \frac{\delta}{\delta c} \left( \mathcal{L}(c, \mathbf{x}, t) \left[ \frac{\delta F}{\delta c}(\mathbf{x}, t) \rho(c, t) + k_B T \frac{\delta \rho}{\delta c}(\mathbf{x}, t) \right] \right) d\mathbf{x} . \quad (5.16)$$

The special case for  $\mathcal{L} = \nabla^2$  was more rigorously derived by Langer [64].

Even aside from being able to derive the continuum equations, the above assumptions yield another nice property. The Stratonovich drift vanishes, so the Stratonovich and Itô integrals coincide [87]. Therefore, despite the fact that we still may have multiplicative noise (indeed, see § 5.2.4 for an example in which the assumptions above are satisfied even for  $c$ -dependent  $g_{ij}$ ), we may use the Itô integral for simulations. In general, this will make the numerics easier to implement.

### 5.2.4 Example

Suppose we wish to add stochastic noise to the 1-dimensional Cahn-Hilliard system (2.26)

$$\begin{aligned} \mu &= \frac{1}{\rho} \frac{\delta F}{\delta c} \\ J &= -\rho B(c, x) \frac{\partial \mu}{\partial x} \\ \frac{\partial(\rho c)}{\partial t} &= -\frac{\partial J}{\partial x} \end{aligned}$$

with (potentially  $c$ - and  $x$ -dependent) mobility  $B$  and constant  $\rho$ . Then our differential operator may be written

$$\mathcal{L} = \frac{1}{\rho} \frac{\partial}{\partial x} \left[ B(c, x) \frac{\partial}{\partial x} \right] .$$

In the centered-difference finite volume method discretization assuming no-flux boundary conditions, we get the approximation

$$\mathbf{L} = \frac{1}{\rho(\Delta x)^2} \begin{pmatrix} -B_{1-2} & B_{1-2} & 0 & \cdots & 0 & 0 \\ B_{1-2} & -(B_{1-2} + B_{2-3}) & B_{2-3} & \cdots & 0 & 0 \\ 0 & \ddots & \ddots & \ddots & 0 & 0 \\ 0 & 0 & \ddots & \ddots & \ddots & 0 \\ 0 & 0 & \cdots & B_{(n-2)-(n-1)} & -(B_{(n-2)-(n-1)}) & B_{(n-1)-n} \\ 0 & 0 & \cdots & 0 & B_{(n-1)-n} & -B_{(n-1)-n} \end{pmatrix}.$$

As usual,  $\Delta x$  denotes the (uniform) spacing between points. The quantity  $B_{i-(i+1)}$  is an approximation for the function  $B(c, x)$  at the midpoint between  $x_i$  and  $x_{i+1}$ ; for instance, if  $B(c, x) = c \frac{D}{k_B T}$  for constant  $D$ , we would choose  $B_{i-(i+1)} = \frac{1}{2}(c_i + c_{i+1}) \frac{D}{k_B T}$ .

Now we choose  $\mathbf{b} = \mathbf{I} = (\delta_{ij})$  and

$$\mathbf{g} = \sqrt{\frac{k_B T}{\rho(\Delta x)^3}} \begin{pmatrix} 0 & -\sqrt{B_{1-2}} & 0 & \cdots & 0 & 0 \\ 0 & \sqrt{B_{1-2}} & -\sqrt{B_{2-3}} & \cdots & 0 & 0 \\ 0 & \ddots & \ddots & \ddots & 0 & 0 \\ 0 & 0 & \ddots & \ddots & \ddots & 0 \\ 0 & 0 & \cdots & 0 & \sqrt{B_{(n-2)-(n-1)}} & -\sqrt{B_{(n-1)-n}} \\ 0 & 0 & \cdots & 0 & 0 & \sqrt{B_{(n-1)-n}} \end{pmatrix}.$$

Then (5.14) holds identically. Further, if we add the additional requirement that the approximation  $B_{i-(i+1)}$  is a symmetric function of  $c_i$  and  $c_{i+1}$  (note that it may still have arbitrary dependencies on the other  $\mathbf{c}$ -components), then (5.12) and (5.13) also hold. We therefore get a Langevin equation which satisfies our fluctuation-dissipation theorem; whose deterministic part is identically equal to the right-hand side of the deterministic evolution equation; and which may be simulated using the Itô integral.

Note that this is easily extended to finite volume methods for this same problem in higher dimensions. In this case, we get a  $\mathbf{g}$  matrix as above for each direction. The prefactor need only be changed to  $\sqrt{k_B T / \rho(\Delta V)(\Delta x)^2}$ . Regardless of the dimensionality,  $\sum_{i,j} g_{ij} = 0$ , so the noise is strictly conservative (c.f. Eq. 5.11).

We do have a fairly serious problem, though. Let  $B$  be a typical scale for the  $B_{i-(i+1)}$ . Then a typical value of  $g_{ij}$  is  $\sim \sqrt{B k_B T / \rho(\Delta V)(\Delta x)^2}$ . In simulations, we need the noise terms to be very small during each time-step. If the length of a time step is denoted  $\Delta t$ , then we require

$$\sqrt{\frac{B k_B T}{\rho} \frac{\Delta t}{(\Delta V)(\Delta x)^2}} \ll 1.$$

This is an extremely strict constraint, especially when the stability of the deterministic

integration scheme may only require

$$Bk_B T \frac{\Delta t}{(\Delta x)^2} < 1 .$$

THIS PAGE INTENTIONALLY LEFT BLANK

# Chapter 6

## Dynamical Regimes of the CHR System

The partial differential equation discussed in § 2.5 is obviously mathematically complex: it is a nonlinear, 4<sup>th</sup>-order equation with non-linear, 3<sup>rd</sup>-order boundary conditions. Consequently, there is little hope for analytic results. Unfortunately, the equation is also difficult to analyze physically. Though the microscopic energies are likely all on the scale of  $k_B T$ , there are potentially six different length scales (each spatial direction has an associated atomic-scale  $\lambda_i$  and a particle-scale  $L_i$ ) and nine different time scales (diffusion in each direction across phase boundary widths, diffusion in each direction across the entire particle, and reaction time scales at each crystal face) in the model.

For easy reference, we define a *CHR* (Cahn-Hilliard with Reaction boundary conditions) system to be one for which a non-dimensional concentration field  $c = c(\mathbf{x}, t)$  satisfies the following PDE:

$$\mu = a(1 - 2c) + k_B T \log\left(\frac{c}{1 - c}\right) - \boldsymbol{\nabla} \cdot (\mathbf{K} \boldsymbol{\nabla} c) \quad (6.1a)$$

$$\mathbf{J} = -\rho c \mathbf{D} \boldsymbol{\nabla} (\mu / k_B T) \quad (6.1b)$$

$$\frac{\partial c}{\partial t} = -\frac{1}{\rho} \boldsymbol{\nabla} \cdot \mathbf{J} = \boldsymbol{\nabla} \cdot (c \mathbf{D} \boldsymbol{\nabla} \mu / k_B T) \quad (6.1c)$$

with boundary conditions

$$\hat{\mathbf{n}} \cdot (\mathbf{K} \boldsymbol{\nabla} c) = 0 \quad (6.1d)$$

$$\hat{\mathbf{n}} \cdot \mathbf{J} = -\rho_s R . \quad (6.1e)$$

As used here,  $R$  is the net rate at which material enters the system via boundary reactions. We do not specify its exact form, but note that it will generally depend on the local concentration and chemical potential. We will assume that the diffusivity and gradient-penalty

tensors are both diagonal and constant:

$$\mathbf{D} = \begin{pmatrix} D_x & & \\ & D_y & \\ & & D_z \end{pmatrix} \quad \text{and} \quad \mathbf{K} = k_B T \begin{pmatrix} \lambda_x^2 & & \\ & \lambda_y^2 & \\ & & \lambda_z^2 \end{pmatrix}.$$

Finally, we denote by  $V$  the region of space occupied by our crystal. For simplicity, we will assume that  $V$  is the rectangular parallelepiped  $[0, L_x] \times [0, L_y] \times [0, L_z]$ .

We have already shown (see § 2.5.1) that the natural length scale over which the concentration and chemical potential fields vary in the  $i$ -direction is given by  $\lambda_i$ . The natural time scale for diffusive fluxes in the  $i$ -direction is therefore  $\tau_i^D \equiv \lambda_i^2/D_i$ . However, the boundary reactions can occur at much different time scales, which we denote by  $\tau_i^R$ . This disparity is quantified by the non-dimensional *Damköhler numbers*

$$\text{Da}_i \equiv \frac{\tau_i^D}{\tau_i^R}. \quad (6.2)$$

Clearly the bulk diffusion equation (6.1c) can be neatly non-dimensionalized using only the time scales  $\tau_i^D$ , and similarly the boundary reaction rates should be non-dimensionalized using only the time scales  $\tau_i^R$ . Thus the Damköhler numbers only impact the CHR dynamics through the reaction boundary condition (6.1e). Indeed, at any crystal-electrolyte interface perpendicular to  $\hat{\mathbf{e}}_{(i)}$ , combining the above non-dimensionalizations yields

$$\tilde{J}_i = -\text{Da}_i \tilde{R}_i$$

where the non-dimensionalized quantities (i.e. those with tildes) are expected to be  $O(1)$ . In this Chapter, we discuss the dynamical regimes of the model in various limits for the  $\text{Da}_i$ .

## 6.1 The One-Dimensional BTL Regime

In the *bulk-transport-limited (BTL)* regime, the Damköhler numbers are large. If  $\tilde{J}_i = O(1)$  and  $\text{Da}_i \gg 1$ , then we must have  $\tilde{R}_i \ll 1$ . In the BTL limit  $\text{Da}_i \rightarrow \infty$ , the reaction rates must be identically 0. A more physically intuitive argument is that if the reactions are infinitely fast, then they must equilibrate infinitely quickly. Still another way to understand this regime is by studying it as a perturbation expansion in  $\text{Da}_i^{-1}$ , in which case the zeroth-order system is just  $\tilde{R}_i = 0$ . Regardless, if we view the system at the long (diffusive) time scale, the zeroth-order solution for the boundaries is complete and instantaneous equilibrium.

In any thermodynamically-consistent model for the boundary reactions,  $R_i = 0$  must correspond to an equality between the chemical potentials of the reactants and those of the products in the reaction [41]. At the bulk-diffusive time scale, then, the BTL limit of the CHR system may be simulated by replacing the reaction-flux boundary condition (6.1e) with a boundary condition equating chemical potentials across the crystal-electrolyte interface.

We therefore see that the BTL limit of the CHR equations is just a Cahn-Hilliard sys-

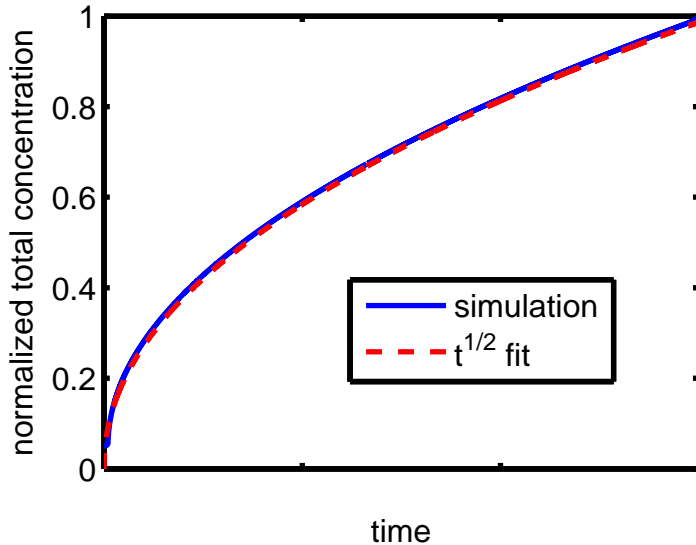


Figure 6-1: Normalized total concentration of an ion channel being filled via BTL dynamics.

tem with a fixed-chemical-potential boundary condition. The dynamics of the system are governed by how quickly the boundary chemical potential can be diffused across the bulk—which obviously must occur at the bulk-diffusive time scale. This is analogous to a standard diffusion problem in which the concentrations at the boundaries are held fixed.

Two additional points are worth noting. First, even though we have replaced the reaction boundary condition, there is still (in general) a net flux of intercalant across the crystal-electrolyte interface. In the BTL limit, however, these transfers occur instantaneously as needed to maintain the chemical-potential boundary condition. Second, in phase-separating systems, the boundary between high- and low-concentration phases in the bulk will move diffusively.

Figure 6-1 shows a plot of the total concentration of a long ion channel being filled via BTL dynamics. For most of the simulation, the total concentration scales like the square root of time (the actual exponent computed using a two-parameter, least-squares fit on a log-log plot was  $\approx 0.477$ ). Phase separation was achieved early in the simulation, and did not disappear until near the end; throughout the phase-separated period, the interphase boundary moved with a velocity that scaled like the inverse square root of time. This is all *diffusive* behavior.

## 6.2 The One-Dimensional SRL Regime

In the *surface-reaction-limited (SRL)* regime, the Damköhler numbers are small. If  $\tilde{R}_i = O(1)$  and  $\text{Da}_i \ll 1$ , then we must have  $\tilde{J}_i \ll 1$ . In the SRL limit  $\text{Da}_i \rightarrow 0$ , we must have  $\tilde{J}_i = 0$ . A more physically intuitive argument is that if the bulk diffusivities are infinitely

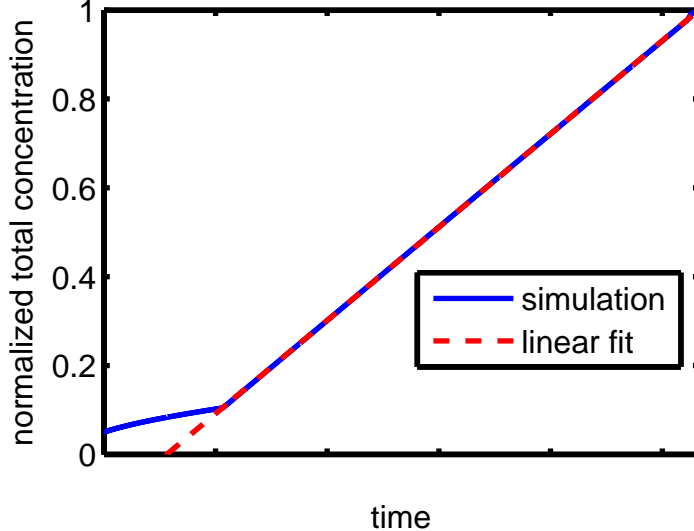


Figure 6-2: Normalized total concentration of an ion channel being filled via SRL dynamics.

small, then the bulk must equilibrate infinitely quickly. Still another way to understand this regime is by studying it as a perturbation expansion in  $\text{Da}_i$ , in which case the zeroth-order system is just a Cahn-Hilliard system with no-flux conditions at the boundary. Regardless, if we view the system at the long (reaction) time scale, the zeroth-order solution for the bulk is complete and instantaneous relaxation.

The SRL regime was described in [90] as follows:

In this regime, bulk transport is fast enough [to] equilibrate the concentration to a nearly constant value  $c(t)$  across the material, which varies uniformly at the slowest reaction time scale.

However, this is not correct: as discussed in § 2.3.2, bulk relaxation implies uniformity of *chemical potential*, but for phase-separating systems this involves rather extreme *non-uniformities* in *concentration*. In a phase-separating system, bulk equilibrium (or at least bulk metastability) occurs for spatially-uniform concentration fields only when the overall concentration is outside of the spinodal range. Indeed, inside the spinodal range, uniform concentrations are not only non-equilibrium points, but are actually linearly unstable.

Figure 6-2 shows a plot of the total concentration of a long ion channel being filled via SRL dynamics. Once phase separation was achieved (near the spinodal at total concentration  $\approx 0.11$ ), the total concentration scales linearly with time. Moreover, throughout this period, the interphase boundary moved with almost constant velocity. A more careful treatment of (6.1e) reveals that this velocity scales like  $(\rho_s/\rho)/\tau_i^R$  (so it does not depend on  $\lambda_i$ ).

We have therefore reached a very important conclusion: In a phase-separating system, the interphase boundary will always move from the particle boundaries into the bulk at the slowest time scale. In the BTL limit, the interphase boundary must diffuse away from the

particle boundaries; in the SRL limit, the interphase boundary must be pushed away from the particle boundaries via the reactions. We cannot conclude that there is any uniformity in the concentration fields in any regime.

### 6.3 “The SRL Equation”

In [90], an equation was derived for the dynamics of LiFePO<sub>4</sub> assuming extreme anisotropy in the SRL limit. In particular, it was claimed that if  $Da_x, Da_z \gg 1 \gg Da_y$ , then the concentration fields along the  $y$ -oriented channels would be uniform, so depth-averaging should lead to the (non-dimensional) equation

$$\frac{\partial \bar{c}}{\partial \tilde{t}} = \tilde{R} \quad (6.3)$$

where  $\bar{c}$  is the depth-averaged concentration field. Note that  $\tilde{R}$  here represents only the reactions occurring at the  $xz$ -faces.

There are multiple problems with this equation. Most importantly, the depth-averaging operation is not valid in general. Mathematically, the authors interchanged the order of the linear depth-averaging operation and the highly nonlinear operator  $\tilde{R}$ , which is rarely justifiable. In this case, it could only be valid if the concentration field were indeed uniform in the  $y$ -direction. However, as pointed out in § 2.3.2 and § 6.2, this is not true for phase-separating systems (like LiFePO<sub>4</sub>) over most of the concentration range. Indeed, the SRL regime only implies concentration uniformity outside of the miscibility gap; in particular, we can only claim that the concentration remains uniform along these channels *at all times* if the channels are so short that there is no spinodal or miscibility gap (see Chapter 8 or [13]).

Another problem with the derivation of this PDE in [90] is the claim that the Damköhler numbers in the  $x$ - and  $z$ -directions are important. What is actually used in deriving the equation, however, is that

$$\tau_y^D \ll \tau_y^R \ll \tau_{x,z}^{D,R}$$

i.e. that diffusion in the  $y$ -direction is the fastest time scale in the problem, and diffusion and reaction time scales for the  $x$ - and  $z$ -directions are very slow relative to the  $y$ -reactions. It is therefore mixed Damköhler numbers which are relevant.

Finally, a major problem with the *use* of (6.3) (rather than with its derivation) in [90] is that the original 4<sup>th</sup>-order equation has become a 2<sup>nd</sup>-order equation, but there is no discussion of boundary conditions. Indeed, given the assumptions of the paper that  $Da_x$  and  $Da_z$  are large, we should use the variational boundary condition (6.1d) and the fixed-chemical-potential boundary condition discussed in §6.1. However, this would allow an influx of intercalant at the  $xy$ - and  $yz$ -planes, which is clearly not what was intended in [90].

We provide here a detailed derivation of the “depth-averaged” equation used in [90], along with a careful list of the assumptions needed for its validity. Define the depth-averaged

concentration field

$$\bar{c}(x, z, t) \equiv \frac{1}{L_y} \int_0^{L_y} c(x, y', z, t) dy' . \quad (6.4)$$

We wish to find a simplified version of the full CHR model in terms of this new variable.

### 6.3.1 Evolution equation

Clearly  $\bar{c}(x, z, t)$  is the average concentration along the line  $\{(x', y', z') \in V \mid x' = x, z' = z\}$  at time  $t$ . Denote by  $\mathcal{T}_\epsilon(x, z)$  the closed, rectangular parallelepiped of width  $\epsilon$  centered on this line, i.e.

$$\mathcal{T}_\epsilon(x, z) \equiv \{(x', y', z') \in V \mid |x' - x| \leq \epsilon/2, |z' - z| \leq \epsilon/2\} .$$

The integral form of the conservation law (6.1c) with this “tube” as a control volume is

$$\frac{d}{dt} \int_{\mathcal{T}_\epsilon(x, z)} \rho c(x', y', z', t) dV = - \oint_{\partial \mathcal{T}_\epsilon(x, z)} \hat{\mathbf{n}} \cdot \mathbf{J}(x', y', z', t) dA .$$

The surface integral above has six components: the  $x$ - and  $z$ -directed bulk fluxes through the four sides of the tube, and the reaction fluxes through the top and bottom. Consider first the  $x$ -directed bulk fluxes. If we denote the  $x$ -component of the flux vector by  $J_x$ , then the total  $x$ -directed contribution to the surface integral may be estimated as follows:

$$\begin{aligned} & - \int_0^{L_y} \int_{z-\epsilon/2}^{z+\epsilon/2} J_x(x + \frac{\epsilon}{2}, y', z', t) dz' dy' + \int_0^{L_y} \int_{z-\epsilon/2}^{z+\epsilon/2} J_x(x - \frac{\epsilon}{2}, y', z', t) dz' dy' \\ & \approx -\epsilon \int_0^{L_y} \int_{z-\epsilon/2}^{z+\epsilon/2} \frac{\partial}{\partial x} J_x(x, y', z', t) dz' dy' \\ & \approx -\epsilon^2 \int_0^{L_y} \frac{\partial}{\partial x} J_x(x, y', z, t) dy' \\ & = \epsilon^2 \rho D_x \int_0^{L_y} \frac{\partial}{\partial x} \left( c \frac{\partial(\mu/k_B T)}{\partial x} \right) dy' . \end{aligned}$$

The fields  $c(\mathbf{x}, t)$  and  $\mu(\mathbf{x}, t)/k_B T$  are both  $O(1)$  quantities that vary in the  $x$ -direction over length scales comparable to  $\lambda_x$ . The absolute value of the  $x$ -component of the surface integral will therefore have order of magnitude  $\epsilon^2 \rho D_x L_y / \lambda_x^2$ . The exact same argument can be made for the  $z$ -component of the surface integral, whose order of magnitude is evidently  $\epsilon^2 \rho D_z L_y / \lambda_z^2$ .

The  $y$ -component of the surface integral consists entirely of the boundary reactions at the top and bottom of the particle. If  $R_y$  is a typical reaction rate over the top and bottom squares of the tube (i.e.  $\mathcal{T}_\epsilon(x, z) \cap \partial V$ ), then the  $y$ -component of the surface integral is approximately  $2\epsilon^2 \rho_s R_y$ .

We will assume that the reaction rates dominate this surface integral. More precisely, we

make the following

$$\text{Assumption 1 (1D transport): } \frac{D_x}{\lambda_x^2} \ll \left( \frac{\rho_s}{\rho L_y} \right) R_y \quad \text{and} \quad \frac{D_z}{\lambda_z^2} \ll \left( \frac{\rho_s}{\rho L_y} \right) R_y .$$

Then the bulk fluxes through the sides of the tube are negligible, and we are left only with the reaction fluxes through the top and bottom.

We have already used the approximations

$$\begin{aligned} & - \int_{x-\epsilon/2}^{x+\epsilon/2} \int_{z-\epsilon/2}^{z+\epsilon/2} \hat{\mathbf{n}} \cdot \mathbf{J}(x', y=0, z', t) dz' dx' \approx \epsilon^2 \rho_s R(x, y=0, z, t) \\ & - \int_{x-\epsilon/2}^{x+\epsilon/2} \int_{z-\epsilon/2}^{z+\epsilon/2} \hat{\mathbf{n}} \cdot \mathbf{J}(x', y=L_y, z', t) dz' dx' \approx \epsilon^2 \rho_s R(x, y=L_y, z, t) \end{aligned}$$

where we have used the shorthand notation  $R(\mathbf{x}, t)$  to mean  $R(\mathbf{x}, c(\mathbf{x}, t), \mu(\mathbf{x}, t))$ . We may also make the similar approximation

$$\int_{T_\epsilon(x,z)} c(x', y', z', t) dV \approx \epsilon^2 L_y \cdot \bar{c}(x, z, t) .$$

By canceling the common factor of  $\epsilon^2$  and then taking the limit as  $\epsilon \rightarrow 0$ , we get the evolution equation

$$\frac{\partial \bar{c}(x, z, t)}{\partial t} = \frac{\rho_s}{\rho L_y} \left[ R(x, y=0, z, t) + R(x, y=L_y, z, t) \right] . \quad (6.5)$$

Note that these reaction rates are still functions of  $c$  rather than of  $\bar{c}$ , so we do not yet have a closed PDE for the depth-averaged concentration.

### 6.3.2 Concentration field uniformity

In order to understand the bulk concentration field, we must non-dimensionalize the original CHR equations using time scales appropriate for filling an entire ion channel. It is clear from (6.5) that the natural time scale for the evolution of  $\bar{c}$  is  $T^R \equiv (\rho L_y / \rho_s) R_y^{-1}$ , where  $R_y$  is a typical value for  $R$  along the  $y = 0$  and  $y = L_y$  boundaries of  $V$ . We non-dimensionalize all lengths by  $L_y$ , and define the diffusive time scale  $T^D \equiv L_y^2 / D_y$  and the ion channel Damköhler number  $\text{Da} \equiv T^D / T^R$ . Then the  $y$ -component of the flux equation (6.1b) may be written

$$\text{Da} \cdot \tilde{J}_y = -\tilde{\rho} c \frac{\partial \tilde{\mu}}{\partial \tilde{y}}$$

where tildes denote non-dimensionalized quantities.

We now make the assumption used in [90] that we are in the surface-reaction-limited regime:

$$\text{Assumption 2 (SRL): } \text{Da} \ll 1$$

(note that this is different from the SRL regime discussed in § 6.2). If we examine the non-dimensional flux equation in the asymptotic limit  $\text{Da} \rightarrow 0$  (which is essentially just the “long-time” limit for diffusion in the  $y$ -direction), we see that  $\partial\tilde{\mu}/\partial\tilde{y} = 0$ . Note that this does not immediately imply that  $\partial c/\partial y = 0$  because in a phase-separating material a non-uniform concentration field can have a uniform chemical potential. Moreover, we cannot make any equilibrium arguments here because  $\tilde{\mu}$  may still vary as a function of  $x$  and  $z$ .

By (6.1a),

$$\frac{\partial\tilde{\mu}}{\partial\tilde{y}} = \tilde{g}_{\text{hom}}''(c) \frac{\partial c}{\partial\tilde{y}} - \tilde{\lambda}_x^2 \frac{\partial^3 c}{\partial\tilde{x}^2\partial\tilde{y}} - \tilde{\lambda}_y^2 \frac{\partial^3 c}{\partial\tilde{y}^3} - \tilde{\lambda}_z^2 \frac{\partial^3 c}{\partial\tilde{z}^2\partial\tilde{y}}.$$

We have seen that this entire expression must be 0 in the SRL regime, so we may write

$$\frac{\partial^3 c}{\partial\tilde{y}^3} = \frac{1}{\tilde{\lambda}_y^2} \left[ \tilde{g}_{\text{hom}}''(c) \frac{\partial c}{\partial\tilde{y}} - \tilde{\lambda}_x^2 \frac{\partial^3 c}{\partial\tilde{x}^2\partial\tilde{y}} - \tilde{\lambda}_z^2 \frac{\partial^3 c}{\partial\tilde{z}^2\partial\tilde{y}} \right].$$

Then if we make the “thin-slab” assumption

$$\textbf{Assumption 3 (thin-slab): } \tilde{\lambda}_y \gg 1$$

the above expression becomes simply  $\partial^3 c / \partial\tilde{y}^3 = 0$  in the asymptotic limit  $\tilde{\lambda}_y \rightarrow \infty$ .

We are therefore restricted to concentration fields whose  $y$ -dependence is at most quadratic. However, the variational boundary condition (6.1d) may be written  $\partial c / \partial y = 0$  at  $y = 0$  and  $y = L_y$ . The only quadratic functions that can satisfy these Neumann conditions at the boundaries are the constant functions. Given our assumptions, then,  $c$  can only be a function of  $x$ ,  $z$ , and  $t$ , and in fact  $\bar{c}(x, z, t) = c(x, y, z, t) \quad \forall y$ . All functions which depend on  $c$  can therefore be considered to be functions of  $\bar{c}$ . In particular, our evolution equation (6.5) is a closed equation for  $\bar{c}$  in the 1-dimensional transport, SRL, thin-slab regime. If the reaction rate does not depend explicitly on position, then this equation is simply

$$\frac{\partial\bar{c}(x, z, t)}{\partial t} = 2 \frac{\rho_s}{\rho L_y} R(\bar{c}(x, z, t), \bar{\mu}(x, z, t)) \quad (6.5')$$

where we have defined

$$\bar{\mu}(x, z, t) \equiv g'_{\text{hom}}(\bar{c}) - \lambda_x^2 \frac{\partial^2 \bar{c}}{\partial x^2} - \lambda_z^2 \frac{\partial^2 \bar{c}}{\partial z^2}.$$

It must be emphasized that, despite the fact that the miscibility and spinodal limits disappear for  $\lambda \approx L$  (see Chapter 8 or [13]), we could not have weakened the thin-slab assumption to  $\tilde{\lambda}_y \gtrsim 1$ . The miscibility gap is an equilibrium property, whereas we are specifically deriving non-equilibrium time-evolution equations. Moreover, the spinodal gap disappears in small 1-dimensional systems, but our concentration field is allowed to vary in  $x$  and  $z$ , and this variation may preserve phase-separation in the  $y$ -direction.

### 6.3.3 Boundary conditions

Equation 6.5' is a second-order PDE, and so must be closed with a pair of boundary conditions. By Assumption 1, there are no bulk fluxes in the  $x$ - or  $z$ -directions, so flux conditions are inappropriate. However, the variational boundary conditions (6.1d) still apply. Therefore, our PDE system has been simplified from a 4<sup>th</sup>-order equation with non-linear, 3<sup>rd</sup>-order boundary conditions to a 2<sup>nd</sup>-order equation with homogeneous Neumann boundary conditions.

### 6.3.4 Extension to systems with surface energies

The uniformity condition derived above for the concentration field would no longer be valid if we were to include a concentration-dependent surface energy density in the free energy functional. More specifically, suppose we were to add the surface term

$$G_{\text{surface}} = \oint_{\partial V} \gamma(\mathbf{x}, c) dA$$

to the bulk free energy. Then the variational boundary condition (2.11) would become

$$\hat{\mathbf{n}} \cdot (\mathbf{K} \nabla c) + \frac{\partial \gamma}{\partial c} = 0 . \quad (6.1d')$$

In general, this condition can only be satisfied by a concentration profile that is fully quadratic in  $y$ , and it may not be satisfiable at all (depending on the exact form of  $\partial \gamma / \partial c$ ). Equation 6.5' should therefore be considered the 1D-transport, SRL, thin-slab, no-surface-energy equation.

### 6.3.5 Relevance to LiFePO<sub>4</sub>

We have provided a formal derivation of a simplified CHR system, but we have yet to discuss its relevance to our material of interest. Unfortunately, many experimental procedures used to estimate physical parameters for battery systems are based on mathematical models which are not valid for phase-separating materials [90]. In particular, we are not aware of any estimates for the rate constant  $R_y$ . This is also noted by Srinivasan and Newman [92], who estimate an exchange current density by fitting experimental data to a mathematical model of an entire cell. Their model, however, has several shortcomings which we have already discussed. There are also analyses based on the Avrami-Johnson-Mehl-Eroofev equation which indicate that the reactions are rate-limiting [2], but the resulting parameters cannot be interpreted as reaction rate constants.

As we have defined it, the gradient penalty tensor is probably impossible to measure directly. However, we can estimate the individual  $\lambda_i$  as characteristic length scales for the interphase boundary widths. Thus, images as made by Richardson's group [21] allow us to estimate  $\lambda_x \approx 4 \text{ nm}$ . Though a phase boundary in the (101) direction has also been

seen [85], we are not aware of any images having been taken of flat interfaces perpendicular to the  $y$  or  $z$  axes. However, based on the “relative weakness of the bonding between the  $bc$  layers” [21], we may assume that  $\lambda_y$  and  $\lambda_z$  are both larger than  $\lambda_x$ .

The diffusion constants are also difficult to measure directly, especially for nano-particles. However, they can be estimated using ab initio techniques [74]. Such computations yield values of  $D_y \approx 10^{-8} \text{ cm}^2/\text{s}$ ,  $D_x \approx 10^{-19} \text{ cm}^2/\text{s}$ , and  $D_z \approx 10^{-45} \text{ cm}^2/\text{s}$ . Though other techniques can give quite different estimates for each of these parameters [55], there is wide agreement that the diffusion tensor is highly anisotropic, and that diffusion in LiFePO<sub>4</sub> is essentially one-dimensional.

Finally, the site densities are very well known through experiments and computations. Indeed, the unit cell of the crystal lattice and its dimensions are pictured very clearly in several different papers (see, for example, [72, 31]). Ignoring the relatively small changes in the lattice parameters between LiFePO<sub>4</sub> and FePO<sub>4</sub>, we may approximate the volume of a unit cell as  $290 \text{ \AA}^3$ ; since there are 4 lithium ions per unit cell,  $\rho \approx 0.014 \text{ \AA}^{-3}$ . Similarly, the area of the  $ac$  face of the unit cell is about  $49 \text{ \AA}^2$ , and there are a total of 2 exposed ions at the surface per unit cell, so  $\rho_s \approx 0.041 \text{ \AA}^{-2}$ .

Satisfying the first two assumptions requires bounding the reactive time scale:

$$\frac{L_y^2}{D_y} \ll \left( \frac{\rho L_y}{\rho_s} \right) R_y^{-1} \ll \min \left( \frac{\lambda_x^2}{D_x}, \frac{\lambda_z^2}{D_z} \right).$$

If we use a typical crystal depth of  $L_y \approx 50 \text{ nm}$  and if we make the estimate that  $\lambda_y$  and  $\lambda_z$  are approximately equal to  $\lambda_x$ , then we require

$$3 \times 10^{-3} \text{ sec}^{-1} \ll T^R \ll 2 \times 10^6 \text{ sec}^{-1}.$$

Since  $T^R$  is a characteristic time for filling an ion channel with lithium, and since we know that batteries using LiFePO<sub>4</sub> can be discharged at rates as fast as 400C [57], it seems reasonable to assume that these bounds are satisfied.

The thin slab assumption, however, is probably impossible to justify. Though we have not seen experimental evidence of a phase boundary in the  $y$ -direction, this is not proof that one never forms or that it must be very thick. Indeed, this is only evidence that such phase boundaries are not as energetically favorable as those in the  $x$ -direction, and that the particles have enough time to equilibrate before being examined in an electron microscope. Given that the gradient penalty tensor is defined as a tensorial extension of the nearest-neighbor energetic interactions,  $\lambda_y$  is probably confined to being at the nano-scale, so  $\lambda_y \gg L_y$  is unlikely to be experimentally feasible.

It is worth noting, however, that elastic effects do induce long-range interactions; if we think of  $\lambda_y$  as a parameter which somehow approximates these effects, it may indeed be larger than a few nanometers. Moreover, recent work on elastic effects in LiFePO<sub>4</sub> in particular have shown that the phase boundary tends to align in  $yz$  planes, both at equilibrium and during spinodal decomposition [93]. Dynamic simulations of the full CH equations which also include elastic effects would certainly still show some curvature of the phase boundary

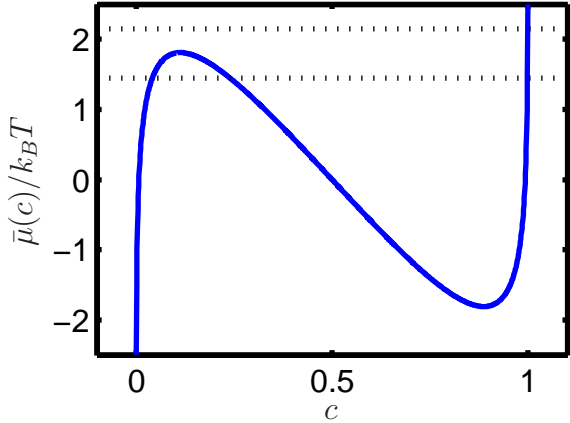


Figure 6-3: A plot of  $\bar{\mu}$  as a function of  $c$ . The lower line is at a chemical potential  $\mu_{\text{lower}} < \mu_{\text{max}}$  such that there are three different concentrations satisfying  $\bar{\mu}(c) = \mu_{\text{lower}}$ . The upper line is at a chemical potential  $\mu_{\text{upper}} > \mu_{\text{max}}$ , so there is only one concentration satisfying  $\bar{\mu}(c) = \mu_{\text{upper}}$ .

in the  $y$ -direction. However, it might be the case that this curvature is not very important, and that the tendency for the system to keep this boundary fairly straight might justify the use of the depth-averaged equation as a significant simplification of the full PDE system.

### 6.3.6 Wave propagation

As argued mathematically in [90], the depth-averaged equation admits wave solutions. In this section, we provide a more physical description of this phenomenon. We must first examine the homogeneous chemical potential

$$\bar{\mu}(c) \equiv a(1 - 2c) + k_B T \log \left( \frac{c}{1 - c} \right)$$

in more detail (see Fig. 6-3). There is some chemical potential  $\mu_{\text{max}}$  above which there is only one concentration  $c$  such that  $\bar{\mu}(c) = \mu$  but below which there are three such concentrations. Further, in the three-solution range, the two solutions near 0 and 1 are extremely insensitive to changes in chemical potential because of the logarithmic singularities at the endpoints.

Now suppose we have a concentration field  $c(x)$  that exhibits a phase change but which is at equilibrium with the electrolyte. Consider an instantaneous increase in the electrochemical potential of the external lithium ions and electrons, but suppose it is still inside the three-solution range. The concentration fields in the pure phases of the crystal will quickly equilibrate because, as noted above, concentrations near 0 and 1 are insensitive to changes in chemical potential. However, the interphase boundary cannot equilibrate as quickly, so will remain at a lower chemical potential than the electrolyte. This chemical potential difference drives insertion reactions at the interphase boundary, which will then cause the boundary

to spread (see Fig. 6-4). A more rigorous analysis [90] shows that, in fact, this spreading will occur at a constant velocity, i.e. that the depth-averaged equation admits non-linear wave solutions. Thus, the “active region” of the crystal in which significant lithium insertion occurs is concentrated along the thin interphase boundary, and the crystal can only fill with lithium via the motion of this boundary.

We see a similar spreading of the interphase boundary even if the change in chemical potential increases  $\mu_{\text{ext}}$  beyond  $\mu_{\text{max}}$  (see Fig. 6-5). However, the initial lithium-poor phase (in which  $c \approx 0$ ) can no longer quickly equilibrate with the electrolyte because there is now only one solution to  $\bar{\mu}(c) = \mu_{\text{ext}}$ , and it is very close to  $c = 1$ . Thus, in addition to the spreading wave, lithium is also being inserted into regions far away from the interphase boundary. In particular, then, the active region for lithium insertion is now the entire crystal face. Moreover, the reactions in these regions will actually accelerate through most of the filling process because  $\bar{\mu}(c)$  is a decreasing function of  $c$  over much of its range. The particle will therefore tend to fill much more quickly when the external electrochemical potential is increased beyond  $\mu_{\text{max}}$ .

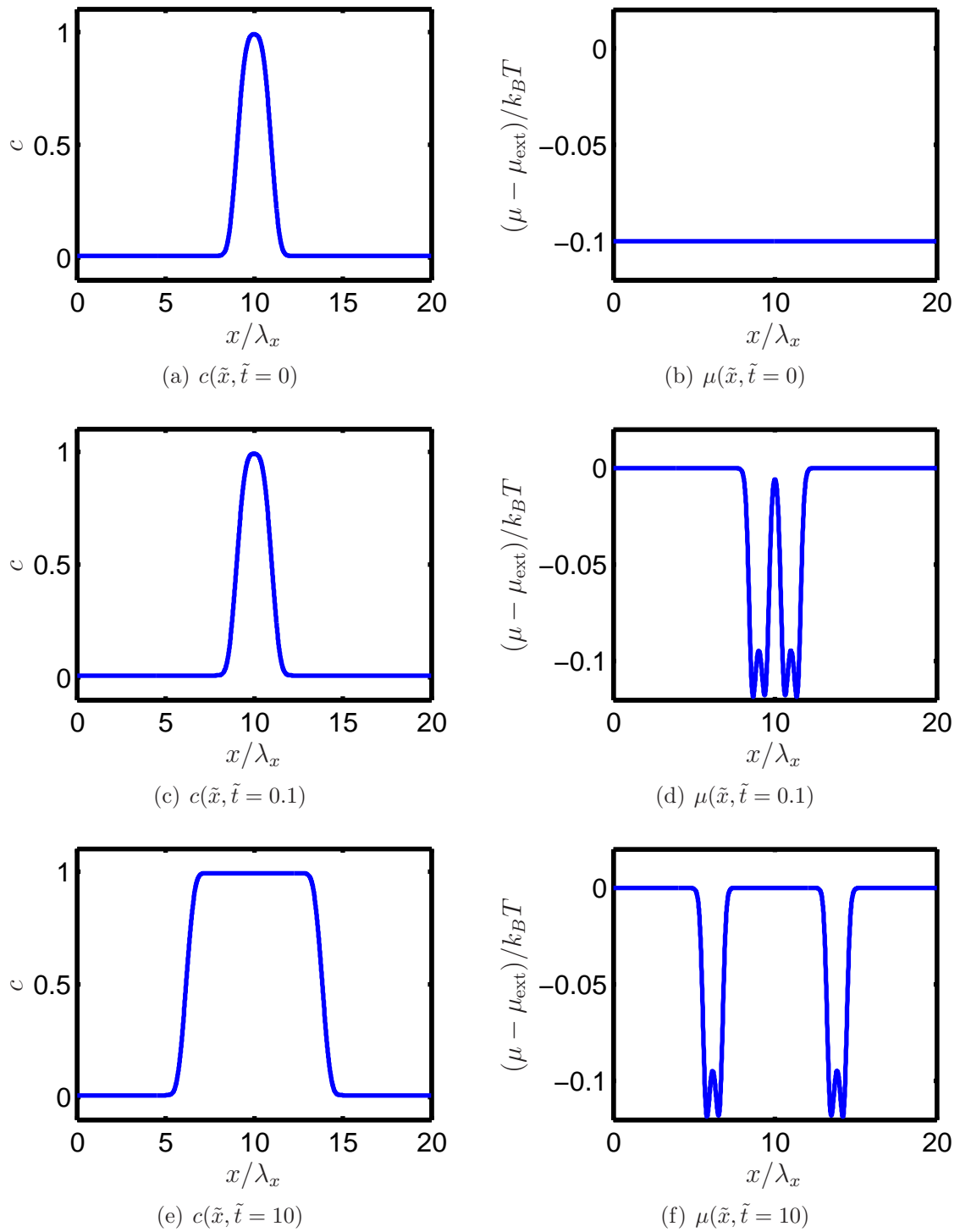


Figure 6-4: Response of the depth-averaged system to a sudden increase in  $\mu_{\text{ext}}$  of  $0.1k_B T$ . By  $\tilde{t} = 0.2$ , the waves are moving with constant velocities.

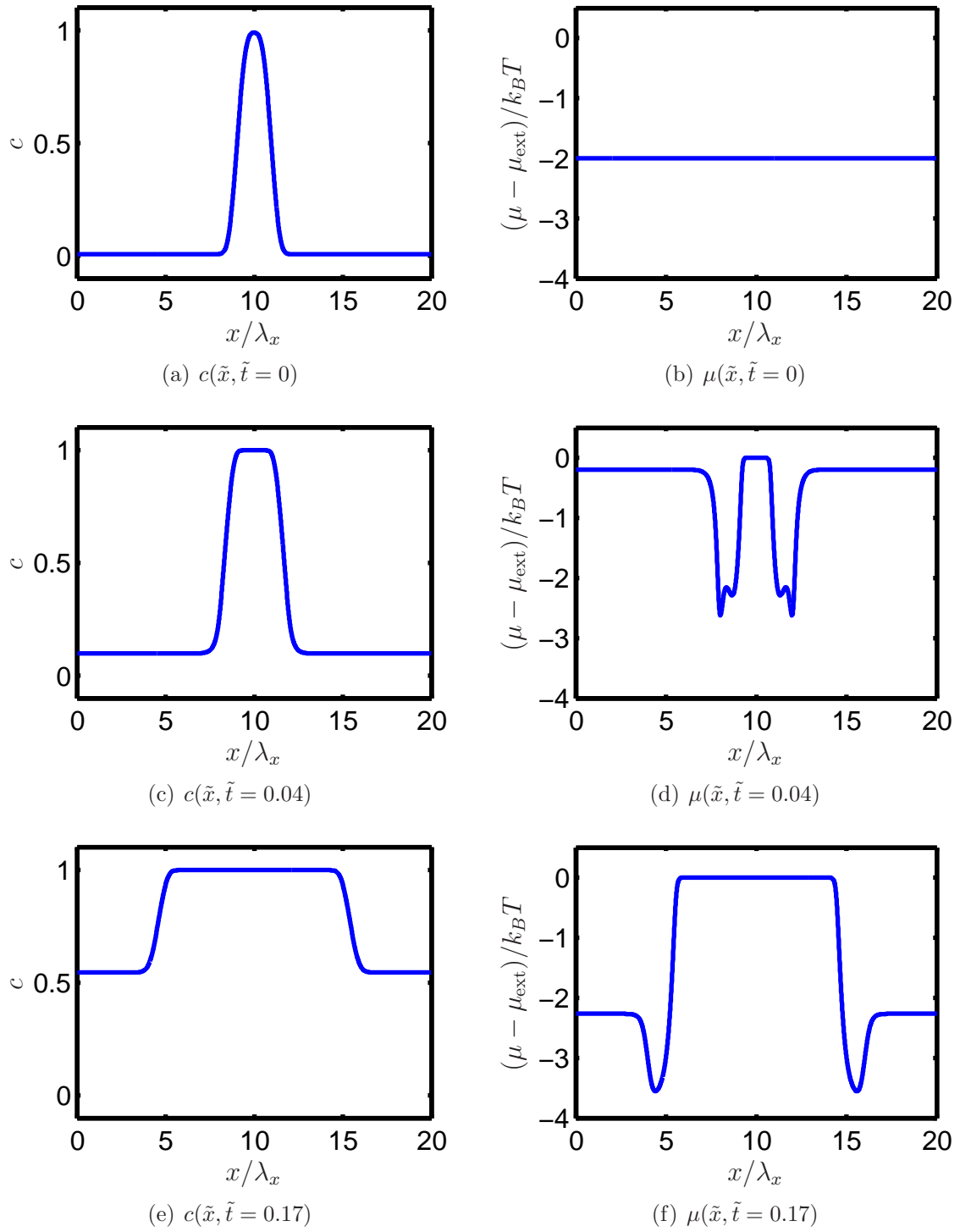


Figure 6-5: Response of the depth-averaged system to a sudden increase in  $\mu_{\text{ext}}$  of  $2k_B T$ . By  $\tilde{t} = 0.2$ , the particle is completely filled.

# Part II

## Applications

THIS PAGE INTENTIONALLY LEFT BLANK

# Chapter 7

## Defects in LiFePO<sub>4</sub>

In Chapters 2 and 3, we developed an elaborate continuum model that could be applied to the intercalation dynamics in an electrode consisting of phase-separating crystals of active material dispersed throughout some electrolyte. At the atomic scale, however, the lithium ions are simply executing a random walk through some energy landscape. One can imagine various impediments to such random walks: substances which cannot host lithium ions may block their paths through the electrolyte; surface contaminants may prevent entry into the active material; or crystal defects may leave large, immobile atoms in lithium vacancies inside the active material. As long as these obstacles are geometrically small and spatially isolated from one another, they will tend not to dramatically impact three-dimensional random walks [53]. Intuitively, lithium ions can always just “go around” them.

LiFePO<sub>4</sub> is an unusual material for which the general claims above do not necessarily hold. Inside these crystals, lithium ions are essentially confined to one-dimensional channels [74, 78], so even a single point defect can prevent diffusive progress. At a larger scale, the material is phase-separating [83], so there are energetic barriers against lithium ions straying into delithiated regions. Moreover, the interphase boundary tends to be flat [21]; a surface contaminant which blocks ion channels will force the moving boundary to bend around them, which is energetically expensive. In this Chapter, we will see how even small, rare defects can have macroscopic consequences for the equilibrium properties and kinetics of LiFePO<sub>4</sub>.

### 7.1 Maximum Charge Capacity

We begin by quantifying how individual point defects (i.e., lithium vacancies which cannot be occupied or diffused across by lithium ions) can impact the overall capacity of a crystal to store charge. As discussed above, LiFePO<sub>4</sub> crystals are essentially large groups of one-dimensional ion channels across which lithium diffusion is extremely rare. Therefore, even just two point defects in a single channel will block all of the vacancies in between, reducing the capacity by much more than just two lithium ions.

Consider a single ion channel with  $N \gg 1$  sites, numbered from 1 to  $N$ . Suppose that there are  $D$  defective sites,  $\{d_1, d_2, \dots, d_D\} \subseteq \{1, 2, \dots, N\}$ , in which no ions can be stored

and through which no flux can pass. In a one-sided channel, ions are only allowed to enter from below (so the outside of the crystal can be considered “site 0”). The one-sided capacity  $C_1$  of the channel is then simply

$$C_1 = \frac{1}{N} (\min\{d_1, d_2, \dots, d_D\} - 1)$$

where we must define  $\min\emptyset = N + 1$ . In a two-sided crystal, ions are allowed to enter from below (“site 0”) or above (“site  $N + 1$ ”), so the two-sided capacity is

$$C_2 = 1 - \frac{1}{N} (\max\{d_1, d_2, \dots, d_D\} - \min\{d_1, d_2, \dots, d_D\} + 1)$$

where we must define  $\max\emptyset = N$ .

We first suppose that the defects form during the creation of the crystal. Each vacancy is assumed to be defective with probability  $p \ll 1$ , independent of the state of any other vacancies. We may then assume that the total number of defects  $D$  is a Poisson random variable with parameter  $\lambda = Np$  [40]. Its probability density function is then

$$\mathbb{P}(D = d) = e^{-\lambda} \frac{\lambda^d}{d!}. \quad (7.1)$$

### 7.1.1 One-sided capacity

We take the large- $N$  limit from the beginning, and so model the channel as the continuum  $[0, 1]$ . Then for any  $x$  in this closed interval, we may write

$$\mathbb{P}(C_1 < x) = \sum_{d=0}^{\infty} \mathbb{P}(D = d) \mathbb{P}(\text{at least one defect occurs below } x \mid D = d).$$

The defects can arise anywhere in the channel, obeying only a uniform probability distribution therein. The probability that a single defect occurs in such a way as to leave the channel with a capacity of at least  $x$  is then  $1 - x$ . Since the defect locations are completely independent, we see that

$$\mathbb{P}(\text{at least one defect occurs below } x \mid D = d) = 1 - (1 - x)^d.$$

Substituting this and the Poisson density (7.1) into the above then yields

$$\mathbb{P}(C_1 < x) = e^{-\lambda} \sum_{d=0}^{\infty} \frac{\lambda^d}{d!} - e^{-\lambda} \sum_{d=0}^{\infty} \frac{[\lambda(1-x)]^d}{d!}.$$

These sums are easily computed using the Taylor series for  $e^z$  to get

$$\mathbb{P}(C_1 < x) = 1 - e^{-\lambda x}. \quad (7.2a)$$

We know that the channel is at full capacity if and only if no defects have formed, so

$$\mathbb{P}(C_1 = 1) = e^{-\lambda} . \quad (7.2b)$$

Thus we have a “truncated” exponential distribution (in the sense that it is an exponential distribution with all of the  $x \geq 1$  probability mass concentrated at  $x = 1$ ). This is as expected since  $C_1$  is essentially just the “waiting time” for the first occurrence of a Poisson process [40].

Combining the above yields the expectation and variance

$$\mathbb{E}(C_1) = \frac{1 - e^{-\lambda}}{\lambda} \quad (7.2c)$$

$$\text{Var}(C_1) = \frac{1 - 2\lambda e^{-\lambda} - e^{-2\lambda}}{\lambda^2} . \quad (7.2d)$$

Higher moments or cumulants can, of course, also be computed in closed form given the probability distribution (7.2). Note that in the “rare-defect” limit  $\lambda \ll 1$ , we have

$$\mathbb{E}(C_1) \sim 1 - \frac{1}{2}\lambda \quad \text{and}$$

$$\text{Var}(C_1) \sim \frac{1}{3}\lambda .$$

In the “common-defect” limit  $\lambda \gg 1$ , we have

$$\mathbb{E}(C_1) \sim \frac{1}{\lambda} \quad \text{and}$$

$$\text{Var}(C_1) \sim \frac{1}{\lambda^2} .$$

The latter is intuitively clear since, by uniformity, we expect the capacity of a one-sided,  $D$ -defect channel to be about  $1/D$ .

### 7.1.2 Two-sided capacity

In the case of two-sided channels, the probability distribution for the capacity given a fixed number of defects is no longer intuitively obvious, and instead must be calculated. Given that there are exactly  $d > 2$  defects, then  $C_2 < x$  if and only if the maximum distance between any two defects is  $< 1 - x$ . There are  $d(d - 1)$  ways to choose one defect to be closest to 0 and a second defect to be closest to 1, and then all other defects must lie in

between. Therefore

$$\begin{aligned}\frac{1}{d(d-1)} \mathbb{P}(C_2 < x \mid D = d) &= \int_0^x dx_1 \int_{1-x+x_1}^1 dx_2 \int_{x_1}^{x_2} dx_3 \cdots \int_{x_1}^{x_2} dx_d \\ &= \int_0^x dx_1 \int_{1-x+x_1}^1 dx_2 (x_2 - x_1)^{d-2}\end{aligned}$$

This integral is elementary, and may be simplified to

$$\mathbb{P}(C_2 < x \mid D = d) = 1 - (1 - x)^d - dx(1 - x)^{d-1}.$$

Note that for any  $x \in [0, 1]$ , this evaluates to 0 for  $d = 0$  or  $d = 1$ , as expected.

Now summing over all  $d$  using the Poisson distribution (7.1) for  $D$  gives us

$$\mathbb{P}(C_2 < x) = e^{-\lambda} \sum_{d=0}^{\infty} \frac{\lambda^d}{d!} - e^{-\lambda} \sum_{d=0}^{\infty} \frac{[\lambda(1-x)]^d}{d!} - e^{-\lambda} \lambda x \sum_{d=0}^{\infty} d \frac{[\lambda(1-x)]^{d-1}}{d!}.$$

Again, each of these sums may be computed in closed form using the Taylor series for  $e^z$ , yielding the final result

$$\mathbb{P}(C_2 < x) = 1 - e^{-\lambda x} - \lambda x e^{-\lambda x}. \quad (7.3a)$$

We know that two-sided channels are at full capacity if and only if there are fewer than 2 defects, so

$$\mathbb{P}(C_2 = 1) = (1 + \lambda)e^{-\lambda}. \quad (7.3b)$$

Combining the above yields the expectation and variance

$$\mathbb{E}(C_2) = \frac{2 - (2 + \lambda)e^{-\lambda}}{\lambda} \quad (7.3c)$$

$$\text{Var}(C_2) = \frac{2 + (2 - 2\lambda - 2\lambda^2)e^{-\lambda} - (2 + \lambda)^2 e^{-2\lambda}}{\lambda^2}. \quad (7.3d)$$

In the “rare-defect” limit  $\lambda \ll 1$ , we have

$$\begin{aligned}\mathbb{E}(C_2) &\sim 1 - \frac{1}{6}\lambda^2 \\ \text{Var}(C_2) &\sim \frac{1}{12}\lambda^2.\end{aligned}$$

In the “common-defect” limit  $\lambda \gg 1$ , we have

$$\begin{aligned}\mathbb{E}(C_2) &\sim \frac{2}{\lambda} \\ \text{Var}(C_2) &\sim \frac{2}{\lambda^2}.\end{aligned}$$

Note that in the former case, the dependence on  $\lambda$  is quadratic rather than linear as with the one-sided channels. In the latter case, the capacity is asymptotically equal to twice that of the comparable one-sided channel; again, this should be intuitively clear.

### 7.1.3 Defect formation energy

In the computations above, the Poisson parameter  $\lambda$  was taken to equal the product of the number  $N$  of lithium sites per channel and the probability  $p$  that an individual site is defective. We know that lithium sites are spaced about 3 Å apart [83], so  $N$  is simply one third the height of the channel in Angstroms. The probability  $p$ , however, is more difficult to estimate (though it might be measurable experimentally [106]).

From statistical mechanics, we know that if there is some well-defined energy barrier  $E$  for defect formation, then  $p = e^{-E/k_B T}$ . This temperature  $T$  would correspond to the high temperatures at which the LiFePO<sub>4</sub> is produced; once cooled to room temperature, the defects would be “frozen in place” as the energy barrier for correcting the defect would be too large to surmount at low temperatures. Thus, given  $E$  (which might be estimated from ab initio computations) and  $T$ , we could predict the available capacity of LiFePO<sub>4</sub> using the expectation values computed above.

Alternatively, if the available capacity is known experimentally, then the defect activation energy may be estimated by reversing the above computation. Table 7.1 is reproduced from [43] (with several errors corrected), and an additional column has been added listing the estimated energy barriers for defect formation. Note that the results range over almost 300 meV, reflecting the widely varying production methods and measurement techniques. However, none of the values is implausible as an atomic-level energy barrier (for example, they are all in the range of diffusional energy barriers computed for LiFePO<sub>4</sub> [74]).

## 7.2 Charge Capacity Fade

Crystal defects can, of course, arise after the high-temperature synthesis of the particle. Indeed, for LiFePO<sub>4</sub> in particular, each charge and discharge cycle during cell use induces large elastic stresses [102, 72] due to the differing lattice parameters between the lithiated and delithiated phases. We can therefore imagine that each charge/discharge cycle could potentially induce new point defects in the crystal structure.

One way to model this is to assume that every lithium vacancy has some small probability  $p_c$  of becoming defective during a single charge/discharge cycle, independent of the state of nearby sites and of previous cycles. Then we get a Poisson process with parameter  $\lambda_c = N p_c$  for each cycle. It is easily verified that the sum of independent Poisson random variables is itself a Poisson random variable whose parameter is equal to the sum of the individual Poisson parameters. Then if we call  $\lambda_f$  the Poisson parameter for defect formation during the crystal formation, we see that the number of defects per channel after  $m$  charge/discharge cycles is just a Poisson random variable with parameter  $\lambda = \lambda_f + m\lambda_c$ . We can then use all of the results derived in § 7.1. In particular, the asymptotic results derived above predict a

Reference	Typical channel height (nm)	Highest measured specific capacity (mAh/g)	Maximum preparation temperature (°C)	Estimated defect formation energy (meV)
[60]	20	166 (0.94C)	335	266
[89]	50	165 (3C)	650	467
[27]	140	145 (C/2)	500	394
[88]	200	141 (C/10)	700	517
[107] <sup>a</sup>				
[101]	500	151 (C/15)	600	554
[32] <sup>a</sup>				
[61]	77	148 (C/30)	600	406
[69] <sup>b</sup>				

<sup>a</sup> no temperature given

<sup>b</sup> particles intentionally doped with Zn

Table 7.1: Estimated energy barriers for defect formation in LiFePO<sub>4</sub> given several different production methods. Each capacity is listed along with the rate at which it was measured; since the low-end voltage also varied between 2 and 3 V, these results are difficult to compare. Note that the theoretical maximum specific capacity of LiFePO<sub>4</sub> is 170 mAh/g, as is easily computed.

long-time capacity decay that behaves like  $1/m$ . In other words, we get a very slow power law which decays as one-over-time.

If instead new defects can only form in the unblocked portion of the channel, then the analysis becomes more complicated. The Poisson parameter is then a function of the current state of the channel (since every new defect decreases the number  $N$  of accessible sites), and closed-form probability distributions are impossible to compute. However, we can say heuristically that each new defect in a one-sided channel will decrease the capacity by about half. This decrease is less in a two-sided channel, but the decay is still geometric. We should therefore expect that the long-time behavior of the charge capacity is an exponential decrease with the number of cycles.

A still more sophisticated model might include three time scales: one for the formation of new, spatially isolated defects (nucleation); another for the formation of new defects near existing ones (growth); and a third for the disappearance or relaxation of existing defects. The latter is likely to be negligible until the defect density is very high. Therefore, we would still see the above-mentioned decays of capacity. However, we would now also get a linear decay on the second time scale.

In principle, the parameters for such a model could be estimated from experimental capacity fade data. For example, Huang et al. have measured a very slow linear decay over 800 cycles [51]. However, there are many potential mechanisms for capacity fade [6, 91, 99], several of which could conceivably yield the same time-dependence as our model.

Moreover, some preparation methods yield material which fades very quickly [102], in which case our mechanism would be insignificant. It is therefore likely that macroscopic, whole-cell experiments would have to be supplemented with more detailed, microscopic studies of individual crystals in order to validate our hypothesized fade mechanism.

## 7.3 Wave-Defect Interactions

So far, we have dealt only with static properties of our material. When studying intercalation dynamics, however, it is also natural to ask how the motion of the interphase boundary might be disrupted by imperfections in the crystal or in its interface with the electrolyte. We still focus on localized defects, which we define to mean any physical change in the system which slows or prevents the filling of a small group of one-dimensional ion channels. For instance: surface impurities could completely block lithium transport into or out of several nearby channels; iron atoms might occupy some fraction of the lithium sites, thus reducing the capacity of a channel; imperfect bonding to an electronically-conductive phase in the electrolyte might dramatically slow intercalation; or impurities might locally change the lithium intercalation potential.

From a dynamical point of view, the exact mechanism leading to localized defects is unimportant. When a phase boundary approaches such a defect, it obviously must bend around it in order to proceed. However, this bending is energetically costly. In the CHR model (2.26), this is quantified by the gradient penalty  $\mathbf{K}$ : not only does the bend introduce new gradients, but it makes the phase boundary—along which there are already sharp gradients—longer. This will slow the progression of the phase boundary until the defect has been passed, thus reducing the lithium flux that the crystal can support.

The problem becomes even more pronounced when  $\mathbf{K}$  is highly anisotropic since such systems would more heavily penalize an increase in the phase boundary. Moreover, in such cases the wave-defect interaction becomes non-local in the sense that a defect comparable in size to the smallest  $\lambda_i$  will affect the wave out to a distance comparable to the largest  $\lambda_i$ . For LiFePO<sub>4</sub>, in which  $\lambda_z$  might be large and  $\lambda_x$  is a few nanometers [90], this means that an atomic-scale defect can impact the phase-transformation dynamics over the entire crystal.

These ideas are illustrated in Figures 7-1 and 7-2 using the thin-slab approximation (see § 6.3); defects are modeled as channels whose total content cannot change. First, note that the waves in the anisotropic crystal are much flatter than those in the isotropic one, as they should be. More significantly, by the second time step, the waves have made the most forward progress in the perfect crystal and the least forward progress in the anisotropic, defective crystal. This is reflected in Figure 7-2 by a sharp reduction in current while the wave interacts with the defect. To make the impact of the defect in our anisotropic case more quantitative, a 2% reduction in the lithium capacity *in this part of the crystal* has created up to a 50% drop in the lithium flux *over the entire crystal*.

Note that at late times, a “hole” is left in the concentration field around the defects with approximate dimensions of  $\lambda_x \times \lambda_z$  (in fact, using the results of § 2.5.1, one can prove that the hole is an ellipse whose axis lengths scale like  $\lambda_x$  and  $\lambda_z$ ). These can cause a crystal to

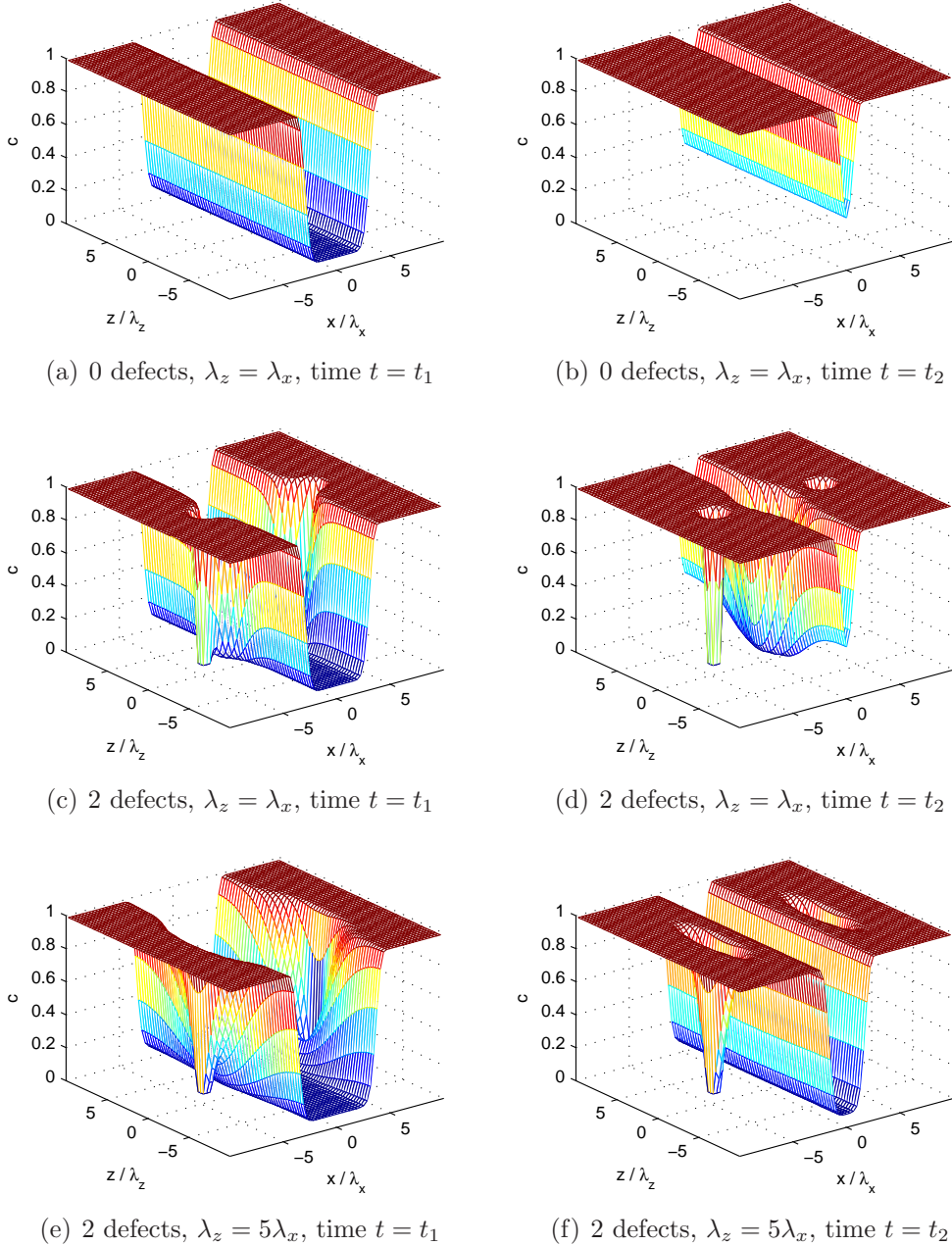


Figure 7-1: Thin-slab simulations of lithiation waves interacting with crystal defects. The top row shows results for a perfect (i.e. defect-free) crystal; the middle row shows results for a crystal with two defects and an isotropic gradient penalty tensor (so  $\lambda_z = \lambda_x$ ); and the third row shows results for a crystal with the same two defects as in the second case, but with an anisotropic  $\mathbf{K}$  ( $\lambda_z = 5\lambda_x$ ). All cases are identically nucleated by two flat, incoming waves, and are pictured at the same two time steps.

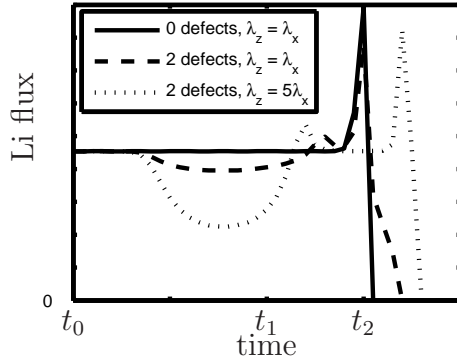


Figure 7-2: The instantaneous lithium flux for the three simulations plotted in Fig. 7-1.

suffer an even more dramatic performance degradation if there are several nearby defects. Because of the gradient penalty term, the lithiation waves are stable to small-wavelength perturbations. Thus if two defects are sufficiently close, the wave cannot “squeeze through” the gap between their respective holes, and they effectively become one long defect. An array of defects with period  $\lambda_z$  can therefore block a wave entirely, preventing the other side of the crystal from being lithiated until a new wave is nucleated.

## 7.4 Conclusion

We have performed a simple analysis of the impact that even atomic-scale defects can have on the charge capacity of LiFePO<sub>4</sub>. More significantly, we have shown that our CHR model predicts a new failure mechanism for LiFePO<sub>4</sub>: because the phase-transformation waves resist bending, they can be slowed down (or even stopped altogether) by defects in the crystal or in the nearby electrolyte. Thus even small drops in the overall lithium capacity of a crystal can lead to large reductions in the power capacity. This is a result which cannot have been predicted by the shrinking core model, and once fully explored could impact the design and development of new battery systems.

THIS PAGE INTENTIONALLY LEFT BLANK

# Chapter 8

## Size-Dependent Spinodal and Miscibility Gaps

Intercalation phenomena occur in many chemical and biological systems, such as graphite intercalation compounds [34], DNA molecules [86], solid-oxide fuel cell electrolytes [79], and Li-ion battery electrodes [52]. The intercalation of a chemical species in a host compound involves the nonlinear coupling of surface insertion/extraction reaction kinetics with bulk transport phenomena. It can therefore occur by fundamentally different mechanisms in nano-particles and molecules compared to macroscopic materials due to the large surface-to-volume ratio. Intercalation dynamics can also be further complicated by phase separation kinetics within the host material. This poses a challenge for theorists, since phase transformation models have mainly been developed for periodic or infinite systems in isolation [8], rather than nano-particles driven out of equilibrium by surface reactions.

In this Chapter, we ask the basic question, “Is nano different?”, for intercalation phenomena in phase-separating materials. Our analysis is based on a general mathematical model for intercalation dynamics recently proposed by Singh, Ceder, and Bazant (SCB) [90]. The SCB model is based on the classical Cahn-Hilliard equation [16] with a novel boundary condition for insertion/extraction kinetics based on local chemical potential differences, including concentration-gradient contributions. For strongly anisotropic nano-crystals, the SCB model predicts a new mode of intercalation dynamics via reaction-limited nonlinear waves that propagate along the active surface, filling the host crystal layer by layer. Here, we apply the model to the thermodynamics of nano-particle intercalation and analyze the size dependence of the miscibility gap (metastable uniform compositions) and the spinodal region (linearly unstable uniform compositions) of the phase diagram.

Our work is motivated by Li-ion battery technology, which increasingly involves phase-separating nanoparticles in reversible electrodes. The best known example is LiFePO<sub>4</sub>, a promising high-rate cathode material [83] that exhibits strong bulk phase separation [83, 4, 21]. Experiments have shown that using very fine nano-particles (< 100 nm) can improve power density [105, 51] and (with surface modifications) achieve “ultrafast” discharging of a significant portion of the theoretical capacity [57]. Experiments also provide compelling evidence [21, 63, 29, 85] for the layer-by-layer intercalation waves (or “domino cascade” [29])

predicted by the SCB theory [90, 14], in contrast to traditional assumption of diffusion limitation in battery modeling [33, 92].

There is also experimental evidence that the equilibrium thermodynamics of LiFePO<sub>4</sub> is different in nano-particles. Recently, Meethong et al. have observed that, as the crystal size decreases, the miscibility gap between the lithium-rich and lithium-poor phases in the material shrinks significantly [73] (i.e. the tendency for phase separation is reduced). A suggested explanation is that smaller particles experience relatively larger surface effects, which has been supported by calculations with an elaborate phase-field model [94], although without accounting for surface reaction kinetics. However, it has also been seen experimentally that carbon coating can reduce the surface effects and prevent the surface-induced reduction of the miscibility gap [108].

We will show that the SCB model suffices to predict that the spinodal and miscibility gaps both decrease as the particle size decreases. The analysis reveals two fundamental mechanisms: (i) nano-confinement of the inter-phase boundary, and (ii) stabilization of the concentration gradients near the surface by insertion/extraction reactions. These effects are independent of surface energy models, and indeed are valid for any phase-separating intercalation system.

## 8.1 Model

We employ the general SCB model for intercalation dynamics—based on the Cahn-Hilliard equation with chemical-potential-dependent surface reactions—with any simplifying assumptions [90]. In particular, we do not specialize to surface-reaction-limited or bulk-transport-limited regimes or perform any depth averaging for strongly anisotropic crystals [90, 14]. Our field of interest is  $c(\mathbf{x}, t)$ , the local concentration of the intercalated diffusing species (e.g., Li in LiFePO<sub>4</sub>). Let  $\rho$  be the density of intercalation sites per unit volume in the system (e.g., occupied by Li ions or vacancies), assumed to be constant and independent of position and local concentration. We take  $c$  to be normalized by  $\rho$ , so it is non-dimensional and only takes values between 0 and 1 (e.g., in the local compound Li<sub>c</sub>FePO<sub>4</sub>).

We assume that the free energy of mixing in our model system is well-approximated by the Cahn-Hilliard functional [18, 16, 8]

$$G_{\text{mix}}[c] = \int_V \left[ g_{\text{hom}}(c) + \frac{1}{2} (\nabla c)^T \mathbf{K} (\nabla c) \right] \rho dV . \quad (8.1)$$

The function  $g_{\text{hom}}(c)$  is the free energy per molecule of a homogeneous system of uniform concentration  $c$ , which is non-convex in systems exhibiting phase separation. The gradient penalty tensor  $\mathbf{K}$  is assumed to be a constant independent of  $\mathbf{x}$  and  $c$ . Then the diffusional chemical potential (in energy per molecule) is the variational derivative of  $G_{\text{mix}}$ ,

$$\mu(\mathbf{x}, t) = \frac{\partial g_{\text{hom}}(c)}{\partial c} - \nabla \cdot (\mathbf{K} \nabla c) . \quad (8.2)$$

The mass flux (in molecules per unit area per unit time) is given by the linear constitutive relation [26]

$$\mathbf{J}(\mathbf{x}, t) = -\rho c \mathbf{B} \nabla \mu , \quad (8.3)$$

where  $\mathbf{B}$  is a mobility tensor. Finally, the dynamics are governed by the mass conservation equation

$$\frac{\partial(\rho c)}{\partial t} + \nabla \cdot \mathbf{J} = 0 . \quad (8.4)$$

For illustration purposes, we employ the regular solution model for the homogeneous free energy [84]:

$$g_{\text{hom}}(c) = ac(1 - c) + k_B T [c \log c + (1 - c) \log(1 - c)] . \quad (8.5)$$

The two terms give the enthalpy and entropy of mixing, respectively. When numerical values are needed, we will use  $a/k_B T = 5$ , which is in rough agreement at room temperature with measurements on LiFePO<sub>4</sub> [30]. Of course, other models are possible, but for the intercalation of a single species in a crystal with bounded compositions  $0 < c < 1$ , the homogeneous chemical potential  $\mu_{\text{hom}}(c) = g'_{\text{hom}}(c)$  must diverge in the limits  $c \rightarrow 0^+$  and  $c \rightarrow 1^-$  due to entropic contributions from particles and vacancies. (This constraint is violated, for example, by the quartic  $g_{\text{hom}}(c)$  from Landau's theory of phase transitions, suggested in a recent paper on LiFePO<sub>4</sub> [85] following SCB.)

Note that  $\mathbf{K}/k_B T$  has units of length-squared. Since it is assumed that  $\mathbf{K}$  is positive-definite, we may denote its eigenvalues by  $k_B T \lambda_i^2$  for real, positive lengths  $\lambda_i$ . In particular, when  $\mathbf{K}$  is diagonal, we define  $\lambda_i \equiv \sqrt{K_{ii}/k_B T}$ . When the system is phase-separated into high- $c$  and low- $c$  regions, these  $\lambda_i$  are the length scales for the interphasial widths in the different eigendirections [18, 8]. In LiFePO<sub>4</sub>, experimental evidence [21] suggests that one of these widths is about 8 nm (though the  $\lambda_i$  in the other two directions might be large—comparable to the particle size—as phase-separation in these directions is not believed to occur). These are therefore the natural length scales for measuring the size of phase-separating nano-crystals.

Our system of equations is closed by the following boundary conditions on the surface of the nano-particle:

$$\hat{\mathbf{n}} \cdot (\mathbf{K} \nabla c) = 0 \quad (8.6)$$

$$\hat{\mathbf{n}} \cdot \mathbf{J} = -\rho_s R \quad (8.7)$$

where  $\hat{\mathbf{n}}$  is an outward unit normal vector. Equation 8.6 is the so-called variational boundary condition, which is natural for systems without surface energies or surface diffusion and follows from continuity of the chemical potential at the surface. Equation 8.7 is a general flux condition enforcing mass conservation, where  $\rho_s$  is the surface density of intercalation sites, and  $R$  is the net local rate of intercalant influx (insertion) across the boundary. In the classical Cahn-Hilliard (CH) model, no mass flux across the boundary is allowed, and thus  $R = 0$ . For intercalation systems [90, 14], we allow for a non-zero reaction rate  $R$  depending on the local values of  $c$  and  $\mu$  and refer to this general set of equations as the Cahn-Hilliard-*with-reactions* (CHR) system.

For the current work (and indeed, for many of the conclusions reached by SCB [90]), the particular form of  $R$  is unimportant. According to statistical transition-state theory in a concentrated solution [10], the net insertion rate is given by the difference of insertion and extraction rates, each having Arrhenius dependence on an (excess) chemical potential barrier. In order to satisfy de Donder's equation [84], it must have the general form

$$R = R_{\text{ins}} \left[ 1 - \exp \left( \frac{\mu - \mu_e}{k_B T} \right) \right] \quad (8.8)$$

where  $R_{\text{ins}}$  is the rate for the insertion reaction. For thermodynamic consistency, this  $\mu$  must be the same as the diffusional chemical potential used in the bulk equations, and  $\mu_e$  is the external chemical potential of the intercalants in a reservoir phase outside of the particle (e.g.,  $\text{Li}^+$  in the electrolyte and  $e^-$  in the metallic current collector of a Li-ion battery electrode); note that we are again assuming that the particle surface is energetically identical to the bulk. If the reaction rates were controlled by electrostatic potential differences, for example, then  $R_{\text{ins}}$  could include transfer coefficients and the interfacial voltage drop, and the familiar Butler-Volmer model for charge-transfer reactions [11] would be recovered in the limit of a dilute solution. Following SCB [90], we do not make any dilute solution approximation and keep the full CH expression for  $\mu$  (8.2)—including the second derivative term—while assuming a uniform external environment at constant  $\mu_e$ . Although different models are possible for the chemical potential of the transition state [10], we make the simple approximation of a constant insertion rate  $R_{\text{ins}}$ , consistent with particles impinging on the surface at constant frequency from the external reservoir. In that case, the composition dependence of  $R$  enters only via the extraction rate.

## 8.2 The CH Miscibility Gap

Outside of the spinodal range, systems with uniform concentration fields are linearly stable. However, if there exists a phase-separated solution with the same overall amount of our material but with a lower free energy, then the uniform system will only be metastable. We will demonstrate that the miscibility range—the set of overall concentrations for which phase separation is energetically favorable—shrinks as the particle size decreases.

Unlike the spinodal, the miscibility gap cannot be studied analytically. Instead, we must solve our original set of equations (8.2–8.4) numerically, looking for phase-separated systems with lower free energies than the uniform system with the same overall concentration. We focus only on 1-dimensional systems, or equivalently 3-dimensional systems whose phase boundary is perpendicular to one of the eigendirections and whose concentration field is uniform in the other two directions. Note that there is experimental [21] and theoretical [29] evidence that this is an accurate picture for the concentration field in  $\text{LiFePO}_4$ . We will henceforth drop the subscripts on  $\lambda$ , and call  $L$  the length of the system.

We begin by fixing a single crystal size. For each value of the average concentration, we choose a corresponding initial condition, and we solve the Cahn-Hilliard equation (using

a semi-discrete finite volume method and the no-flux boundary condition). The system is stepped forward in time until the free energy reaches a minimum. The resulting free energies of mixing for three different crystal sizes and a range of average concentrations are plotted in Fig. 8-1(a). Note that the curves do not extend across the entire  $x$ -axis. This is because, for sufficiently extreme average concentrations, no initial conditions can be found which lead to a phase-separated steady state. This suggests that such states do not exist, or that if they do exist they are not local minimizers of  $G_{\text{mix}}$ . The phase-separated energy curves do extend slightly past the uniform curve, allowing us to estimate the endpoints of the miscibility gap. The results suggest that the miscibility gap shrinks as the crystal size decreases.

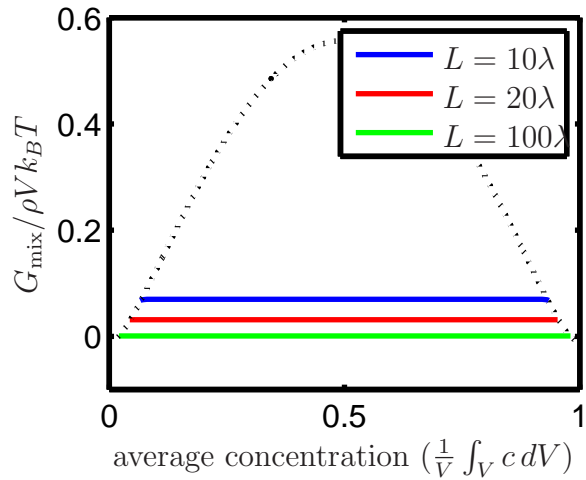
In order to validate this hypothesis, we performed a more exhaustive search for phase-separated, steady-state solutions near the apparent miscibility endpoints. This was done using the shooting method for boundary value problems to compute concentration fields satisfying (8.2) with  $\mu = \text{constant}$ . The resulting field that extremized the average concentration while still having a smaller free energy of mixing than the corresponding constant field was considered to be the boundary of the miscibility region. The calculated miscibility gap widths over a range of crystal sizes are plotted in Fig. 8-1(b); they clearly support a shrinking miscibility gap.

There is a simple physical explanation for this behavior. As discussed above, the interphase region will normally have a width on the order of  $\lambda$ . The average concentration can only be close to 0 or 1 if this interphase region is close to a system boundary. At this point, the average concentration can only become more extreme if the interphase region is compressed or disappears. If it disappears, then we are left with a uniform system, and the average concentration is outside of the miscibility gap. The other alternative, though, is expensive energetically due to the gradient penalty term in (8.1). Thus low-energy, phase-separated systems are limited geometrically to those concentrations in which the interphase region is (relatively) uncompressed between the crystal boundaries. As the crystal size decreases, the limits imposed on the average concentration by the incompressibility of the interphase region becomes more and more severe, and thus the miscibility gap must shrink.

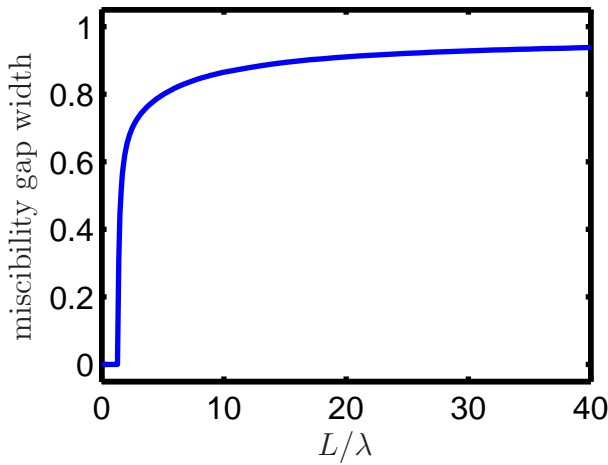
To date, there has not been a systematic experimental study of the size of the miscibility gap as a function of particle size. Meethong et al., for instance, only test three different particle sizes—34, 42, and 113 nm [73]. If we use the estimate  $\lambda \approx 8 \text{ nm}$  (this is the same value as was used in [94], and is compatible with the experimental measurement of the phase boundary width [22]), then these correspond to  $L$ 's of  $4.25\lambda$ ,  $5.25\lambda$ ,  $14.125\lambda$ . The measurements imply miscibility gaps of about 0.55, 0.70, and 0.95, respectively, whereas our model predicts gaps of 0.78, 0.80, and 0.89 for these particle sizes. Note, however, that surface coating seems to increase the miscibility gap to about 0.75 for particles as small as 30 nm [108], and our model predicts a gap of 0.76 for  $L = 3.75\lambda$ .

### 8.3 The CHR Spinodal Gap

The spinodal gap is the set of concentrations for which an initially-uniform system will spontaneously decompose through the exponential growth of infinitesimal fluctuations. Thus,



(a) Mixing energies of steady-state, phase-separated solutions.



(b) Width of the miscibility gap as a function of crystal size.

Figure 8-1: The free energies in the first plot are given per intercalation site so that they are comparable across different crystal sizes. The dotted line indicates the free energy of mixing per site for a uniform system of the given concentration.

perturbation theory is the relevant mathematical tool, and we look for solutions to the CHR system of the form

$$c(\mathbf{x}, t) = c_0 + \epsilon c_1(\mathbf{x}, t)$$

where  $c_0$  is a constant and  $\epsilon$  is a small parameter. If  $c_0$  is truly a static solution to the CHR equations, then by (8.8),  $\mu_e$  must equal  $\mu_0 = \partial g_{\text{hom}}(c_0)/\partial c$  at all points on the boundary of  $V$ . The first-order system derived by linearizing about  $c_0$  is then

$$\mu_1(\mathbf{x}, t) = \frac{\partial^2 g_{\text{hom}}(c_0)}{\partial c^2} c_1 - \nabla \cdot (\mathbf{K} \nabla c_1) \quad (8.9a)$$

$$\mathbf{J}_1(\mathbf{x}, t) = -\rho c_0 \mathbf{B} \nabla \mu_1 \quad (8.9b)$$

$$\frac{\partial(\rho c_1)}{\partial t} = -\nabla \cdot \mathbf{J}_1 \quad (8.9c)$$

with the boundary conditions

$$\hat{\mathbf{n}} \cdot (\mathbf{K} \nabla c_1) = 0 \quad (8.9d)$$

$$\hat{\mathbf{n}} \cdot \mathbf{J}_1 = \frac{\rho_s R_{\text{ins}}}{k_B T} \mu_1 . \quad (8.9e)$$

This is a fourth-order, linear system with constant coefficients. Note that the exact same set of equations would result even had we taken  $\mathbf{K}$  and  $\mathbf{B}$  to be functions of  $c$ ; the tensors above would only need to be replaced by the (still constant) values  $\mathbf{K}(c_0)$  and  $\mathbf{B}(c_0)$ .

If we have an infinite system with no boundaries, then the Fourier ansatz  $e^{i\mathbf{k} \cdot \mathbf{x}} e^{st}$  solves the above system if and only if it satisfies the dispersion relation

$$s = -c_0(\mathbf{k}^T \mathbf{B} \mathbf{k}) \left( \frac{\partial^2 g_{\text{hom}}(c_0)}{\partial c^2} + \mathbf{k}^T \mathbf{K} \mathbf{k} \right) . \quad (8.10)$$

Since  $\mathbf{B}$  and  $\mathbf{K}$  must be positive-semidefinite,  $s$  will be non-positive whenever  $\partial^2 g_{\text{hom}}(c_0)/\partial c^2 \geq 0$ . However, if  $\partial^2 g_{\text{hom}}(c_0)/\partial c^2 < 0$ , then the  $c_0$  will be unstable to long-wavelength perturbations. In particular, for the regular solution model (8.5), the criterion for linear stability becomes

$$-2 \frac{a}{k_B T} + \frac{1}{c_0(1 - c_0)} \geq 0 .$$

Thus a high enthalpy of mixing will promote instability of uniform systems with moderate concentrations.

If instead the system geometry is finite, then the boundary conditions will constrain the set of allowable wave vectors  $\mathbf{k}$ . We again focus on one-dimensional systems for simplicity. Then if the system occupies the line segment from 0 to  $L$ , the general solution of the perturbed equations for the CH system ( $R_{\text{ins}} = 0$ ) is a sum of terms of the form

$$c_1(x, t) = A \cos \left( \frac{n\pi}{L} x \right) e^{st}$$

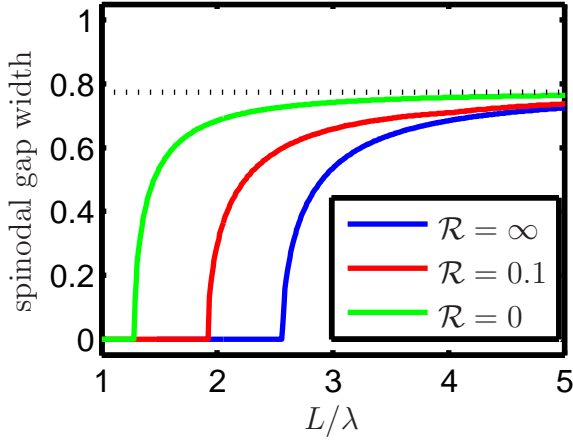


Figure 8-2: Width of the spinodal gap as a function of crystal size. The dotted line indicates the width of the spinodal region for an infinite system. The other three curves are given for different values of the non-dimensionalized reaction rate constant  $\mathcal{R} \equiv (\rho_s/\rho\lambda)(R_{\text{ins}}/(D/\lambda^2))$ , where  $D = Bk_B T$  is the diffusion constant in the bulk.

for any integer  $n$ . The dispersion relation (8.10) still holds, but the wave number must equal  $n\pi/L$  for integer values of  $n$  in order to satisfy the boundary conditions. In other words, we can no longer perturb the system with arbitrarily-long wavelengths. The stability criterion is  $\partial^2 g_{\text{hom}}(c_0)/\partial c^2 > -\pi^2\lambda^2/L^2$ .

For the regular solution model (8.5), the criterion for linear stability becomes

$$-2\frac{a}{k_B T} + \frac{1}{c_0(1-c_0)} > -\pi^2\lambda^2/L^2 .$$

The spinodal region is defined as the range  $(\alpha, 1 - \alpha)$  of unstable  $c_0$  values. It is easily verified that  $\alpha$  is a decreasing function of  $L$ , i.e. that *the spinodal range is more narrow for smaller crystals*. Moreover, for sufficiently small values of  $\lambda/L$ , the above inequality is satisfied for all values of  $c_0$ , in which case there is no spinodal region at all. These facts are demonstrated in Fig. 8-2. These results date back to Cahn's 1961 paper [16] and are known in the phase-field community. However, it seems that their relevance for nano-particle composites—as in Li-ion batteries—has not yet been appreciated.

Moving beyond classical bulk models, we will now show that non-zero boundary reactions can further reduce the spinodal gap width. Even the linear perturbed system of equations is no longer analytically tractable when  $R_{\text{ins}} \neq 0$ , and in particular, the wave numbers are no longer simply  $n\pi/L$ . According to the dispersion relation (8.10), every  $s$  is associated with four wave numbers, and in general it takes a linear combination of all four such functions to satisfy the boundary conditions. For any given  $L$ ,  $c_0$ , and  $s$ , we may compute the four corresponding wave numbers  $k_j$ , and then look for a set of coefficients  $A_j$  such that  $\sum_{j=1}^4 A_j e^{ik_j x} e^{st}$  solves the perturbed PDE and boundary conditions (8.9). Because the system is linear and homogeneous, this can be reduced to finding a solution to some matrix equation  $\mathbf{MA} = \mathbf{0}$ ,

which has solutions if and only if the determinant of the matrix  $\mathbf{M}$  is 0.

Therefore, for any given system size  $L$  and reaction rate constant  $R_{\text{ins}}$ , we must numerically solve for the range of concentrations  $c_0$  that admit solutions to the perturbed equations for at least one positive value of  $s$ . Results of such computations are shown in Fig. 8-2. Notice that increasing the reaction rate constant reduces the spinodal gap. Moreover, it was found numerically that increasing  $R_{\text{ins}}$  tends to reduce the growth rate constant  $s$ .

These effects cannot be explained solely in terms of chemical potential perturbations near the boundary. Instead, we must examine the nature of the allowable perturbations for different reaction rates. For large values of  $R_{\text{ins}}$ , any non-zero  $\mu_1$  at the boundaries causes large perturbations in the reaction fluxes by Eq. 8.9e. In order for  $J_1$  to be differentiable near the boundaries, we must also have large bulk fluxes nearby. In general, this would require large concentration gradients, or equivalently short-wavelength perturbations. But, as is clear from the dispersion relation (8.10), it is precisely the *short-wavelength* perturbations which are rendered stable by the gradient penalty term (see Ref. [49] for an interesting discussion of this point).

More mathematically, suppose  $\mu_1$  is non-zero at a boundary. Then by (8.9e),  $J_1$  must be non-zero there, which by (8.9b) implies that  $\mu_1$  must have a non-zero gradient. Combining these two terms with our ansatz for  $c_1$  yields the requirement

$$\left| c_0 \left( \frac{\rho}{\rho_s} \right) (k_B T B) k \right| \sim R_{\text{ins}} .$$

We therefore see that when  $\mu_1$  is non-zero at a boundary, the wave number scales linearly with the reaction rate constant. Again, large  $R_{\text{ins}}$  would require large  $k$ , which are increasingly stable.

As the reaction rate increases, then, unstable perturbations satisfying (8.9) must have  $\mu_1$  and  $\nabla \mu_1$  close to 0 near the boundaries. However, this requires long-wavelength perturbations, and we have already shown that these will become increasingly stable as the crystal size shrinks. Thus fast reaction rates will tend to stabilize small nano-particles.

Note, however, that for systems larger than about  $2.5\lambda$ , the spinodal gap does not disappear even for infinitely fast reactions. This implies that there must exist infinitesimal perturbations to a uniform system which lead to phase separation without ever changing the diffusional chemical potential at the boundaries of the system. This has been verified numerically by solving the full CHR system (8.2–8.8) in the limit  $R_{\text{ins}} \rightarrow \infty$ . However, by limiting the spinodal decomposition to only occur via this small class of perturbations, higher reaction rates reduce the decomposition growth rate and the spinodal gap width.

Though we have used a specific mathematical model to derive these results, the conclusions are generally valid. Regardless of the bulk model, a bounded system will only allow a discrete spectrum for its first-order perturbations. The smallest admissible wave numbers will scale like  $1/L$ , and the system will suffer linear instability for more narrow ranges of concentrations as the system size shrinks. Moreover, fast reaction rates at the boundaries require short wavelength perturbations, and such perturbations are energetically unfavorable when there is a diffuse interface between phases.

## 8.4 Other Effects

There are at least two important effects which we have excluded from our analysis. First, we have intentionally neglected surface energies in order to demonstrate that purely bulk effects and reaction rates can cause shrinking spinodal and miscibility gaps. However, surface energies could easily be accommodated. For example, if the free energy of the system were to include a concentration-dependent surface tension between the particle and its environment,

$$G_{\text{mix}} = G_{\text{mix,bulk}} + \int_{\partial V} \gamma(c) dA ,$$

then the variational boundary condition (8.6) would need to be replaced by

$$\hat{\mathbf{n}} \cdot (\mathbf{K} \nabla c) + \frac{1}{\rho} \frac{d\gamma}{dc} = 0 .$$

This would change the analysis, but would not significantly affect the conclusions.

Perhaps a more serious omission for LiFePO<sub>4</sub> in particular is elastic stress in the crystal due to lattice mismatches. However, it has been demonstrated [93] that these effects can frequently be accommodated by simply decreasing the enthalpy-of-mixing parameter  $a$ . Given our results above, elastic stress would therefore enhance the shrinking spinodal and miscibility gaps.

## 8.5 Conclusion

We have shown that intercalation phenomena in phase-separating materials can be strongly dependent on nano-particle size, even in the absence of contributions from surface energies and elastic strain. In particular, the miscibility gap and spinodal gap both decrease (and eventually disappear) as the particle size is decreased to the scale of the diffuse interphase thickness. Geometrical confinement enhances the relative cost of bulk composition gradients, and insertion/extraction reactions tend to stabilize the concentration gradients near the surface. These conclusions have relevance for high-rate Li-ion battery materials such as LiFePO<sub>4</sub>, but are in no way restricted to this class of materials.

# Chapter 9

## Inter-Particle Interactions

It has recently been discovered that, upon partial discharge of a rechargeable cell with a composite LiFePO<sub>4</sub> cathode, most of the individual particles of the active material are either completely lithiated or completely delithiated [29]. This inter-particle “mosaic model” runs counter to the intuitive picture that all particles should be in similar, partially-lithiated states. The authors of the above study conclude that since LiFePO<sub>4</sub> is a phase-separating material, the nucleation of the lithiated phase must be slow and the propagation of the inter-phase boundary must be fast. While this certainly could be true (and there is independent experimental evidence for such a conclusion [2]), it does not explain other studies which show that smaller particles tend to be the ones which are completely lithiated while larger particles remain unlithiated [19]. In fact, since nucleation is a stochastic event whose probability of occurrence is increased by larger volume (for homogeneous nucleation) or surface area (for heterogeneous nucleation), any justification for the mosaic model based on nucleation rates alone must favor the larger particles.

We first point out that there is a simple, energetic explanation for the mosaic model which is independent of nucleation rates. As cell discharge begins, all LiFePO<sub>4</sub> particles will be in similar states of delithiation. Whether by nucleation or spinodal decomposition, phase transition is the result of thermal fluctuations, and as such is inherently stochastic. Thus, this process will not occur simultaneously in different particles. Once a particular particle does undergo phase separation, however, it will immediately be in a lower-energy state (see Fig. 9-1). Consequently, it will be energetically favorable for lithium ions in the electrolyte to be inserted into the phase-separated particles. As the energy of insertion into the phase-separated particles will remain relatively constant (this can be understood, for instance, by noting the long voltage plateau seen experimentally [83]), this disparity will persist until phase separation is lost near the end of discharge for the lower-energy particle. Thus whichever particle phase-separates first will tend to intercalate more of the local lithium ions, greatly reducing the chances of phase-separation in nearby particles until the first fills up. We call this one-at-a-time behavior the “mosaic instability” (see Fig. 9-2).

This explanation can also be cast in terms of reaction rates. Suppose insertion into a phase-separated crystal is lower in free energy than insertion into a non-separated crystal by some amount  $\Delta G$ . Then if these reactions are governed by Arrhenius rate laws, insertion

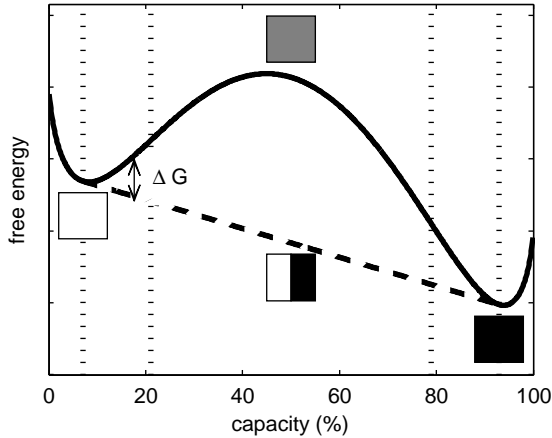


Figure 9-1: Generic free energy plot demonstrating the thermodynamics of phase separation. The outer pair of vertical lines marks the edge of the miscibility gap, the inner pair marks the spinodal gap, and the dashed line is the common tangent along which phase coexistence is energetically favorable. Phase separation occurs at some capacity inside the miscibility gap, and so is associated with a decrease  $\Delta G$  in free energy.

into the phase-separated crystal will tend to be faster by a factor of  $\exp(\Delta G/k_B T)$  (where  $k_B$  is the Boltzmann constant and  $T$  is the temperature). Thus even small energy changes upon phase-separation will result in exponentially faster reactions into that particle. Again, this will tend to strongly favor the filling of phase-separated particles before nucleation occurs in nearby particles.

Note that because of the exponentially faster reaction rates, the local lithium concentration in the electrolyte will quickly decrease. As long as the concentration was not too high to begin with, this will tend to increase the free energy of the lithium ions due to entropic effects. If this depletion is too severe, the free energy of the electrolytic lithium ions may drop to a level below that of the ions in the non-separated particles. At this point, the non-separated particles will not simply be intercalating ions more slowly, but rather will be (on average) de-intercalating ions. This would obviously dramatically enhance the mosaic instability.

In order to understand the experimentally-observed size-dependence of the mosaic effects [19], we must have a model for the phase transition. Suppose there is no nucleation, but rather that phase-separation occurs purely through spinodal decomposition. During the early stages of cell discharge, the lithium concentration inside a single particle is not quite uniform; it must be lower near the middle than near the boundaries due to diffusional transport limitations in the crystal. Such inhomogeneities will naturally be more extreme in larger particles. This disparity will then allow the smaller particles to reach the critical concentration necessary for spinodal decomposition earlier. In summary, small particles reach critical concentrations first, allowing them to phase-separate before larger particles, and thus to become more energetically-favorable targets for lithium insertions from the electrolyte.

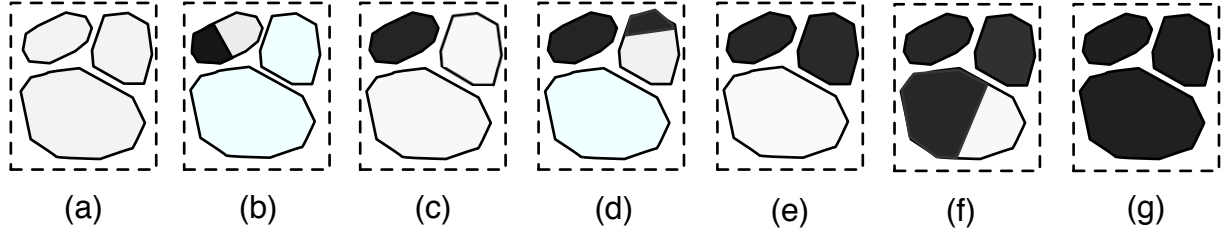


Figure 9-2: Schematic of the inter-particle mosaic instability.

## 9.1 Model

We will now briefly describe the mathematical model for intercalation dynamics introduced by Singh et al. [90] and demonstrate that it predicts the mosaic instability. Define  $\rho$  to be the Li site density (in molecules per unit volume) in the system, which we will take to be a constant independent of position and local concentration. Our field of interest is  $c(\mathbf{x}, t)$ , the local Li concentration normalized by  $\rho$  (so  $0 < c < 1$ ).

We assume that the free energy of mixing in our system is well-approximated by the Cahn-Hilliard functional [18]

$$G_{\text{mix}}[c] = \int_V \rho \left[ g_{\text{hom}}(c) + \frac{1}{2} (\nabla c)^T \mathbf{K} (\nabla c) \right] dV , \quad (9.1)$$

where  $g_{\text{hom}}(c)$  is the free energy per molecule of a homogeneous system of uniform concentration  $c$ . The gradient penalty tensor  $\mathbf{K}$  is assumed to be a constant independent of  $\mathbf{x}$  and  $c$ . Then the diffusional chemical potential (in energy per molecule) is the variational derivative of  $G_{\text{mix}}$ ,

$$\mu(\mathbf{x}, t) = \frac{\partial g_{\text{hom}}(c)}{\partial c} - \nabla \cdot (\mathbf{K} \nabla c) . \quad (9.2)$$

We assume that the flux (in molecules per unit area per unit time) is given by the linear constitutive relation [26]

$$\mathbf{J}(\mathbf{x}, t) = -\rho c \mathbf{B} \nabla \mu , \quad (9.3)$$

where  $\mathbf{B}$  is a mobility tensor. Finally, the dynamics are governed by the conservation equation

$$\frac{\partial(\rho c)}{\partial t} + \nabla \cdot \mathbf{J} = 0 . \quad (9.4)$$

Note that unlike previous work with this model [90, 14], we do not restrict ourselves to situations in which “depth-averaging” is appropriate.

We will only employ the regular solution model for the homogeneous free energy [84]:

$$g_{\text{hom}}(c) = ac(1 - c) + k_B T [c \log c + (1 - c) \log(1 - c)] . \quad (9.5)$$

The first term gives the enthalpy of mixing and the second term gives the entropy of mixing.

When numerical values are needed, we will use  $a/k_B T = 5$ , which is in rough agreement at room temperature with measurements on LiFePO<sub>4</sub> [30].

Our PDE is closed by the boundary conditions

$$\hat{\mathbf{n}} \cdot (\mathbf{K} \nabla c) = 0 \quad \text{and} \quad \hat{\mathbf{n}} \cdot \mathbf{J} = -\rho_s R , \quad (9.6)$$

where  $\hat{\mathbf{n}}$  is an outward unit normal vector. The first is the variational boundary condition, which is natural for systems without surface energies or surface diffusion. The second governs material exchange between the particle and its environment;  $\rho_s$  is the surface density of intercalation sites, and  $R$  is the local rate of Li influx across the boundary. For intercalation materials being charged and discharged, we will use an Arrhenius-type reaction condition to model the transfer of ions between the electrode particle and the electrolyte. For the current work (and indeed, for many of the conclusions reached in [90]), the exact form of  $R$  is unimportant. In order to satisfy de Donder's equation [84], it must be given by

$$R = R_{\text{ins}} \left[ 1 - \exp \left( \frac{\mu - \mu_e}{k_B T} \right) \right] \quad (9.7)$$

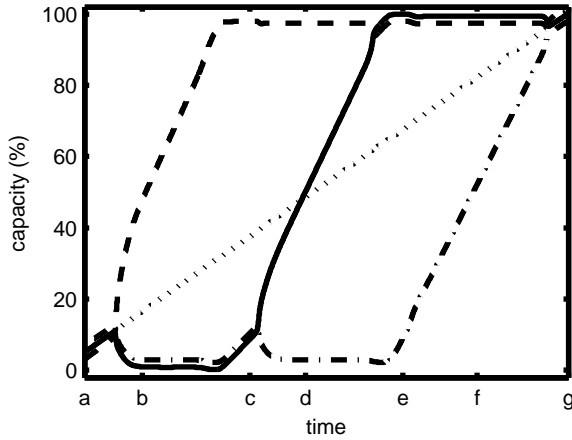
where  $R_{\text{ins}}$  is the rate for the insertion reaction,  $\mu$  is the diffusional chemical potential used in the bulk equations, and  $\mu_e$  is the chemical overpotential for the reactants outside of the particle; note that we are again assuming that the particle surface is energetically identical to the bulk. If the reaction rates were controlled by electrical potential differences, for example, then  $R_{\text{ins}}$  would include transfer coefficients and interfacial potential differences, and the resulting rate law would be of the Butler-Volmer form [9]. For simplicity, we take  $R_{\text{ins}}$  to be a constant.

## 9.2 Numerical Results

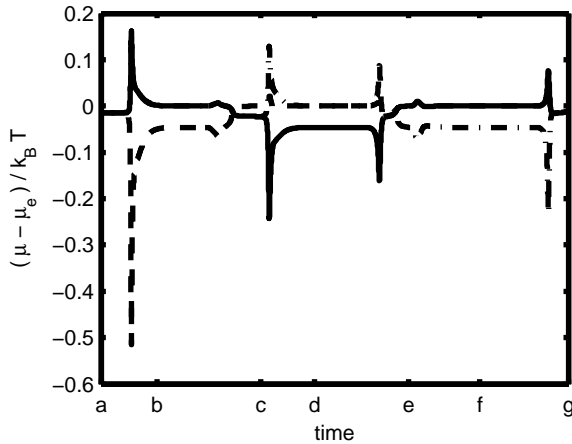
Before discussing solutions to the full set of equations above, we note that a maximum difference in the reaction rates can be easily computed. Indeed, linear stability analysis of the Cahn-Hilliard equation in an infinite crystal shows that spinodal decomposition will occur at concentrations  $c$  satisfying [16]

$$-2 \frac{a}{k_B T} + \frac{1}{c(1-c)} = 0 .$$

Thus, for  $c \approx 0.113$  (assuming  $a = 5k_B T$ ), we could conceivably have a phase-separated and a homogeneous particles with this same average concentration. The diffusional potential of the homogeneous particle can then be computed directly from Eq. 9.2, and would be  $\approx 1.81k_B T$ . The diffusional potential of the phase-separated particle, on the other hand, would be very close to 0. Hence the insertional energy difference would be  $\approx 1.81k_B T$ , making the reaction rate for the phase-separated particle more than 6 times faster than that of the homogeneous particle.



(a) capacity vs. time



(b) chemical potential vs. time

Figure 9-3: Simulation results for the constant-C-rate lithiation of a set of three nearby particles. The solid lines give the data for the particle of intermediate size; the dashed lines give the data for the particle which is 5% smaller; and the dash-dot lines give the data for the particle which is 5% larger. The dotted black line represents the overall capacity of the three particles in the first plot; note that the individual capacity curves have been artificially shifted in the vertical direction to make them easier to distinguish. The labels along the x-axis correspond to the states in Fig. 9-2.

Deriving more information from the model described above requires solutions to the Cahn-Hilliard-with-reactions system. This is a non-linear, 4<sup>th</sup>-order equation with non-linear, 3<sup>rd</sup>-order boundary conditions, so it must be solved numerically. We employ a semi-discrete Finite Volume Method (FVM), and use the implicit Crank-Nicolson method for the time-stepping. The equations are solved for multiple particles simultaneously in order to simulate the interactions described above. This model cannot accommodate nucleation, so all phase transitions occur via spinodal decomposition. Moreover, since lithium transport is essentially one-dimensional in LiFePO<sub>4</sub>[74], we limit ourselves to one-dimensional simulations.

The mosaic instability is an inter-particle interaction, but is limited to those which are sufficiently nearby one another to affect the lithium concentrations in their respective environments. We will therefore assume that the particles in any given simulation are so small and close together that the lithium in the electrolyte is at a uniform chemical potential ( $\mu_e$  in Eq. 9.7); this also allows us to avoid having to solve for ion transport in the electrolyte. However, to model either transport limitations in the electrolyte or constant-C-rate discharge of the cell, we adjust  $\mu_e$  at every time step to maintain a constant overall influx of lithium to the complete set of particles being simulated.

Figure 9-3 shows the results of a simulation using three particles of slightly different sizes. Figure 9-3(a) clearly demonstrates the mosaic instability, and moreover that smaller particles are almost completely lithiated before larger particles are more than about 10% filled. Examination of the time-dependent concentration fields shows that, as expected, each of the pictured events in which one particle begins to fill up at the expense of the others is associated with phase-separation in the first crystal. Further, the effect described above in which non-phase-separated particles actually lose lithium is evident after each new particle phase-separates. The energetic cause for the reaction disparity is evident from Fig. 9-3(b). The large negative spikes in chemical potential occur during phase-separation, and result from the extreme instability of the concentration field between near-homogeneity and complete phase separation.

Note that the number of particles was chosen only for ease of display. Every simulation we have performed with as many as eleven particles has demonstrated the same behavior. Moreover, this effect seems to be independent of the exact diffusion constants, reaction rates, and even reaction rate laws employed.

### 9.3 Discussion

First, it must be pointed out that the physical arguments made above are based purely on the active material being strongly phase-separating. Though we have used LiFePO<sub>4</sub> as our primary example, this is mainly because of the active research being done on this material. Our arguments and mathematical model should yield similar predictions for composite cathodes employing any other phase-separating material (e.g. LiMn<sub>2</sub>O<sub>4</sub> [80]).

Second, any mosaic instability is undesirable in a functioning battery because it causes increased polarization losses. Maintaining a fixed current requires much higher overpotentials when only a fraction of the cathode particles are “active” at any one time. Thus, building

a cell with monodisperse LiFePO<sub>4</sub> particles would limit the mosaic instability and minimize this class of voltage drops. This effect was noticeable in the numerical studies described above, but further work is necessary to understand the impact on a real system.

There are a few restrictions on our analysis. First, the discharge must be sufficiently slow for phase-separation in individual particles to be discrete events. Second, the particles must have the same set of neighbors throughout discharge. Third, the system must not be allowed to equilibrate; since the lowest-energy state at intermediate overall levels of charge is for all particles to be phase-separated, the mosaic state (Fig. 9-2) is only metastable and will not last indefinitely. These restrictions are certainly met by the discharge of a working cell, as in [29]. Some experiments which have not reproduced the mosaic behavior are performed under conditions which are dramatically different. For instance, Ramana et al. [85] use a strong chemical deintercalant; they actively stir an aqueous solution containing the LiFePO<sub>4</sub> particles; and they wait 24 hours before examining the material.

We also note that, though we do not disagree with the detailed analysis provided by Delmas et al. [29], the conclusion reached by the authors that nucleation is slow is not necessary given the presented experimental data. Indeed, even if nucleation were fast, we would still see the results of the mosaic instability since phase-separated particles would still tend to slow down nucleation in other nearby particles. Similarly, the mosaic instability might explain the slow *aggregate* nucleation rate inferred from experiments using the Avrami equation [2].

As discussed more fully in [90], experimental evidence renders the “shrinking-core” model for intercalation untenable from a purely dynamical point of view. What we have shown here makes an even stronger case. Indeed, even if a Fickian model could be concocted to mimic the curious behavior of the phase boundary in LiFePO<sub>4</sub>, it would still be insufficient to recreate the complex inter-particle behavior of the mosaic instability. This only arises because of the energy difference between homogeneous and phase-separated states, which is not present in simple diffusional models.

It is noted by Delmas et al. [29] that while the shrinking-core model does not accurately describe single-particle behavior, it should still be valid for conglomerates, i.e. as a good description for aggregate behavior over multiple nearby particles. However, if lithiation truly occurs one crystal at a time (locally) as we have argued, then shrinking core is probably invalid on any scale.

The most important implication of this work is to the mathematical analysis of entire cells which employ phase-separating materials. The most influential such model [33] and software [75] were developed by Newman’s group. An implicit assumption thereof is that the concentration fields among nearby particles is identical. This “mean-field” assumption is invalidated by the mosaic instability, and would remain invalid even if the shrinking-core model were replaced with a more physically-motivated diffusion equation as described by Singh et al. [90] and used above. Indeed, it would appear that the microscopic behavior of the active material would have to be described using some simplified model which accounts for mosaic effects.

THIS PAGE INTENTIONALLY LEFT BLANK

# Chapter 10

## Conclusion

This thesis has provided a very general and detailed study of the atomic kinetics in small (micron- or nanometer-scale), multiphase particles which interact chemically with their environment. In Part I, we discussed our approach to continuum modeling of such systems, and in Part II we made several theoretical predictions for their behavior. We must emphasize that, while the sophisticated mathematical model we have employed provides quantitative predictions, we have also given simple, physical arguments for most of our conclusions. Moreover, though we have used lithium-ion batteries as our primary example, none of our results are limited to these devices.

Though our results are general, their most important application is certainly to lithium-ion batteries, and in particular to those using LiFePO<sub>4</sub>-based cathodes. As we discussed in the introduction, porous electrode theory as usually employed in the battery community has many shortcomings when used with phase-separating materials. In particular, it does not model the energy barrier to, or time-scale for, phase separation; the energy of the interphase boundary once separation has occurred; or the effect that these energies have on the non-ideality of bulk diffusion or ion transfer reaction rates at the boundaries. In essence, porous electrode theory, when applied to phase-separating materials, ignores much of the physics at the smallest scale. It is precisely this weakness that we have hoped to overcome.

There are currently three major omissions from our work. First, we have neglected elasticity despite its known importance for LiFePO<sub>4</sub>. This was done for the sake of simplicity: including elastic effects would have greatly complicated an already-complicated mathematical model. However, as was discussed in Chapter 6, it is hoped that our model is capable of approximating the CHR-with-elasticity system.

Second, we have not completely understood the phase-separation process. Being based on the Cahn-Hilliard equation, our model is, by design, able to simulate spinodal decomposition. However, it cannot model nucleation, the process of overcoming the energy barrier to phase-separation outside of the spinodal gap. The size of the critical nucleus and the energy required for its formation could be estimated by solving the Cahn-Hilliard equation for unstable steady states. However, the time scale required for the stochastic formation of such a nucleus is more difficult to compute since, especially in materials like LiFePO<sub>4</sub>, there are almost certainly transport limitations to this process. Indeed, the one-dimensional transport

in LiFePO<sub>4</sub> may make homogeneous, bulk nucleation very slow, in which case it may be safely ignored. However, extending the methods of Chapter 5 to the insertion reactions may reveal that heterogeneous nucleation at the boundaries can be fast.

Third, in focusing on the physics at the particle level, we have not adequately connected our predictions to the macroscopic behavior of a composite cathode. For example, we have shown that defects can reduce the flux from individual particles, but we have not predicted the impact on the cell's total power that any given distribution of defects might have. Similarly, we have described the inter-particle mosaic instability, but much larger simulations would be required to understand the spatial extent of this interaction and to quantify its cost to the cell voltage.

Despite these failings, it is our hope that this work will serve as the foundation for new, necessarily simpler models for a composite cell. By starting with an accurate description of the physics at the lowest level and building up, perhaps we can create a new porous electrode theory capable of answering the questions above.

# **Part III**

# **Appendix**

THIS PAGE INTENTIONALLY LEFT BLANK

# Appendix A

## Source Code

I wrote over 11,000 lines of Matlab scripts while working on this thesis. Some of it was highly specialized (for example, searching for unsteady perturbations and low-energy, phase-separated solutions for Chapter 8). Obviously, though, I frequently needed to solve the full, time-dependent CHR system. To illustrate my approach, I have included the Matlab source code used to solve time-dependent and equilibrium problems in one dimension. This includes functions for solving many different reaction-diffusion equations, including Fick's law, diffusion with a regular solution free energy, and the CHR system in various parameter regimes. Though I have also solved these problems in two dimensions, the code to do so is very similar to the one-dimensional version, so it is not included here.

The general pattern for working with this software is as follows: The user first calls the function `chr1d_params_init()` (included in § A.1) to build a parameters structure. This selects a reaction-diffusion model, sets all of the physical parameters for that model, and describes the numerical method used to solve the equations. Along with the initial concentration field, this structure is then passed to the function `chr1d_solve()` (included in § A.2) which solves the requested problem. Finally, the user may pass the results to the function `chr1d_animate()` (not included) for analysis (plotting concentration and chemical potential fields, computing voltages and currents, etc.).

### A.1 `chr1d_params_init.m`

```
1 % chr1d_params_init()
%
% This function builds the parameters structure used by the other chr1d_]()
% routines. Every parameter may be set by the user, though reasonable defaults
5 % are provided. See below for details.
%
% chr1d_params_init() returns the default parameters structure
%
% chr1d_params_init('name1,value1, 'name2',value2, ...) returns the default
```

```

10 % parameters structure, except that parameter namei is set to valuei
%
% chrld_params_init(params,'name1,value1, 'name2',value2, ...) returns the
% parameters structure params, except that parameter namei is set to valuei
function params = chrld_params_init(varargin)
15
%%%%%%%%%%%%%
% BUILD THE DEFAULT PARAMETERS STRUCTURE %
%%%%%%%%%%%%%

20
%%%%%%%%%%%%%
% PHYSICAL CONSTANTS %
%%%%%%%%%%%%%

25
% Boltzmann constant in joules/kelvin
def.phys.kB      = 1.3806504e-23;

30
% Avogadro number
def.phys.NA      = 6.02214179e23;

35
% elementary charge in coulombs
def.phys.q       = 1.602176487e-19;

% temperature in kelvins
def.phys.T       = 300;

40
% standard voltage of the redox reaction Li + FePO4 -> LiFePO4
% The default is taken from ab-initio calculations in
% Phys. Rev. B 70, 235121 (2004).
def.phys.E       = 3.47;

45
% free energies (in electron volts per molecule) of pure Li, FePO4, and
% LiFePO4
% These defaults are room temperature data from Fei Zhou's atomistics
def.phys.gLi     = -1.899;
def.phys.gFePO4  = -42.6328;
def.phys.gLiFePO4 = -48.10;

50
% diffusion constant for the system, in m^2/s
% This default comes from Ceder's paper for LiFePO4.
def.phys.D       = 1e-11;

% the gradient penalty length, in meters
def.phys.lambda   = 1e-9;

55
%%%%%%%%%%%%%
% MODEL %
%%%%%%%%%%%%%

```

```

% the diffusion model to use
def.model.diffusion = 'cahn_hilliard';

% This is the inverse of the dimensionless total (dis)charge time for
65 % simulations with constant (dis)charge rates. The default is [], which indicates that params.ndg.mu_e should remain constant
% throughout the simulation.
def.model.C_rate = [];

70 % true if and only if the equations should be solved in the SRL limit,
% i.e. if the bulk relaxation should occur instantaneously between
% time-steps at the boundary
% If SRL_limit is false, then the Damkohler number is taken literally:
% Da==0 requires no-flux boundary conditions, and Da>0 sets the
75 % relative time-scale for the boundary reactions. If SRL_limit is
% true, then Da is ignored, and the PDE is solved on the reactive
% time-scale. Note that the SRL limit can apply even to real systems
% with large Damkohler numbers, for instance if the reactants are very
% dilute.
80 def.model.SRL_limit = false;

85 % true if and only if time integration should be skipped in favor of
% solving directly for a steady state
def.model.equilibrate = false;

90 %%%%%%
% NON-DIMENSIONAL GROUPS %
%%%%%%%%%%%%

95 % enthalpy of mixing per molecule, non-dimensionalized by k_B*T
% According to experimental data, this should be about 5 for LiFePO4 at
% 300K (c.f. Dodd, Yazami, and Fultz in Electrochemical and Solid-State
% Letters, volume 9, number 3, pages A151—A155, 2006).
def.ndg.a = 5;

100 % length of the system, non-dimensionalized by $\lambda
def.ndg.L = 10;

105 % Damkohler number $k_b \lambda^2 / D$, where $k_b$ is the rate constant
% for the backward reaction FePO4 + Li+ + e- <-- LiFePO4
% If this is 0, there are no boundary reactions. If this is Inf
% (i.e. if we are in the BTL limit), then the boundary reaction is
% replaced with a boundary condition on the chemical potentials.
def.ndg.Da = 1;

110 % sum of the electrochemical potentials of the external electron and
% Li+ ion, divided by k_BT
def.ndg.mu_e = 0;

```

```

% $\\rho_s / \\rho$, non-dimensionalized by $\\lambda$
% This should be equal to the non-dimensionalized width of a unit cell
% in the crystal, or equivalently the inverse of the width of the phase
% transition given as a number of unit cells. In the model, this only
% appears as a multiplier for Da, but we'll keep them separate for
% clarity.
115 def.ndg.w = 1/3;

120

%%%%%%%%%%%%%
% NUMERICS %
%%%%%%%%%%%%%

125
% the number of grid points in the space discretization
def.num.N = 100;

130
% which time-stepping scheme to use
def.num.ode = 'crank_nicolson';

% This is the RelTol option for the integrator (see help for odeset()).
% This is the primary parameter for improved accuracy when an internal
% Matlab time-stepper is being used.
135 def.num.RelTol = [];

% This is the MaxStep option for the integrator (see help for odeset()).
% It is used to decrease the number of time-steps output by my
% implicit time-steppers.
140 def.num.MaxStep = [];

% This is the AbsTol option for the integrator (see help for odeset()).
% This is the primary parameter for improved accuracy when my
% implicit time-steppers are used.
145 def.num.AbsTol = [];

%%%%%%%%%%%%%
% BUILD THE REQUESTED PARAMETERS STRUCTURE %
%%%%%%%%%%%%%
150 Names = {'kB'; 'NA'; 'q'; 'T'; 'E'; 'gL'; 'gFePO4'; 'gLFePO4'; ...
           'D'; 'lambda'; ...
           'diffusion'; 'C_rate'; 'SRL_limit'; 'equilibrate'; ...
           'a'; 'L'; 'Da'; 'mu_e'; 'w';
           'N'; 'ode'; 'RelTol'; 'MaxStep'; 'AbsTol' };
155 sub_structs = {'phys'; 'phys'; 'phys'; 'phys'; 'phys'; ...
                 'phys'; 'phys'; 'phys'; 'phys'; 'phys'; ...
                 'model'; 'model'; 'model'; 'model'; ...
                 'ndg'; 'ndg'; 'ndg'; 'ndg'; 'ndg'; ...
                 'num'; 'num'; 'num'; 'num'; 'num'; };
160 [params,err_str] = build_options_struct(def, varargin, Names, sub_structs);

```

```

    if (~isempty(err_str))
        error(err_str);
165 end
end

```

## A.2 chr1d\_solve.m

```

1 % chr1d_solve()
%
% This is semi-discrete, finite-volume-method code for solving various
% 1-dimensional diffusion problems. See chr1d_params_init() for a description
5 % of the parameters; see below for allowable values, combinations, and
% simplifications.
%
% The grid layout is as follows:
%
10 %      cbar_1   cbar_2     ...   cbar_N
%      |       |       |       ...
%      o       o       o       ...
%      x_0     x_1     x_2     ...
%      |       |       |       ...
%      x_N
%
% Each "|" marks a boundary for a control volume;
15 % x_0=0, N=params.num.N, and x_N=params.ndg.L.
% Each "o" marks the mid-point of a control volume at which a value for cbar is
% stored. Each cbar is an AVERAGE concentration over a control volume
% (and consequently a second-order-accurate approximation for the exact
% concentration at the mid-point of the control volume).
20 % Fluxes are computed at the boundaries BETWEEN control volumes.
%
% parameters:
% params - the chr1d parameters structure
% ts      - the array of time steps at which data will be output
25 % cbars0 - the concentration field at time 0; in the finite-volume
%           interpretation, cbars(i) is the average concentration between
%           (i-1)*h and i*h, where h=params.ndg.L/params.num.N
%
% returns:
30 % T - copy of ts
% Y - Y(i,j) will be the value of cbar for the control volume between
%      x_{j-1} and x_j at time T(i)
% MU - if a constant C-rate simulation is being performed, then
%      MU(i) will be the mean mu_e needed between T(i) and T(i+1)
35 function [T,Y,MU] = chr1d_solve(params, ts, cbars0)

%%%%%%%%%%%%%
% INITIALIZATION %
%%%%%%%%%%%%%
40
% Validate the inputs
if (nargin ≠ 3)

```

```

        error('exactly 3 input parameters required');
end
if (~isstruct(params))
    error('1st argument must be the struct returned by chrld.params_init');
end
if (numel(cbars0) ~= params.num.N)
    error('cbars0 must have exactly params.num.N elements');
end
if ( any(cbars0(:)≤0) || any(cbars0(:)≥1) )
    warning('cbars0 should consist only of data between 0 and 1');
end

55
% Get the ode function corresponding to the requested diffusion model
odefun_code = {'fick'; ...
               'fick_regular'; ...
               'cahn_hilliard'; ...
               'cahn_hilliard_depth_averaged'; ...
               'cahn_hilliard_cook'};
odefun_func = {@odefun_fick; ...
               @odefun_fick_regular; ...
               @odefun_cahn_hilliard; ...
               @odefun_cahn_hilliard_depth_averaged; ...
               @odefun_cahn_hilliard_cook};
odefun_jac = {@Jac_fick; ...
               @Jac_fick_regular; ...
               @Jac_cahn_hilliard; ...
               @Jac_cahn_hilliard_depth_averaged; ...
               []};
odefun_desc = {'Fick''s law (no-flux boundary conditions)'; ...
               'regular-solution Fick''s law (no-flux boundary conditions)'; ...
               'Cahn-Hilliard equation'; ...
               'depth-averaged Cahn-Hilliard with reactions'; ...
               'Cahn-Hilliard-Cook equation'};

75
ind = strmatch(params.model.diffusion, odefun_code, 'exact');
if (isempty(ind))
    error('unknown diffusion model: %s', params.model.diffusion);
end
odefun = odefun_func{ind};
jacfun = odefun_jac{ind};
desc = cat(2, 'bulk kinetics : ', odefun_desc{ind});
if (ind == 3)
    if (params.ndg.Da == 0)
        odefun = @odefun_cahn_hilliard;
        jacfun = @Jac_cahn_hilliard;
        desc = cat(2, desc, ' (no-flux boundary conditions)');
    elseif (params.ndg.Da == Inf)
        odefun = @odefun_cahn_hilliard_BTL;
        jacfun = @Jac_cahn_hilliard_BTL;
        desc = cat(2, desc, ' (BTL specialization)');
    elseif (~isempty(params.model.C_rate))

```

```

95      odefun = @odefun_cahn_hilliard_C_rate;
96      jacfun = @Jac_cahn_hilliard_C_rate;
97      desc   = cat(2, desc, ' (constant C-rate)');
98  else
99      odefun = @odefun_cahn_hilliard_reaction;
100     jacfun = @Jac_cahn_hilliard_reaction;
101     desc   = cat(2, desc, ' (reaction boundary conditions)');
102 end
103 disp(desc);

105 % Pick the integrator
106 integrator_code = {'ode15s'; ...
107     'ode23'; ...
108     'ode23s'; ...
109     'ode45'; ...
110     'backward_euler'; ...
111     'crank_nicolson'};
112 integrator_func = {@ode15s; ...
113     @ode23; ...
114     @ode23s; ...
115     @ode45; ...
116     @odebe; ...
117     @odecn};
118 integrator_desc = {'ode15s (built-in)'; ...
119     'ode23 (built-in)'; ...
120     'ode23s (built-in)'; ...
121     'ode45 (built-in)'; ...
122     'backward Euler'; ...
123     'Crank-Nicolson'};

125 ind = strmatch(params.num.ode, integrator_code, 'exact');
126 if (isempty(ind))
127     error('unknown integrator: %s', params.num.ode);
128 end
129 integrator = integrator_func{ind};
130 desc       = cat(2, 'time stepper : ', integrator_desc{ind});
131 disp(desc);

135 % Pick a meta-integrator if needed
136 meta_integrator = [];
137 if (params.model.equilibrate)
138     disp('specialization: computing steady-state solution');
139     meta_integrator = @metafun_equilibrium;
140 elseif (params.model.SRL_limit)
141     disp('specialization: SRL regime');
142     meta_integrator = @metafun_SRL;
143 elseif ( strcmp(params.model.diffusion, 'cahn_hilliard_cook') ...
144         || strcmp(params.model.diffusion, 'chcr') ...
145         || strcmp(params.model.diffusion, 'chc') )

```

```

145      disp('specialization: stochastic Cahn–Hilliard–Cook');
      meta_integrator = @metafun_cahn_hilliard_cook;
    end

150
% Store a few constants
N = params.num.N;
h = params.ndg.L / N;

155
% Preallocate memory for the arrays used by the odefuns
cs      = zeros(N+1, 1); % approximation for the concentrations at the
% control volume boundaries
cls     = zeros(N+1, 1); % approximation for the first (spatial)
% derivatives of the concentration field at the
% control volume boundaries
160
lap     = zeros(N+1, 1); % approximation for the Laplacian at the
% control volume boundaries
c3s    = zeros(N+1, 1); % approximation for the third (spatial)
% derivatives of the concentration field at the
% control volume boundaries
165
Js     = zeros(N+1, 1); % approximation for the fluxes at the
% control volume boundaries
cbars_t = zeros(N, 1); % time derivative of cbars
      % The temp variables are intermediates in the Jacobian computations
temp1   = zeros(N+1, 1);
temp2   = zeros(N+1, 1);
      % The following are only used by the reaction boundary conditions
cl     = 0; % approximation for the concentration at the left edge x_0
cr     = 0; % approximation for the concentration at the right edge x_N
175
lapl   = 0; % approximation for the Laplacian (which is just the second
% derivative in the 1-d case) at the left edge x_0
lapr   = 0; % approximation for the Laplacian (which is just the second
% derivative in the 1-d case) at the right edge x_N
aL     = 0;
aF     = 0;
aLl   = 0;
aFl   = 0;
aLr   = 0;
aFr   = 0;
180
mul   = 0;
mur   = 0;

185
% Make the differentiation matrices. Di*cbars yields the vector of ith
% derivatives of c at the control volume boundaries with the following
% exceptions: first, the first and last elements of Di*cbars are 0 because
% these are primarily used by the no-flux computations; second, the second
% and second-to-last elements of Di*cbars are computed using the
% homogeneous Neumann boundary conditions.
190
D0 = sparse(2:N, 2:N, +1/2, N+1, N) ...
195

```

```

    + sparse(2:N, 1:(N-1), +1/2, N+1, N);
D1 = sparse(2:N, 2:N, +1/h, N+1, N) ...
    + sparse(2:N, 1:(N-1), -1/h, N+1, N);
D3 = sparse(3:(N-1), 4:N, +1/h^3, N+1, N) ...
    + sparse(3:(N-1), 3:(N-1), -3/h^3, N+1, N) ...
    + sparse(3:(N-1), 2:(N-2), +3/h^3, N+1, N) ...
    + sparse(3:(N-1), 1:(N-3), -1/h^3, N+1, N);
D3(2,1:4) = [+25,-39,+15,-1]/(10*h^3);
D3(end-1,(end-3):end) = [+1,-15,+39,-25]/(10*h^3);

205

% Make differentiation matrices for the mid-points of the control volumes.
% Unlike the above, these compute the derivatives even at the ends; these
% two values are computed using a formula modified to account for the
% variational boundary condition.
210 D0_mid = speye(N);
D1_mid = sparse(2:(N-1), 3:N, +1/(2*h), N, N) ...
    + sparse(2:(N-1), 1:(N-2), -1/(2*h), N, N);
D1_mid(1,1:2) = [-1,+1]/(2*h);
215 D1_mid(N,(N-1):N) = [-1,+1]/(2*h);
D2_mid = sparse(2:(N-1), 3:N, +1/h^2, N, N) ...
    + sparse(2:(N-1), 2:(N-1), -2/h^2, N, N) ...
    + sparse(2:(N-1), 1:(N-2), +1/h^2, N, N);
D2_mid(1,1:3) = [-13,+14,-1]/h^2;
220 D2_mid(N,(N-2):N) = [-1,+14,-13]/h^2;

225 %%%%%%
% DIFFUSION MODELS %
%%%%%%

230 % Fick's law c_t=c_xx with no-flux boundary conditions
% the Jacobian is independent of c, so may be precomputed
Jf = 1/h^2*( sparse(1:N, 1:N, [-1;-2+zeros(N-2,1);-1], N, N)...
    + sparse(1:(N-1), 2:N, +1, N, N)...
    + sparse(2:N, 1:(N-1), +1, N, N) );
235 function Jac = Jac_fick(t,cbars)
    Jac = Jf;
end
function [cbars_t,Jac] = odefun_fick(t,cbars)
    Js = -D1*cbars;
240    cbars_t = (-1/h)*diff(Js);
    if (nargout > 1)
        Jac = Jf;
    end
end
245
```

```

% This is the Fick's law using the regular solution model chemical potential
%  $a(1-2c) + \log(c/(1-c))$ . Note that when  $a>2$ , the system is
% phase-separating, and the solutions will have discontinuities. We still
% employ no-flux boundary conditions.
250 function Jac = Jac_fick_regular(t,cbars)
    temp1 = cls.* (2*params.ndg.a - 1./((1-cs).^2));
    temp2 = 2*params.ndg.a*cs - 1./(1-cs);
    fJac = sparse(1:(N+1), 1:(N+1), temp1, N+1, N+1) * D0 ...
255           + sparse(1:(N+1), 1:(N+1), temp2, N+1, N+1) * D1;
    Jac = (-1/h)*diff(fJac);
end
function [cbars_t,Jac] = odefun_fick_regular(t,cbars)
    cs = D0*cbars;
260    cls = D1*cbars;
    Js = 2*params.ndg.a*cs.*cls - cls./(1-cs);
    cbars_t = (-1/h)*diff(Js);
    if (nargout > 1)
        Jac = Jac_fick_regular(t,cbars);
    end
265 end

% Compute the Jacobian of the Cahn–Hilliard flux (including the 0–flux at
270 the boundaries). It is assumed that cs, cls, and c3s have all already
been computed and stored in global variables.
function fJac = fJac_cahn_hilliard()
    temp1 = c3s + cls.* (2*params.ndg.a - 1./((1-cs).^2));
    temp2 = 2*params.ndg.a*cs - 1./(1-cs);
275    fJac = sparse(1:(N+1), 1:(N+1), temp1, N+1, N+1) * D0 ...
           + sparse(1:(N+1), 1:(N+1), temp2, N+1, N+1) * D1 ...
           + sparse(1:(N+1), 1:(N+1), cs, N+1, N+1) * D3;
end

280 % Compute the Jacobian of the Cahn–Hilliard time–derivative, taking the
% no–flux and no–gradient boundary conditions into account.
function oJac = Jac_cahn_hilliard(t,cbars)
    fJac = fJac_cahn_hilliard();
285    oJac = (-1/h)*diff(fJac);
end

% Cahn–Hilliard diffusion with no–flux boundary conditions
290 % (along with the variational boundary condition)
function [cbars_t,Jac] = odefun_cahn_hilliard(t,cbars)
    % Compute 2nd-order-accurate approximations for the concentrations and
    % their 1st- and 3rd-derivatives at all control volume boundaries
    % except the leftmost and rightmost. The variational boundary
    % condition is used to derive special formulas for the 3rd derivatives
    % near the ends.
    cs = D0*cbars;

```

```

cls = D1*cbars;
c3s = D3*cbars;

300
% Compute 2nd-order-accurate approximations for the fluxes at all
% control volume boundaries (including the leftmost and rightmost).
% The no-flux boundary condition is implemented exactly.
Js = (2*params.ndg.a)*cs.*cls - cls./(1-cs) + cs.*c3s;

305
% This formula is exact in the Finite Volume setting. Given that Js is
% 2nd-order accurate, it might look like we should only get 1st-order
% convergence; however, it can be shown that with Js computed as above,
% cbars_t(i) is 2nd-order accurate everywhere except at i=1,2,N-1,N.
310 cbars_t = (-1/h) * diff(Js);

% Compute the Jacobian of cbars_t if requested
if (nargout > 1)
    Jac = Jac_cahn_hilliard(t,cbars);
end
end

320
% Compute the Jacobian of the Cahn-Hilliard-with-reactions flux. It is
% assumed that cs, cls, c3s, cl, cr, lapl, lapr, aLl, aLr, aFl, and aFr
% have all already been computed and stored in global variables.
function fJac = fJac_cahn_hilliard_reaction()
    % Compute the flux gradients for a system with no-flux boundary
    % conditions
    fJac = fJac_cahn_hilliard();

    % Adjust the first and last flux gradients to take the reactions into
    % account
    c = [cl , cr];
    lap = [lapl , lapr];
    aL = [aLl , aLr];
    aF = [aFl , aFr];
    dc = [+1,      0,      0,      0,      0; ...
            0,      0,      0,      0,      +1 ];
330
    dlap = [-25, +32, -7, 0, 0; ...
              0,      0,      -7, +32, -25] / (11*h^2);
    dR = (params.ndg.w*params.ndg.Da) ...
        * ( ( aL.*(-2*params.ndg.a*(1-c)+1./c+lap) ...
            - exp(params.ndg.mu_e)*aF ...
            .* (2*params.ndg.a*c-1./(1-c)+lap) )*dc ...
        + ( aL.*(-(1-c)) - exp(params.ndg.mu_e)*aF.*((c) )*dlap );
340
    fJac(1,1:3) = -dR(1:3);
    fJac(end,(N-2):N) = +dR(4:6);
end

345
% Compute the Jacobian of the CHR time-derivative, taking the
% reaction and variational boundary conditions into account.

```

```

function oJac = Jac_cahn_hilliard_reaction(t,cbars)
350    fJac = fJac_cahn_hilliard_reaction();
    oJac = (-1/h)*diff(fJac);
end

355 % Cahn-Hilliard diffusion with reaction boundary conditions; the reactions
% are modeled using the kinetic law of mass action and my variational
% chemical activities
function [cbars_t,Jac] = odefun_cahn_hilliard_reaction(t,cbars)
    % Perform the no-flux computations
360    cbars_t = odefun_cahn_hilliard(t,cbars);

    % Reset the time derivatives at the edges to satisfy the reaction
    % boundary condition rather than the no-flux boundary condition;
    % this takes advantage of the fact that the Js vector is filled in
365    % already. The concentrations and laplacians are computed at the
    % end-points using Taylor expansions which explicitly account for the
    % variational boundary condition.
    cl      = cbars(1);
    cr      = cbars(end);
370    lapl   = 1/(11*h^2) * (-25*cbars(1) + 32*cbars(2) - 7*cbars(3));
    lapr   = 1/(11*h^2) * (-25*cbars(end)+32*cbars(end-1)-7*cbars(end-2));
    aLl    = cl      * exp(params.ndg.a*(1-cl)^2 - (1-cl)*lapl);
    aLr    = cr      * exp(params.ndg.a*(1-cr)^2 - (1-cr)*lapr);
    aFl    = (1-cl) * exp(params.ndg.a*cl^2 + cl*lapl);
375    aFr    = (1-cr) * exp(params.ndg.a*cr^2 + cr*lapr);
    Js(1)  = (-params.ndg.w*params.ndg.Da)*(aLl-exp(params.ndg.mu_e)*aFl);
    Js(end) = (+params.ndg.w*params.ndg.Da)*(aLr-exp(params.ndg.mu_e)*aFr);
    cbars_t(1) = (-1/h) * (Js(2) - Js(1));
    cbars_t(end) = (-1/h) * (Js(end) - Js(end-1));
380
    % Compute the Jacobian of cbars_t if requested
    if (nargout > 1)
        Jac = Jac_cahn_hilliard_reaction(t,cbars);
    end
end

385

% Compute the Jacobian of the constant C-rate flux. It is
% assumed that cs, cls, c3s, cl, cr, lapl, lapr, aLl, aLr, aFl, and aFr
390 % have all already been computed and stored in global variables.
function fJac = fJac_cahn_hilliard_C_rate()
    % Compute the Jacobians of the flux vector using reaction boundary
    % conditions.
    fJac = fJac_cahn_hilliard_reaction();

395
    % Correct these Jacobians for the dependence of mu_e on the
    % concentrations near both boundaries.
    c      = [cl , cr];
    lap   = [lapl, lapr];

```

```

400      aL    = [aLl , aLr];
401      aF    = [aFl , aFr];
402      dc    = [+1,      0,      0,      0,      0; ...
403                  0,      0,      0,      0,      +1 ];
404      dlap  = [-25,   +32,   -7,      0,      0; ...
405                  0,      0,      0,     -7,   +32,   -25] / (11*h^2);
406      dsaL  = (params.ndg.w*params.ndg.Da/h) ...
407          * ( ( aL.*(-2*params.ndg.a*(1-c)+1./c+lap) )*dc ...
408              + ( aL.*(-(1-c)) )*dlap );
409      dsaF  = (params.ndg.w*params.ndg.Da/h) ...
410          * ( ( aF.*(2*params.ndg.a*c-1./(1-c)+lap) )*dc ...
411              + ( aF.*(c) )*dlap );
412      saL   = (params.ndg.w*params.ndg.Da/h)*(aLl+aLr);
413      saF   = (params.ndg.w*params.ndg.Da/h)*(aFl+aFr);
414      dmu_e = exp(-params.ndg.mu_e)/saF^2 ...
415          * ( saF*dsaL - (params.model.C_rate*N+saL)*dsaF);
416      fJac(1,1:3) = fJac(1,1:3) ...
417          + params.ndg.w*params.ndg.Da ...
418          * exp(params.ndg.mu_e)*aFl*dmu_e(1:3);
419      fJac(1,(N-2):N) = fJac(1,(N-2):N) ...
420          + params.ndg.w*params.ndg.Da ...
421          * exp(params.ndg.mu_e)*aFl*dmu_e(4:6);
422      fJac(N+1,1:3) = fJac(N+1,1:3) ...
423          - params.ndg.w*params.ndg.Da ...
424          * exp(params.ndg.mu_e)*aFr*dmu_e(1:3);
425      fJac(N+1,(N-2):N) = fJac(N+1,(N-2):N) ...
426          - params.ndg.w*params.ndg.Da ...
427          * exp(params.ndg.mu_e)*aFr*dmu_e(4:6);
428  end

430
431 % Compute the Jacobian of the constant-C-rate time-derivative.
432 function oJac = Jac_cahn_hilliard_C_rate(t,cbars)
433     fJac = fJac_cahn_hilliard_C_rate();
434     oJac = (-1/h)*diff(fJac);
435 end

440
441 % This function performs a constant C-rate integration of the CHR equations.
442 % This is done by computing a new value for params.ndg.mu_e during each call
443 % in order to fix a constant value for the sum of the reaction boundary
444 % fluxes.
445 function [cbars_t,Jac] = odefun_cahn_hilliard_C_rate(t,cbars)
446     % Perform the no-flux computations
447     cbars_t = odefun_cahn_hilliard(t,cbars);

450     % Reset the time derivatives at the edges to satisfy the reaction
        % boundary condition rather than the no-flux boundary condition;
        % this takes advantage of the fact that the Js vector is filled in
        % already. The concentrations and laplacians are computed at the
        % end-points using Taylor expansions which explicitly account for the

```

```

% variational boundary condition.
cl    = cbars(1);
cr    = cbars(N);
lapl = 1/(11*h^2) * (-25*cbars(1)+32*cbars(2) - 7*cbars(3));
455   lapr = 1/(11*h^2) * (-25*cbars(N)+32*cbars(N-1)-7*cbars(N-2));
aLl  = cl    * exp(params.ndg.a*(1-cl)^2 - (1-cl)*lapl);
aLr  = cr    * exp(params.ndg.a*(1-cr)^2 - (1-cr)*lapr);
aFl  = (1-cl) * exp(params.ndg.a*cl^2      +      cl*lapl);
aFr  = (1-cr) * exp(params.ndg.a*cr^2      +      cr*lapr);
460   saL  = (params.ndg.w*params.ndg.Da/h)*(aLl+aLr);
saF  = (params.ndg.w*params.ndg.Da/h)*(aFl+aFr);
params.ndg.mu_e = log( (params.model.C_rate*N+saL) / saF );
Js(1)  = (-params.ndg.w*params.ndg.Da)*(aLl-exp(params.ndg.mu_e)*aFl);
Js(end) = (+params.ndg.w*params.ndg.Da)*(aLr-exp(params.ndg.mu_e)*aFr);
465   cbars_t(1)  = (-1/h) * (Js(2) - Js(1));
cbars_t(end) = (-1/h) * (Js(end) - Js(end-1));

% Reset the appropriate element of the output variable MU.
% XXX This may fail for the built-in integrators which can take steps
470   % larger than diff(ts), and it will be slow for large ts arrays.
[min_val,min_ind] = min(abs(ts(:)-t));
MU(min_ind) = params.ndg.mu_e;

% Compute the Jacobian of cbars_t if requested
475   if (nargout > 1)
        Jac = Jac_cahn_hilliard_C_rate(t,cbars);
    end
end

480
% Compute the Jacobian of the BTL time-derivative, taking the
% mu=mu_{ext} and variational boundary conditions into account.
function oJac = Jac_cahn_hilliard_BTL(t,cbars)
    % Compute the flux gradients for a system with no-flux boundary
485   % conditions
    fJac = fJac_cahn_hilliard();

    % Adjust the first and last flux gradients to take the mu=mu_{ext}
    % boundary condition into account
    fJac(1,1)  = 1/h*(params.ndg.mu_e-mul+2*params.ndg.a*cl-1/(1-cl));
    fJac(1,1:3) = fJac(1,1:3) + cl/h*[-13,+14,-1]/(11*h^2);
    fJac(end,end) = 1/h*(mur-params.ndg.mu_e-2*params.ndg.a*cr+1/(1-cr));
    fJac(end,end-2:end) = fJac(end,end-2:end) - cr/h*[-1,+14,-13]/(11*h^2);

495   % Compute the gradients for the time derivatives
    oJac = (-1/h)*diff(fJac);
end

500   % Cahn-Hilliard diffusion in the Bulk-Transport-Limited regime;
% thus the boundary reactions are assumed to happen infinitely quickly,

```

```

% so the kinetic law of mass action may be replaced with equality of
% chemical potentials
function [cbars_t,Jac] = odefun_cahn_hilliard_BTL(t,cbars)
505    % Perform the no-flux computations
    cbars_t = odefun_cahn_hilliard(t,cbars);

    % Reset the time derivatives at the edges to satisfy the
    % fixed-chemical-potential boundary condition rather than the no-flux
510    % boundary condition. The method for doing this is very imperfect:
    % at the left edge, mu is computed at x_{1/2} using the FVM formulas
    % with c'(x_0)=0. It is then assumed that mu_{-1/2} is equal to
    % mu_{ext}, and the flux at x_0 is computed as
    % -c_0*(mu_{+1/2}-mu_{-1/2})/h.
515    cl      = cbars(1);
    cr      = cbars(end);
    lapl   = 1/(11*h^2) * (-13*cbars(1) +14*cbars(2) -cbars(3));
    lapr   = 1/(11*h^2) * (-13*cbars(end)+14*cbars(end-1)-cbars(end-2));
    mul    = params.ndg.a*(1-2*cl) + real(log(cl/(1-cl))) - lapl;
520    mur    = params.ndg.a*(1-2*cr) + real(log(cr/(1-cr))) - lapr;
    Js(1)  = -cbars(1) * (mul-params.ndg.mu_e)/h;
    Js(end) = -cbars(end) * (params.ndg.mu_e-mur)/h;
    cbars_t(1) = (-1/h) * (Js(2) - Js(1));
    cbars_t(end) = (-1/h) * (Js(end) - Js(end-1));

525    % Compute the Jacobian of cbars_t if requested
    if (nargout > 1)
        Jac = Jac_cahn_hilliard_BTL(t,cbars);
    end
530 end

% This is the odefun for the depth-averaged Cahn-Hilliard-with-reactions
% kinetics. In this case, cbars(i) is the concentration of a 1-d ion
% channel, and the kinetics are driven entirely by the boundary reactions.
535    % As such, there are no diffusive fluxes, and this isn't a finite volume
    % method at all. For consistency, however, we retain the model in which
    % the inputs are the control-volume averages.
function Jac = Jac_cahn_hilliard_depth_averaged(t,cbars)
540    Jac_aF = sparse(1:N, 1:N,
                      (2*params.ndg.a*cs+lap-1./(1-cs)).*aF, ...
                      N, N) * D0_mid ...
545    + sparse(1:N, 1:N, cls.*aF, N, N) * D1_mid ...
    + sparse(1:N, 1:N, cs.*aF, N, N) * D2_mid;
    Jac_aL = sparse(1:N, 1:N,
                      (2*params.ndg.a*(cs-1)+lap+1./cs).*aL, ...
                      N, N) * D0_mid ...
550    + sparse(1:N, 1:N, cls.*aL, N, N) * D1_mid ...
    + sparse(1:N, 1:N, (cs-1).*aL, N, N) * D2_mid;
    Jac    = exp(params.ndg.mu_e)*Jac_aF - Jac_aL;
end
function [cbars_t,Jac] = odefun_cahn_hilliard_depth_averaged(t,cbars)

```

```

    cs = D0_mid*cbars;
    cls = D1_mid*cbars;
    lap = D2_mid*cbars;
555
    aL = cs .* exp((1-cs).*(params.ndg.a*(1-cs) - lap) + 1/2*cls.^2);
    aF = (1-cs).* exp( cs .*(params.ndg.a*cs + lap) + 1/2*cls.^2);
    cbars_t = exp(params.ndg.mu_e)*aF - aL;
    if (nargout > 1)
        Jac = Jac_cahn_hilliard_depth_averaged(t,cbars);
560
    end
end

565

%%%%%%%%%%%%%
% SPECIALIZED INTEGRATORS %
%%%%%%%%%%%%%

570

% Solve directly for a nearby steady state rather than doing any time
% stepping.
function [T,Y] = metafun_equilibrium(odefun, integrator, options)
    % optimization function; this is only needed to strip the time
    % parameter from the inputs to odefun
    function [cbars_t,Jac] = foo(cbars)
        if (nargout == 1)
            cbars_t = odefun(0,cbars);
575
        else
            [cbars_t,Jac] = odefun(0,cbars);
        end
    end
580
end

% The time vector doesn't make much sense here
T = Inf;

% Solve for the steady-state
fs_options = optimset('Display','on', 'Jacobian','on', ...
585
    'TolFun',params.num.AbsTol, ...
    'TolX',params.num.RelTol);
Y = fsolve(@foo, reshape(cbars0,N,1), fs_options)';
end

590
595

% This is the integrator for Cahn–Hilliard diffusion with reaction boundary
% conditions in the Surface–Reaction–Limited regime. Thus between
% time–steps of the reaction ODEs, the bulk concentration field is
% completely relaxed (using no–flux boundary conditions).
600
function [T,Y] = metafun_SRL(odefun, integrator, options)
    % Initialize the outputs
    T = ts;

```

```

Y = zeros(numel(cbars0), numel(ts)); % we'll transpose later
605

% Set up future calls to fsolve
fs_options = optimset('Display','off', 'Jacobian','on', ...
    'TolFun',params.num.AbsTol, ...
    'TolX',params.num.RelTol);

610 function [cbars_t,Jac] = foo(cbars)
    if (nargout == 1)
        cbars_t = odefun_cahn_hilliard(0,cbars);
    else
        [cbars_t,Jac] = odefun_cahn_hilliard(0,cbars);
    end
end

% initial bulk relaxation
Y(:,1) = fsolve(@foo, reshape(cbars0,N,1), fs_options);
620 if ( any(isnan(Y(:,1))) || any(Y(:,1)≥1) || any(Y(:,1)≤0) )
    error('oops #1');
end

% integration
625 for i=2:numel(ts)
    % Perform the bulk relaxation using the Crank–Nicolson method.
    % Perform a few backward Euler iterations before and after.
    % This is recommended in a paper by Ole Osterby to reduce the
    % oscillations that arise when using the Crank–Nicolson integrator
    % when the initial conditions don't already satisfy the boundary
    % conditions. In our case, the problem arises by ignoring the
    % reactions during the bulk relaxation.

    % Step the boundary conditions using the requested integrator.
    % Use 3 time steps instead of just 2 to ensure that built-in
    % integrators don't return data for ALL intermediate time steps.
    [Tbc,Ybc] = integrator(@odefun_cahn_hilliard_reaction, ...
        [T(i-1),1/2*(T(i-1)+T(i)),T(i)], ...
        Y(:,i-1), options);
635    if ( any(isnan(Ybc(:))) || any(Ybc(:)≥1) || any(Ybc(:)≤0) )
        error('oops #2');
    end

    % Bulk relaxation
640    Y(:,i) = fsolve(@foo, Ybc(end,:)', fs_options);
    if ( any(isnan(Y(:,i))) || any(Y(:,i)≥1) || any(Y(:,i)≤0) )
        error('oops #3');
    end
end

645 % Transpose the output matrix to put it in the standard form of
% Matlab's solvers' output.
Y = Y';

```

```

% Cahn–Hilliard–Cook stochastic integrator
function [T,Y] = metafun_cahn_hilliard_cook(odefun, integrator, options)
    % initialization
    T = reshape(ts,numel(ts),1);
    Y = zeros( numel(cbars0) , numel(ts) );

    % Get the relevant parameters from the ODE options structure
    tolx = odeget(options, 'AbsTol');
    max_step = odeget(options, 'MaxStep', Inf);

    % Build the optimization options structure; make sure that fsolve()
    % doesn't talk to the user every time it is called
    fs_options = optimset('Display','off');
    if (~isempty(tolx) && (tolx > 0))
        fs_options = optimset(fs_options, 'TolX',tolx, 'TolFun',tolx);
    end

    % The data for the first time step is given to us
    Y(:,1) = reshape(cbars0,numel(cbars0),1);

    % March through the remaining time steps
    ys_old = Y(:,1);
    prefactor = sqrt(params.ndg.w / h^3);
    for n=1:(numel(ts)-1)
        t_n      = ts(n);
        t_np1   = ts(n+1);
        dt = t_np1 - t_n;

        % Decide how many integration steps to take between the two
        % time-steps at which solutions are to be output
        num_substeps = max( 1 , ceil(abs(dt/max_step) - 0.01) );

        % Integrate from t_n to t_np1 in num_substeps evenly-spaced steps
        sub_dt = dt / num_substeps;
        for j=1:num_substeps
            t_old      = t_n + (j-1)*sub_dt;
            t_new      = t_n + j*sub_dt;
            yprime_old = odefun_cahn_hilliard(t_old, ys_old);
            fun        = @(ys)( ys-ys_old ...
                - (sub_dt/2) ...
                * ( yprime_old ...
                    + odefun_cahn_hilliard(t_new,ys)));
            etas      = prefactor*sqrt(sub_dt) ...
                * sqrt(ys_old(1:(end-1)) + ys_old(2:end)) ...
                .* randn(numel(cbars0)-1,1);
            ys_old    = fsolve(fun, ys_old, fs_options) ...
                + ([0;etas] - [etas;0]);
        end
    end

```

```

        Y(:,n+1) = ys.old;
    end

    % Transpose the output matrix to put it in the standard form of
    % Matlab's solvers' output.
    710   Y = Y.';

end

715   %%%%%%%%%%%%%%
% INTEGRATE THE ODES %
%%%%%%%%%%%%%

% Build the options set for the integrator
720   options = odeset();
if ( ~isempty(params.num.RelTol) && (params.num.RelTol > 0) )
    options = odeset(options, 'RelTol', params.num.RelTol);
end
if ( ~isempty(params.num.MaxStep) && (params.num.MaxStep > 0) )
    options = odeset(options, 'MaxStep', params.num.MaxStep);
725   end
if ( ~isempty(params.num.AbsTol) && (params.num.AbsTol > 0) )
    options = odeset(options, 'AbsTol', params.num.AbsTol);
end
if ( ~isempty(jacfun) )
    options = odeset(options, 'Jacobian', jacfun);
end

% Integrate
735   if (nargout > 2)
        MU = params.ndg.mu_e + zeros(numel(ts),1);
    end
    tic;
    if (isempty(meta_integrator))
        [T,Y] = integrator(odefun, ts, cbars0, options);
740   else
        [T,Y] = meta_integrator(odefun, integrator, options);
    end
    toc;
745 end

```

THIS PAGE INTENTIONALLY LEFT BLANK

# Bibliography

- [1] Basic research needs for electrical energy storage. Basic Energy Sciences Workshop Reports 1, Department of Energy, 2007.
- [2] Jan L. Allen, T. Richard Jow, and Jeffrey Wolfenstine. Kinetic study of the electrochemical FePO<sub>4</sub> to LiFePO<sub>4</sub> phase transition. *Chemistry of Materials*, 19:2108–2111, 2007.
- [3] Samuel M. Allen and John W. Cahn. A microscopic theory for antiphase boundary motion and its application to antiphase domain coarsening. *Acta Metallurgica*, 27:1085–1095, 1979.
- [4] Anna S. Andersson, Beata Kalska, Lennart Häggström, and John O. Thomas. Lithium extraction/insertion in LiFePO<sub>4</sub>: an X-ray diffraction and Mössbauer spectroscopy study. *Solid State Ionics*, 130:41–52, 2000.
- [5] Luis Arnaut, Sebastiao Formosinho, and Hugh Burrows. *Chemical Kinetics: From Molecular Structure to Chemical Reactivity*. Elsevier, 2007.
- [6] Pankaj Arora, Ralph E. White, and Marc Doyle. Capacity fade mechanisms and side reactions in lithium-ion batteries. *Journal of the Electrochemical Society*, 145(10):3647–3667, 1998.
- [7] Svante Arrhenius. On the reaction velocity of the inversion of cane sugar by acids. *Zeitschrift für physikalische Chemie*, 4:226–232, 1889.
- [8] R.W. Ballufi, S.M. Allen, and W.C. Carter. *Kinetics of Materials*. John Wiley and Sons, 2005.
- [9] Allen J. Bard and Larry R. Faulkner. *Electrochemical Methods: Fundamentals and Applications*. John Wiley & Sons, second edition, 2001.
- [10] M. Z. Bazant, D. Lacoste, and K. Sekimoto. in preparation.
- [11] John O'M. Bockris, Amulya K. N. Reddy, and Maria Gamboa-Aldeco. *Modern Electrochemistry 2A: Fundamentals of Electrodics*. Kluwer Academic, second edition, 2000.

- [12] A.J. Bray. Theory of phase-ordering kinetics. *Advances in Physics*, 43(3):357–459, 1994.
- [13] Damian Burch and Martin Z. Bazant. Size-dependent spinodal and miscibility gaps for intercalation in nano-particles. submitted.
- [14] Damian Burch, Gogi Singh, Gerbrand Ceder, and Martin Z. Bazant. Phase-transformation wave dynamics in LiFePO<sub>4</sub>. *Solid State Phenomena*, 139:95–100, 2008.
- [15] J. W. Cahn and D. W. Hoffman. A vector thermodynamics for anisotropic surfaces–ii. curved and faceted surfaces. *Acta Metallurgica*, 22(10):1205–1214, October 1974.
- [16] John W. Cahn. On spinodal decomposition. *Acta Metallurgica*, 9:795–801, 1961.
- [17] John W. Cahn. Spinodal decomposition. *Transactions of the Metallurgical Society of AIME*, 242:166–180, 1968.
- [18] John W. Cahn and John E. Hilliard. Free energy of a nonuniform system I: Interfacial free energy. *Journal of Chemical Physics*, 28(2):258–267, 1958.
- [19] Gerbrand Ceder. unpublished.
- [20] S. Chandrasekhar. Stochastic problems in physics and astronomy. *Reviews of Modern Physics*, 15(1):1–89, January 1943.
- [21] Guoying Chen, Xiangyun Song, and Thomas J. Richardson. Electron microscopy study of the LiFePO<sub>4</sub> to FePO<sub>4</sub> phase transition. *Electrochemical and Solid-State Letters*, 9(6):A295–A298, 2006.
- [22] Guoying Chen, Xiangyun Song, and Thomas J. Richardson. Metastable solid-solution phases in the LiFePO<sub>4</sub>/FePO<sub>4</sub> system. *Journal of The Electrochemical Society*, 154(7):A627–A632, 2007.
- [23] Long-Qing Chen. Phase-field models for microstructure evolution. *Anual Review of Materials Research*, 32:113–140, 2002.
- [24] W. T. Coffey, Yu. P. Kalmykov, and J. T. Waldron. *The Langevin Equation: With Applications to Stochastic Problems in Physics, Chemistry and Electrical Engineering*. World Scientific, 2004.
- [25] H.E. Cook. Brownian motion in spinodal decomposition. *Acta Metallurgica*, 18:297–306, 1970.
- [26] S.R. de Groot and P. Mazur. *Non-Equilibrium Thermodynamics*. Dover, 1984.
- [27] C. Delacourt, P. Poizot, S. Levasseur, and C. Masquelier. Size effects on carbon-free LiFePO<sub>4</sub> powders: The key to superior energy density. *Electrochemical and Solid-State Letters*, 9(7):A352–A355, 2006.

- [28] Ronald M. Dell and David A.J. Rand. *Understanding Batteries*. Cambridge, 2001.
- [29] C. Delmas, M. Maccario, L. Croguennec, F. Le Cras, and F. Weill. Lithium deintercalation in LiFePO<sub>4</sub> nanoparticles via a domino-cascade model. *Nature Materials*, 7:665–671, August 2008.
- [30] J.L. Dodd, R. Yazami, and B. Fultz. Phase diagram of Li<sub>x</sub>FePO<sub>4</sub>. *Electrochemical and Solid-State Letters*, 9(3):A151–A155, 2006.
- [31] Joanna L. Dodd. *Phase Composition and Dynamical Studies of Lithium Iron Phosphate*. PhD thesis, California Institute of Technology, 2007.
- [32] Robert Dominko, Miran Gaberscek, Jernej Drofenik, Marjan Bele, Stane Pejovnik, and Janko Jamnik. The role of carbon black distribution in cathodes for Li ion batteries. *Journal of Power Sources*, 119–121:770–773, 2003.
- [33] Marc Doyle, Thomas F. Fuller, and John Newman. Modeling of galvanostatic charge and discharge of the lithium-polymer-insertion cell. *The Journal of the Electrochemical Society*, 140(6), June 1993.
- [34] M.S. Dresselhaus and G. Dresselhaus. Intercalation compounds of graphite. *Advances in Physics*, 30:139–325, 1981. also reprinted as Advances in Physics 51 (2002) 1.
- [35] Heike Emmerich. *The Diffuse Interface Approach in Materials Science: Thermodynamic Concepts and Applications of Phase-Field Models*. Springer-Verlag, 2003.
- [36] Lawrence C. Evans. *Partial Differential Equations*. American Mathematical Society, 1998.
- [37] M. G. Evans and M. Polanyi. Some applications of the transition state method to the calculation of reaction velocities, especially in solution. *Transactions of the Faraday Society*, 31:875–894, 1935.
- [38] George M. Ewing. *Calculus of Variations with Applications*. Dover, 1985.
- [39] Henry Eyring. The activated complex in chemical reactions. *Journal of Chemical Physics*, 3:107–115, 1935.
- [40] William Feller. *An Introduction to Probability Theory and Applications Volume I*. John Wiley and Sons, third edition, 1970.
- [41] Enrico Fermi. *Thermodynamics*. Dover, 1956.
- [42] Hans Peter Fischer, Philipp Maass, and Wolfgang Dieterich. Novel surface modes in spinodal decomposition. *Physical Review Letters*, 79(5):893–896, 1997.

- [43] Miran Gaberscek, Robert Dominko, and Janez Jamnik. Is small particle size more important than carbon coating? an example study on LiFePO<sub>4</sub> cathodes. *Electrochemistry Communications*, 9(12):2778–2783, 2007.
- [44] Mariano Giaquinta and Stefan Hildebrandt. *Calculus of Variations I*. Springer, 2004.
- [45] V.L. Ginzburg and L.D. Landau. On the theory of superconductivity. *Zh. Eksp. Teor. Fiz.*, 20:1064–1082, 1950.
- [46] Istvan Gyarmati. *Non-Equilibrium Thermodynamics: Field Theory and Variational Principles*. Springer-Verlag, 1970.
- [47] B.C. Han, A. Van der Ven, D. Morgan, and G. Ceder. Electrochemical modeling of intercalation processes with phase field models. *Electrochimica Acta*, 49:4691–4699, 2004.
- [48] P. Hawrylak and K. R. Subbaswamy. Kinetic model of state transformation and intercalation in graphite. *Physical Review Letters*, 53(22):2098–2101, 1984.
- [49] J. E. Hilliard. Spinodal decomposition. In H. I. Aaronson, editor, *Phase Transformations: Papers presented at a Seminar of the American Society for Metals, October 12 and 13, 1968*, pages 497–560. American Society for Metals, 1970.
- [50] P.C. Hohenberg and B.I. Halperin. Theory of dynamic critical phenomena. *Reviews of Modern Physics*, 49(3):435–479, July 1977.
- [51] H. Huang, S.-C. Yin, and L.F. Nazar. Approaching theoretical capacity of LiFePO<sub>4</sub> at room temperature at high rates. *Electrochemical and Solid-State Letters*, 4(10):A170–A172, 2001.
- [52] R. Huggins. *Advanced Batteries: Materials Science Aspects*. Springer, 2008.
- [53] Barry D. Hughes. *Random Walks and Random Environments Volume 1: Random Walks*. Clarendon Press, 1995.
- [54] James M. Hyman, Robert J. Knapp, and James C. Scovel. High order finite volume approximations of differential operators on nonuniform grids. *Physica D*, 60:112–138, 1992.
- [55] M. Saiful Islam, Daniel J. Driscoll, Craig A. J. Fisher, and Peter R. Slater. Atomic-scale investigation of defects, dopants, and lithium transport in the LiFePO<sub>4</sub> olivine-type battery material. *Chemistry of Materials*, 17(20):5085–5092, 2005.
- [56] C. R. Johnson. Positive definite matrices. *American Mathematical Monthly*, 77(3):259–264, March 1970.
- [57] Byoungwoo Kang and Gerbrand Ceder. Battery materials for ultrafast charging and discharging. *Nature*, 458:190–193, March 2009.

- [58] Ioannis Karatzas and Steven E. Shreve. *Brownian Motion and Stochastic Calculus*. Springer-Verlag, second edition, 2004.
- [59] A. Karma. Phase field methods. In K.H.J. Buschow, R.W. Cahn, M.C. Flemings, B. Ilschner, E.J. Kramer, and S. Mahajan, editors, *Encyclopedia of Materials: Science and Technology Vol. 7*, pages 6873–6886. Elsevier, 2001.
- [60] Dong-Han Kim and Jaekook Kim. Synthesis of LiFePO<sub>4</sub> nanoparticles in polyol medium and their electrochemical properties. *Electrochemical and Solid-State Letters*, 9(9):A439–A442, 2006.
- [61] Jae-Kwang Kim, Gouri Cheruvally, Jae-Won Choi, Jong-Uk Kim, Jou-Hyeon Ahn, Gyu-Bong Cho, Ki-Won Kim, and Hyo-Jun Ahn. Effect of mechanical activation process parameters on the properties of LiFePO<sub>4</sub> cathode material. *Journal of Power Sources*, 166(1):211–218, 2007.
- [62] H. A. Kramers. Brownian motion in a field of force and the diffusion model of chemical reactions. *Physica*, 7:284–304, 1940.
- [63] L. Laffont, C. Delacourt, P. Gibot, M. Yue Wu, P. Kooyman, C. Masquelier, and J. Marie Tarascon. Study of the LiFePO<sub>4</sub>/FePO<sub>4</sub> two-phase system by high-resolution electron energy loss spectroscopy. *Chemistry of Materials*, 18:5520–5529, 2006.
- [64] J.S. Langer. Theory of spinodal decomposition in alloys. *Annals of Physics*, 65:53–86, 1971.
- [65] F.C. Larché and J.W. Cahn. A linear theory of thermochemical equilibrium of solids under stress. *Acta Metallurgica*, 21(8):1051–1063, 1973.
- [66] Randall J. Leveque. *Finite Volume Methods for Hyperbolic Problems*. Cambridge University Press, 2002.
- [67] Gilbert Newton Lewis and Merle Randall. *Thermodynamics*. McGraw-Hill, 1961.
- [68] David Linden and Thomas B. Reddy, editors. *Handbook of Batteries*. McGraw-Hill, third edition, 2002.
- [69] H. Liu, Q. Cao, L.J. Fu, C. Li, Y.P. Wu, and H.Q. Wu. Doping effects of zinc on LiFePO<sub>4</sub> cathode material for lithium ion batteries. *Electrochemistry Communications*, 8(10):1553–1557, 2006.
- [70] C.H.P. Lupis. *Chemical Thermodynamics of Materials*. Prentice-Hall, 1983.
- [71] Richard I. Masel. *Chemical Kinetics and Catalysis*. John Wiley & Sons, 2001.
- [72] Thomas Maxisch and Gerbrand Ceder. Elastic properties of olivine Li<sub>x</sub>FePO<sub>4</sub> from first principles. *Physical Review B*, 73(17), 2006.

- [73] Nonglak Meethong, Hsiao-Ying Shadow Huang, W. Craig Carter, and Yet-Ming Chiang. Size-dependent lithium miscibility gap in nanoscale  $\text{Li}_{1-x}\text{FePO}_4$ . *Electrochemical and Solid-State Letters*, 10(5):A134–A138, 2007.
- [74] D. Morgan, A. Van der Ven, and G. Ceder. Li conductivity in  $\text{Li}_x\text{MPO}_4$  ( $\text{M}=\text{Mn,Fe,Co,Ni}$ ) olivine materials. *Electrochemical and Solid-State Letters*, 7(2):A30–A32, 2004.
- [75] John Newman. Fortran programs for the simulation of electrochemical systems.
- [76] John Newman and William Tiedemann. Porous-electrode theory with battery applications. *AIChE Journal*, 21(1):25–41, January 1975.
- [77] John S. Newman. *Electrochemical Systems*. Prentice Hall, second edition, 1991.
- [78] Shin-Ichi Nishimura, Genki Kobayashi, Kenji Ohoyama, Ryoji Kanno, Masatomo Yashima, and Atsuo Yamada. Experimental visualization of lithium diffusion in  $\text{Li}_x\text{FePO}_4$ . *Nature Materials*, 7:707–711, September 2008.
- [79] R. O’Hayre, S. Cha, W. Colella, and F. B. Prinz. *Fuel Cell Fundamentals*. Wiley, 2nd edition edition, 2009.
- [80] Tsutomu Ohzuku, Masaki Kitagawa, and Taketsugu Hirai. Electrochemistry of manganese dioxide in lithium nonaqueous cell. *Journal of the Electrochemical Society*, 137(3):769–775, 1990.
- [81] Lars Onsager. Reciprocal relations in irreversible processes I. *Physical Review*, 37:405–426, February 1931.
- [82] Ole Østerby. Five ways of reducing the Crank-Nicolson oscillations. unpublished.
- [83] A.K. Padhi, K.S. Nanjundaswamy, and J.B. Goodenough. Phospho-olivines as positive-electrode materials for rechargeable lithium batteries. *The Journal of the Electrochemical Society*, 144(4):1188–1194, April 1997.
- [84] I. Prigogine and R. Defay. *Chemical Thermodynamics*. John Wiley & Sons, 1954.
- [85] C.V. Ramana, A. Mauger, F. Gendron, C.M. Julien, and K. Zaghib. Study of the Li-insertion/extraction process in  $\text{LiFePO}_4/\text{FePO}_4$ . *Journal of Power Sources*, 187(2):555–564, 2009.
- [86] A. N. Richards and A. Rodgers. Synthetic metallomolecules as agents for the control of dna structure. *Chem. Soc. Rev.*, 36:471–483, 2007.
- [87] H. Risken. *The Fokker-Planck Equation: Methods of Solution and Applications*. Springer-Verlag, 1984.

- [88] Ho Chul Shin, Won Il Cho, and Ho Jang. Electrochemical properties of carbon-coated LiFePO<sub>4</sub> cathode using graphite, carbon black, and acetylene black. *Electrochimica Acta*, 52(4):1472–1476, 2006.
- [89] Charles R. Sides, Fausto Croce, Vaneica Y. Young, Charles R. Martin, and Bruno Scrosatic. A high-rate, nanocomposite LiFePO<sub>4</sub>/carbon cathode. *Electrochemical and Solid-State Letters*, 8(9):A484–A487, 2005.
- [90] Gogi K. Singh, Gerbrand Ceder, and Martin Z. Bazant. Intercalation dynamics in rechargeable battery materials: General theory and phase-transformation waves in LiFePO<sub>4</sub>. *Electrochimica Acta*, 53:7599–7613, 2008.
- [91] R. Spotnitz. Simulation of capacity fade in lithium-ion batteries. *Journal of Power Sources*, 113(1):72–80, 2003.
- [92] Venket Srinivasan and John Newman. Discharge model for the lithium iron-phosphate electrode. *Journal of the Electrochemical Society*, 151(10):A1517–A1529, 2004.
- [93] Liam Stanton and Martin Z. Bazant. Anisotropic lattice mismatch strain in phase-separating systems. in preparation.
- [94] Ming Tang, Hsiao-Ying Huang, Nonglak Meethong, Yu-Hua Kao, W. Craig Carter, and Yet-Ming Chiang. Modeling particle size effects on phase stability and transition pathways in nanosized olivine cathode particles. In *Materials Research Society Symposium Proceedings Volume 1100*, 2008.
- [95] Lloyd N. Trefethen. *Spectral Methods in Matlab*. Society for Industrial and Applied Mathematics, 2000.
- [96] J. D. van der Waals. The thermodynamic theory of capillarity under the hypothesis of a continuous variation of density. *Verhandel. Konink. Akad. Weten. Amsterdam*, 1(8), 1893. translated by J. S. Rowlinson in *Journal of Statistical Physics* 20(2):200–244, 1979.
- [97] N. G. van Kampen. *Stochastic Processes in Physics and Chemistry*. Elsevier, third edition, 2007.
- [98] Jacobus Henricus van't Hoff. *Studies in Chemical Dynamics*. Williams And Norgate, 1884.
- [99] J. Vetter, P. Novák, M.R. Wagner, C. Veit, K.C. Möller, J.O. Besenhard, M. Winter, M. Wohlfahrt-Mehrens, C. Vogler, and A. Hammouche. Ageing mechanisms in lithium-ion batteries. *Journal of Power Sources*, 147:269–281, 2005.
- [100] Colin A. Vincent and Bruno Scrosati. *Modern Batteries: An Introduction to Electrochemical Power Sources*. John Wiley and Sons, second edition, 1997.

- [101] Deyu Wang, Hong Li, Zhaoxiang Wang, Xiaodong Wu, Yucheng Sun, Xuejie Huang, and Liquan Chen. New solid-state synthesis routine and mechanism for LiFePO<sub>4</sub> using LiF as lithium precursor. *Journal of Solid State Chemistry*, 177(12):4582–4587, 2004.
- [102] Deyu Wang, Xiaodong Wu, Zhaoxiang Wang, and Liquan Chen. Cracking causing cyclic instability of LiFePO<sub>4</sub> cathode material. *Journal of Power Sources*, 140:125–128, 2005.
- [103] Robert Weinstock. *Calculus of Variations with Applications to Physics and Engineering*. Dover, 1974.
- [104] C. John Wen, B. A. Boukamp, R. A. Huggins, and W. Weppner. Thermodynamic and mass transport properties of “LiAl”. *Journal of the Electrochemical Society*, 126(12):2258–2266, 1979.
- [105] A. Yamada, S. C. Chung, and K. Hinokuma. Optimized LiFePO<sub>4</sub> for lithium battery cathodes. *Journal of the Electrochemical Society*, 148(3):A224–A229, 2001.
- [106] Shoufeng Yang, Yanning Song, Peter Y. Zavalij, and Stanley Whittingham. Reactivity, stability and electrochemical behavior of lithium iron phosphates. *Electrochemistry Communications*, 4:239–244, 2002.
- [107] Denis Y. W. Yu, Christopher Fietze, Wolfgang Weydanz, Kazunori Donoue, Takao Inoue, Hiroshi Kurokawa, and Shin Fujitani. Study of LiFePO<sub>4</sub> by cyclic voltammetry. *Journal of The Electrochemical Society*, 154(4):A253–A257, 2007.
- [108] K. Zaghib, A. Mauger, F. Gendron, and C. M. Julien. Surface effects on the physical and electrochemical properties of thin LiFePO<sub>4</sub> particles. *Chemistry of Materials*, 20(2):462–469, 2008.